STRUCTURAL DAMAGE DIAGNOSIS AND REMAINING USEFUL LIFE ASSESSMENT MODEL FOR ADHESIVELY BONDED COMPOSITE MATERIALS

Yang Zhang, M.Sc. Eng

A dissertation submitted to the Scientific Board of the Szewalski Institute of Fluid-Flow Machinery, Polish Academy of Sciences in partial fulfillment of the requirements for the

Doctor of Philosophy

Supervisor
Wiesław Ostachowicz, Prof., D.Sc., Ph.D. Eng
Maciej Radzieński, D.Sc., Ph.D. Eng

April 2025

Truth and failure are the twin guides on the path of enlightenment

Veritas numquam perit

Declaration

I hereby declare that except where specific reference is made to the work of others, the contents of this dissertation are original and have not been submitted in whole or in part for consideration for any other degree or qualification in IMP PAN, or any other unit. This dissertation is my own work and contains nothing which is the outcome of work done in collaboration with others, except as specified in the text and Acknowledgements.

Certain figures and tables used in this dissertation are sourced from the published journals that has been listed in Publication. The research presented herein has been conducted entirely independently by me, and I hereby declare this assertion.

Yang Zhang, M.Sc. Eng

Gdańsk, Poland
April 2025

Acknowledgements

The completion of this dissertation marks the culmination of years of dedication, perseverance, and unwavering support from those dearest to me. As I reflect on this journey, I am filled with immense gratitude for the people who have stood by my side, offering their love, encouragement, and belief in me.

First and foremost, I would like to express my deepest gratitude to my supervisor, Prof. Wiesław Ostachowicz, for his invaluable support in both my academic and personal life. He was the first professor I met in Poland, and beyond his profound knowledge and expertise, he has imparted to me something even more precious—wisdom, humility, and composure. These qualities will guide me far beyond my academic journey, shaping the way I approach life itself. I am also deeply grateful to my co-supervisor, Dr. Maciej Radzieński—a mentor and a friend. He embodies the perfect balance between a passion for life and a deep dedication to work. Over the past four years, he has patiently guided me through every experiment and has carefully revised each paper with unwavering attention to detail.

Beyond academia, my deepest appreciation goes to my parents, whose love and sacrifices have been my greatest source of strength. To my parents, whose unwavering support has carried me through life's many challenges. And my grandparents who always care about and support me whatever I want to try.

To my beloved wife, Ms. Chen Xiu, my pillar of strength and my source of boundless inspiration—thank you for walking this journey with me, for your patience, understanding, and the countless ways in which you have supported me. Your belief in me, even during the most challenging moments, has been my greatest motivation. This dissertation is as much yours as it is mine.

Finally, to my newborn son, sweet Xiuheng Zhang, whose born has given my life newfound meaning. Your presence fills my heart with joy, and I hope that one day, when you see this dissertation, you will be able to feel your father's infinite love for you.

This dissertation is dedicated to all those who have supported me throughout this journey. I am sincerely grateful for their encouragement and guidance.

Acknowledgements

This doctoral research was made possible through the generous support of the following foundations and organizations, to whom we extend our deepest gratitude.

国家留学基金管理委员会
CHINA SCHOLARSHIP COUNCIL

NATIONAL SCIENCE CENTRE
POLAND
Grant no. 2023/49/N/ST8/00473

FNP
START 99/2024

cost
EUROPEAN COOPERATION
IN SCIENCE & TECHNOLOGY

Funded by
the European Union

Abstract

Composite materials are widely adopted in aerospace and other high-performance applications due to their lightweight characteristics and excellent mechanical properties. Currently, adhesive bonding has become the preferred alternative to traditional riveted joints for assembling composite structures. However, the complexity of manufacturing processes, combined with varying operational conditions, often leads to internal defects such as disbonds and voids, which significantly increase the risk of structural failure. As a result, despite its advantages in maintaining load transfer continuity and preserving fibre integrity, adhesive bonding still faces acceptance challenges compared to conventional mechanical fastening methods.

Currently, various non-destructive testing and structural health monitoring-based techniques are employed to inspect composite structures and assess their remaining service life, with the aim of enhancing detection accuracy and extending operational longevity. However, due to the extreme sensitivity of traditional elastic wave methods to the microstructure of the actually bonded region and noise interference, achieving effective detection remains a significant challenge. In recent years, the emergence of multi-model ensemble techniques has helped overcome these issues. Hybrid models based on digital twins integrate signal processing techniques with deep learning, addressing the challenges associated with fault feature extraction in traditional methods while providing a neural network-based approach for predicting remaining useful life.

The primary objective of this dissertation is to develop a model for damage diagnosis and remaining useful life prediction of bonded composite materials. It also highlights the feasibility of using guided waves for experimental measurements and assessing the crack length within adhesion. Compared to single neural network structures, this study adopts a multi-model collaborative approach to address the issues associated with classic neural network-based remaining useful life prediction, such as single-value outputs and the reliance on Bayesian networks for uncertainty quantification. Adopting the ensemble fracture mechanics model effectively simulates the nonlinear characteristics of crack propagation, which is not constrained by limitations related to the insufficient initial sample size or a short prediction horizon. Furthermore, a dropout-based approximation of the Bayesian approach is used, eliminating the need to assign probability distributions to hidden layer nodes within the neural network, thereby reducing model complexity. The prediction output consists of confidence intervals, improving the reliability of the results. Compared with traditional Bayesian networks, repeated experimental trials demonstrate an accuracy improvement of 16.43%. Additionally, a data augmentation and segmentation method is proposed to address the initial-stage deviation problem in remaining useful life prediction. Experimental results show that initial-stage prediction errors can be effectively reduced after data adjustments. Chapter 5 presents the results of all models developed in this dissertation, alongside a comparative analysis with currently established mainstream approaches.

The integration of multi-model digital twin technology aims to resolve the issues of Bayesian dependence in prediction processes and the single-value nature of remaining useful life predictions. This research further provides technical support for the broader application of adhesively bonded composite materials across different fields.

Publications

Journal papers

- **Y. Zhang**, M. Radzieński, R. Soman, W. Ostachowicz. "Spatial domain localization method for multi-damage in plate-like structure based on coefficient matrix of reflected guided waves." ***Journal of Sound and Vibration***, vol. 552, 2023, p. 117636.
- **Y. Zhang**, M. Radzieński, W. Ostachowicz. "Diagnostic-prognostic framework for assessing the health status of composite structures." ***International Journal of Mechanical Sciences***, vol. 278, 2024, p. 109461.
- **Y. Zhang**, M. Radzieński, S. Xue, Z. Wang, W. Ostachowicz. "A method for detecting cracks on the trailing edge of wind turbine blades based on aeroacoustic noise analysis." ***Structural Health Monitoring***, 2024.
- **Y. Zhang**, M. Radzieński, J. Chen, Z. Wang, W. Ostachowicz. "Predicting the remaining useful life of adhesively bonded composites using guided waves and a multi-connected approximate Bayesian model." ***NDT & E International Journal***, Under review.
- **Y. Zhang**, R. Wang, S. Li, S. Qi. "Temperature sensor denoising algorithm based on curve fitting and compound Kalman filtering." ***Sensors***, 20 (2020) 1959.

Conference papers

- **Y. Zhang**, R. Soman, M. Radzieński, W. Ostachowicz. "Damage Simulation Method for Adhesively Bonded Composite Structures Based on XFEM and Cohesive Hybrid Model." In: *50th Annual Review of Progress in Quantitative Nondestructive Evaluation*, American Society of Mechanical Engineers, USA, 2023, p. V001T09A003.
- **Y. Zhang**, M. Radzieński, W. Ostachowicz. "Effect of bending modes on failure analysis of adhesively bonded composite structures." In: *Health Monitoring of Structural and Biological Systems XVIII*, SPIE, USA, 2024, p. 1295104.

- **Y. Zhang**, M. Radzieński, W. Ostachowicz. "Methods for Remaining Useful Life Prognosis of Adhesively Bonded Composite Structures."In: *51st Annual Review of Progress in Quantitative Nondestructive Evaluation*, American Society of Mechanical Engineers, USA, 2024.

Project

- **Damage Diagnosis and Remaining Useful Life Prognosis of Adhesively Bonded Composite Structures Based on Digital Twin and Deep Learning Hybrid Model**
  National Science Centre, Preludium 22, 139,400 PLN
  Principal investigator: Yang Zhang

Scholarship and Stipend

- START, Foundation for Polish Science, 2024.
- PhD Scholarship, China Scholarship Council, 2021.

Table of contents

List of figures

List of tables

Nomenclature

Roman Symbols

A	amplitude of guided waves
C_L	longitudinal wave velocity of guided waves
C_p	phase velocity of guided waves
C_S	shear wave velocity of guided waves
$F(\omega)$	Fourier transform of an input signal (excitation signal at any location) $f(t)$
h	thickness of homogeneous media
$k(\omega,x)$	wavenumber of guided waves
$Y(t,x)$	time-space wave-field when guided waves reach the position x
$Y(\omega)$	frequency spectrum signal of $Y(t,x)$

Acronyms / Abbreviations

BNN	Bayesian Neural Network
CFRP	Carbon-Fiber Reinforced Polymer
CNN	Convolutional Neural Network
CRA	Cumulative Relative Accuracy
DL	Deep Learning
DT	Digital Twin
DTHM	Digital Twin Hybrid Model

ELBO	Evidence Lower Bound
EoL	End-of-Life
FEA	Finite Element Analysis
FEM	Finite Element Method
FM	Fracture Mechanics
GW	Guided Waves
LSTM	Long Short-Term Memory
MAE	Mean Absolute Error
MAPE	Mean Absolute Percentage Error
MC	Monte Carlo
ML	Machine Learning
MSE	Mean Squared Error
NDT	Non-Destructive Testing
NN	Neural Network
PA	Phased Array
PZT	Piezoelectric Transducer
ReLu	Rectified Linear Unit
RMSE	Root Mean Squared Error
RNN	Recurrent Neural Network
RUL	Remaining Useful Life
S-S	Strain-Stress
SERR	Strain Energy Release Rate
SHM	Structure Health Monitoring
SH	Shear Horizontal

SLJ	Single Lap Joint
T-S	Traction-Separation
XFEM	eXtended Finite Element Methods

Chapter 1

Introduction

1.1 Introduction

In recent years, driven by the growing imperative to achieve unprecedented levels of eco-efficiency, the aircraft industry has been striving for ultra-lightweight structures. To this goal, composites are increasingly replacing conventional metal due to their high tensile stiffness and low weight. This trend is mirrored across the aerospace, automotive, wind energy, and marine sectors, where combining different composite materials enhances the strength-to-weight ratio.

However, joint design practices have not kept pace with this transition. At present, composite structures are still commonly assembled using mechanical fasteners. This approach not only introduces a considerable weight penalty but also compromises structural integrity by cutting through load-bearing fibres and disrupting the load path. The limited adoption of adhesive joints can be attributed to several factors: insufficient understanding of critical manufacturing parameters, difficulties in non-destructive testing (NDT), gaps in structural health monitoring (SHM) methodologies, and the absence of a robust framework for diagnosis-prognosis [1, 2]. Compared to conventional rivet fastening methods, adhesive bonding offers advantages including the reduced weight and the preservation of the inherent mechanical properties of the materials, making it particularly well-suited to composites [3–5].

Moreover, the integrity of the bonded interface is an essential factor that must be considered when employing such structures. Challenges such as surface preparation, fatigue life prediction, material durability, and the demand for reliable SHM and remaining useful life (RUL) assessment systems continue to hinder the widespread application of bonded joints. Failures in bonded structures may occur in various forms, with common types including adhesive failure and adherend damage. Numerous studies have demonstrated that early-stage damage in these systems is often repairable. This has prompted extensive experimental and analytical efforts to ensure that early damage can be detected and repaired before progressing to an irreparable state.

Consequently, this doctoral dissertation aims to develop an integrated diagnostic–prognostic framework capable of accurately identifying damage in the adhesive zone and predicting the RUL of the structure following damage initiation.

1.2 Research question and objectives

Current research on SHM and RUL prediction of adhesively bonded composite structures primarily relies on conventional fracture mechanics (FM) and data-driven techniques. Both approaches face notable limitations. The FM models often struggle to predict RUL accurately due to insufficient experimental data for calibration and their inability to quantify uncertainty. Data-driven models often overlook the fatigue crack growth mechanisms. Sole reliance on input training data fails to represent the nonlinear nature of crack propagation, which restricts the capacity of data-driven models to capture and predict complex fracture behaviours effectively.

Although the hybrid model techniques of neural networks (NN) with Bayesian statistical methods have improved the feasibility of RUL prediction, they still lack the incorporation of FM required to model the nonlinear progression of crack growth. This shortcoming ultimately leads to reduced accuracy, particularly in the high-cycle fatigue failure.

To address these limitations, this dissertation proposes a digital twin hybrid model (DTHM) with three key features:

- a deep learning (DL) hybrid model integrating FM theories;
- using guided waves (GW) to quantify the damage extent;
- utilising hybrid model with dropout to approximately replace Bayesian neural network (BNN) to predict RUL and quantify uncertainty.

1.3 Thesis of the work

Combining FM with machine learning (ML) methods via digital twin (DT) technology enables damage diagnosis and RUL prognosis with uncertainty quantification for the bonding zones of adhesively bonded composite structures.

1.4 Methodology

The research methodology of this dissertation is centred on multidisciplinary model fusion. The hierarchical framework, referred to in this dissertation as a diagnostic–prognostic model, comprises three core components: damage extent quantification model, fatigue crack growth calculation, and an RUL prognosis model. The detailed methodologies are introduced as follows:

- The crack growth calculation module combines FM with the extended finite element method (XFEM). Simulation data generated from Abaqus, COMSOL, and FE-life are incorporated into a DT database to support the training of ML model;
- The experimental module constitutes the physical system and consists of two components: damage quantification experiments based on the GW and fatigue life characterisation. The purpose of this module is to quantify damage extent, and obtain experimental damage data and corresponding end-of-life (EoL) values;
- The RUL prognosis model, built on the DT concept, processes and integrates data from both simulated and physical models. It predicts RUL using DL frameworks and platforms, developed by TensorFlow and implemented via the Anaconda environment.

This methodology integrates experimental procedures, numerical simulations, and advanced computing techniques in a coordinated manner, thereby enabling comprehensive health assessment of adhesively bonded composite structures.

1.5 Dissertation contributions

This dissertation builds upon the current state-of-the-art and has the potential to significantly improve the RUL prediction results of adhesive bonding composites, aiming to bring them as close as possible to actual life. In the process of damage detection and quantification, the hybrid model includes an innovative damage extent quantification method by using GW. In the simulation process, this dissertation presents a DTHM that integrates the XFEM and FM, which enables the calculation of nonlinear fatigue crack growth. Additionally, this research introduces an approximate approach to replace BNN by employing dropout and Monte Carlo (MC) sampling in ML to quantify uncertainty in the RUL prognosis process.

First, the study introduces a convolutional neural network (CNN)-long short-term memory (LSTM) hybrid networks with dropout and MC sampling to predict RUL and quantify uncertainty. This method does not require frequent modifications to hyperparameters and quantifies uncertainty in the network, as dropout is capable of producing probabilistic outcomes. This approach simplifies the process instead of using BNN to quantify uncertainty and avoid increased running time and complex node hyperparameters.

Subsequently, in order to accurately simulate the nonlinear process of crack propagation, this dissertation collects simulation data from the crack growth solver. The solver combined with the RUL prediction model forms a DTHM, which effectively solves the problem of difficulty in predicting nonlinear crack propagation using NN. Compared to existing RUL prediction methods, this approach offers significant advantages in both efficiency and accuracy.

In summary, this dissertation sheds light on the modelling that combines FM with intelligent algorithms to advance the application of SHM and RUL prognosis in bonded composite structures, thereby encouraging wider acceptance of such structures.

1.6 Dissertation organization

The first Chapter discusses the methodology and key contributions of the research field. This is to help readers better understand the structure of this dissertation. The rest of the dissertation is organized as follows:

Chapter 2 presents a literature review relevant to this research, with a primary focus on the technologies and models used in SHM for damage diagnosis and RUL prognosis of the adhesively bonded composite materials.

Chapter 3 introduces the data-driven RUL prediction method, providing a detailed description of the NN commonly employed in the RUL prediction process.

Chapter 4 builds upon Chapter 3 by presenting the methodology of this study, specifically a diagnosis-prognosis framework based on DT technology.

Chapter 5 demonstrates the RUL prediction results using a single lap joint (SLJ) as a specimen. Meanwhile, the proposed approach is compared with published methods, including BNN and CNN, to highlight the advantages of the proposed DTHM methods.

Chapter 6 presents the conclusions of this dissertation and discusses potential future research directions that build upon the current work.

Chapter 2

Literature review

2.1 Introduction

This chapter reviews the major studies and methodologies developed for predicting damage and RUL in the adhesive zone of bonded composite structures. The existing literature primarily focuses on three research directions: SHM technologies based on GW, RUL prediction models for bonded structures, and the application of DT technology in this context. The structure of this chapter is outlined in Fig. 2.1.

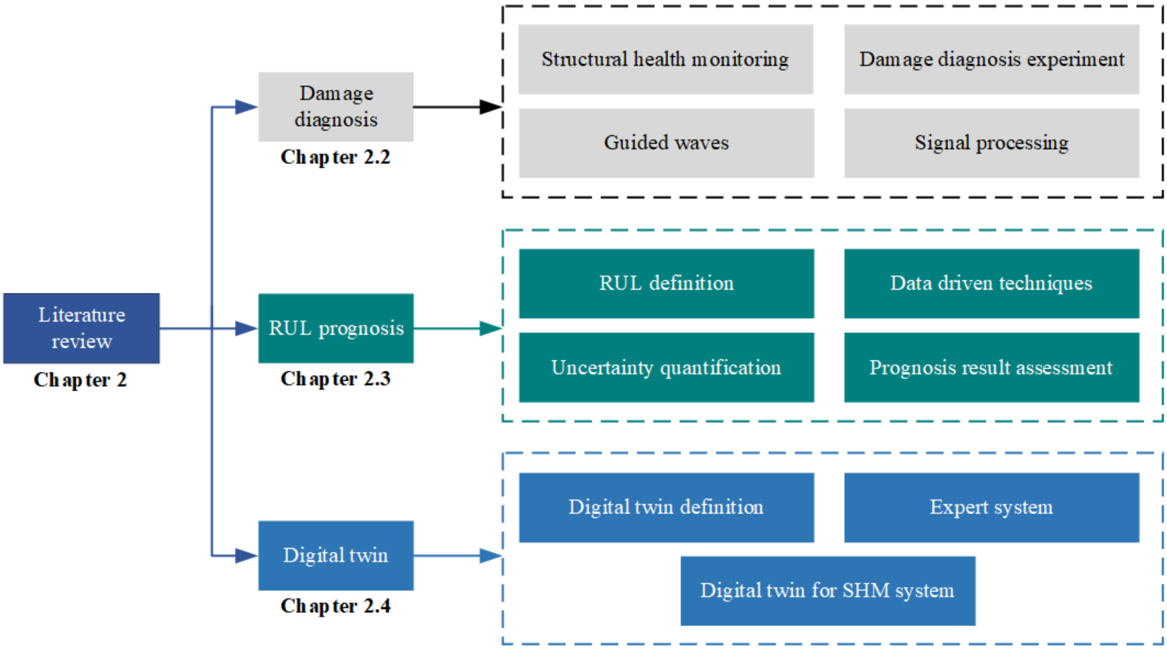

Figure 2.1 The content structure of the literature review.

Additionally, this chapter not only reviews the state-of-the-art but also critically examines the limitations and research gaps within existing studies. The objective is to provide a comprehensive overview of both experimental and numerical investigations related to damage detection and RUL prognosis in adhesively bonded composite structures.

2.2 Damage diagnosis by using guided waves

Compared to conventional riveted connections, adhesive bonding of composite materials offers a practical solution for broadening their applications [6], while mitigating structural damage and reducing stress concentrations. However, damage detection and structural health evaluation in bonded composite assemblies remain key challenges that limit progress in the field. This section outlines experimental and numerical approaches for structural damage diagnosis using GW, with a focus on damage quantification. The discussion is organised into three sub-sections: GW-based detection principles, experimental procedures, and signal processing techniques.

2.2.1 Structural health monitoring

SHM refers to technologies used to detect, locate, and quantify changes in material structures resulting from damage or degradation. As a multidisciplinary field, SHM integrates concepts from automation, mechanics, mechanical, and civil engineering. It is generally classified into contact and non-contact methods [7–9]. Common contact methods include GW, acoustic emission (AE), and vibration-based approaches. Non-contact techniques are typically based on acoustics, laser technologies, and visual inspection [10, 11]. Regardless of classification, the primary aim of SHM methods is to detect damage and ensure long-term structural performance. Current research is particularly focused on applications in wind turbines, aircraft, and bridges [3, 6, 12–14].

The majority of SHM techniques rely on the excitation and measurement of signals using specially designed actuators and sensors, with structural health status assessed through the analysis of damage-related features. Although specific requirements may vary across application domains, the objective remains consistent: to obtain comprehensive structural health information. In certain practical scenarios, damage detection must operate continuously and under all conditions, referred to as active SHM technology [15]. Additionally, employing embedded sensors such as optical fiber systems integrated into composite materials is also a popular SHM technology [16]. These diverse scenarios underscore the adaptability of SHM in enabling full-field and large-scale damage detection [17]. As a result, SHM technologies have been progressively adopted across various disciplines. A summary of representative damage detection methods and SHM techniques is presented in Tab. 2.1 [17].

Table 2.1 Commonly used NDT and SHM techniques.

Technique	Application	Advantages	Limitations
GW	Cracks; Impact; Delamination; Hole; Broken fibre; Debonding; Adhesive failures; Fatigue damage.	GW enable long-distance, cost-effective monitoring of large areas, and are useful for detecting internal damage in thin materials.	Dispersive nature and multiple modes in single frequency; lower capacity to detect small size damage.
AE	Cracks; Delamination; Debonding; Fibre breakage; Impact; Matrix micro damage; Corrosion; Fatigue damage.	AE offers real-time monitoring, enabling the detection of damage within structures with high sensitivity.	AE technology is sensitive to noise, which can interfere with the characteristic signal. Need a precision signal processing method to analyse the signal.
Vibration	Cracks; Delamination; Corrosion; Stiffness changes; Debonding; Buckling; Loose connection.	Vibration monitoring can identify changes in vibration patterns, indicating early-stage damage. This method allows for real-time, continuous monitoring, effectively detecting issues like rotating machinery.	It is sensitive to environmental noise, and it requires complex data analysis with specific signal processing algorithms. It is difficult to precisely locate damage and often necessitates baseline data.

Table 2.1 (continued)

Technique	Application	Advantages	Limitations
Thermography	Translaminar cracks; Inclusions; Laminated failures; Delamination; Debonding; Impact; Fatigue damage; Corrosion.	Thermal imaging is a non-contact method that can be used to quickly detect damage on large surfaces and to accurately locate damage.	It is limited to detecting surface or near-surface damage, and its accuracy may be affected by ambient temperature and lighting. And the detection instrument is expensive.
Electrical Resistance	Cracks; Delamination; Debonding; Corrosion; Fatigue damage.	Resistive technology is effective at detecting changes in conductivity due to damage and is sensitive to small damage.	Requires direct contact with the structure and is limited to conductive materials. Its sensitivity depends on factors such as fiber volume and electrode location, as well as ambient temperature.
Electromechanical Impedance	Cracks; Delamination; Debonding; Corrosion; Fatigue damage.	Utilizes high-frequency structural vibrations to detect local stiffness changes, offering high sensitivity to incipient damage.	Requires direct contact with the structure and is influenced by environmental conditions such as temperature and humidity.

Table 2.1 (continued)

Technique	Application	Advantages	Limitations
Laser scanning	Surface damage; Cracks; Corrosion; Impact.	Laser scanning is a non-contact and highly accurate technique that enables remote sensing, making it suitable for delicate or hard-to-reach structures.	Sensitive to environmental conditions. Equipment is expensive and requires careful calibration.
Visual inspection	Surface damage.	Optical inspection using cameras is non-contact, provides visual documentation, and is easy to implement for surface damage detection and monitoring.	Limited to detecting surface damage, and its effectiveness can be compromised by poor lighting conditions, obstructions, or the size of the damage.

SHM techniques can generally be categorised into five levels based on the research objectives [18]. Typically, SHM involves using a network of advanced sensing and actuation elements integrated within the structure to obtain information related to the structural health status (first level). Advanced signal processing methods are then employed to extract characteristic parameters and locate the damage (second level). Using information from the detection samples, the extent of the damage is determined (third level). This process ultimately leads to an assessment of the structure performance (fourth level) and RUL prognosis of the damaged structure (fifth level). The specific SHM development roadmap is illustrated in Fig. 2.2.

This dissertation adopts GW-based SHM techniques to quantify the damage extent. In view of its integration with a subsequent framework for RUL prediction, the research aligns with the fifth level of SHM, as illustrated in Fig. 2.2. The proposed framework is designed not only to assess structural integrity but also to predict the RUL, thereby contributing to the broader goal of ensuring long-term structural safety and durability.

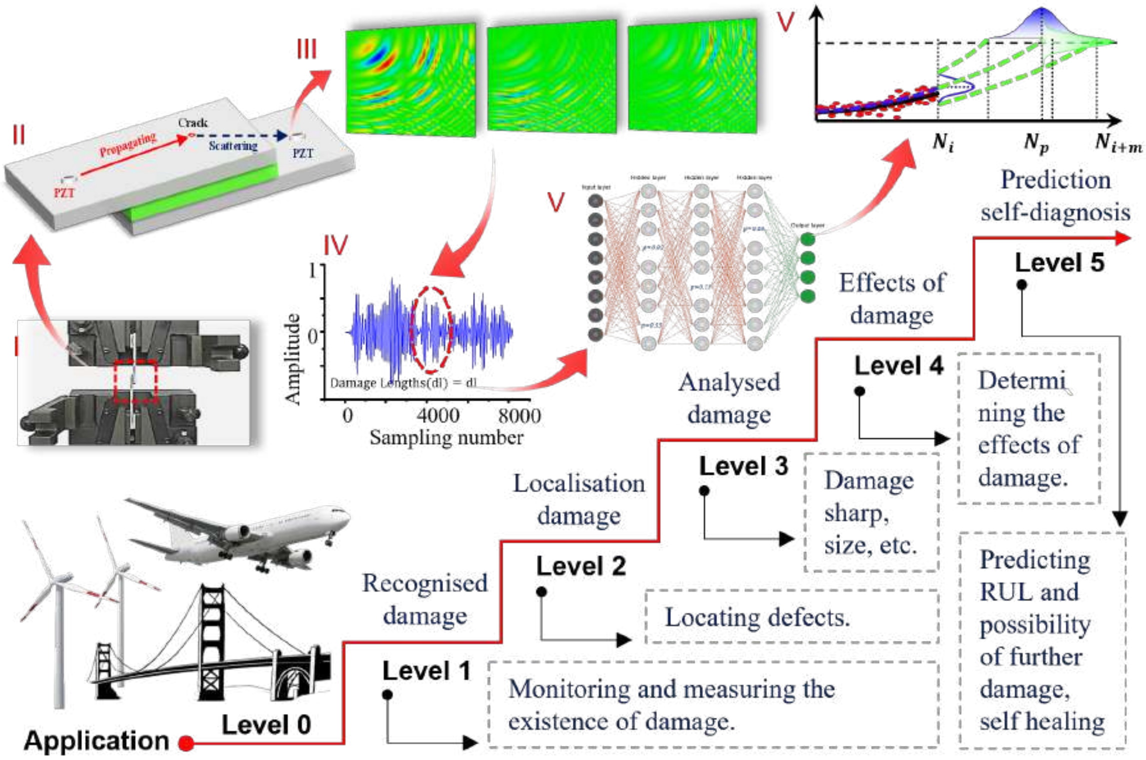

Figure 2.2 An overview of the technical level of SHM technology and the roadmap for implementing advanced SHM in this dissertation.

2.2.2 Guided waves

GW are formed when acoustic waves reflect and propagate repeatedly between discontinuous interfaces, such as the upper and lower boundaries of a solid plate. They travel within the waveguide at ultrasonic frequencies and are accompanied by complex dispersion. In a homogeneous medium, shear waves and longitudinal waves propagate independently as body waves in different directions. Fig. 2.3 illustrates the propagation characteristics of GW in a plate structure, where mode conversion occurs due to elastic interactions within the structure.

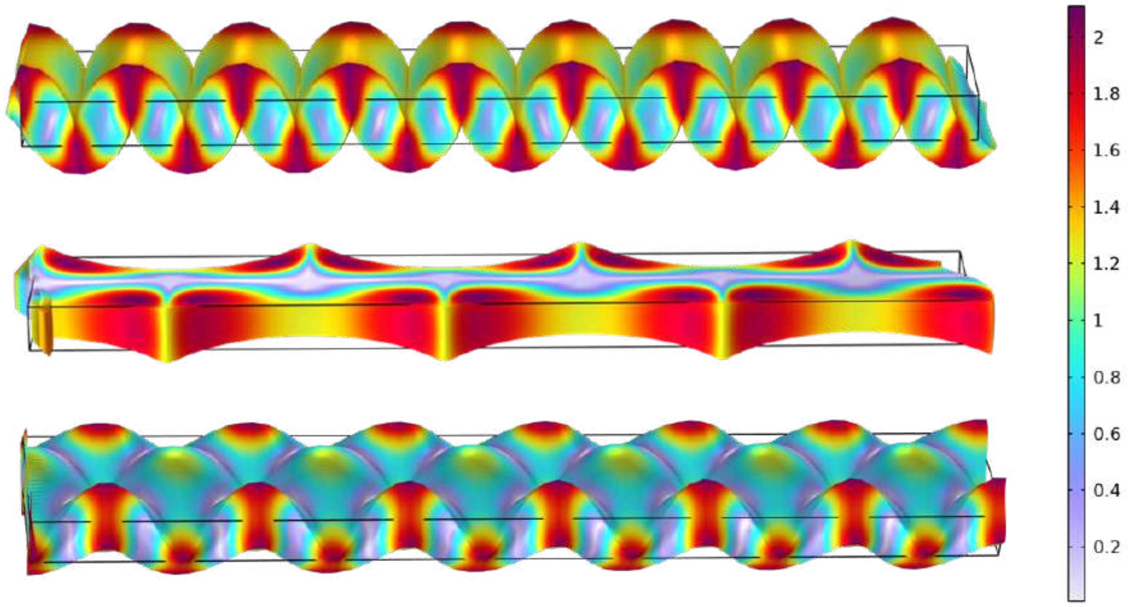

Figure 2.3 Shear waves, longitudinal waves and mixed waves in structures.

The thickness of the thin plate is significantly smaller than its length and width and is comparable to the wavelength. Consequently, ultrasonic waves undergo continuous reflection between the upper and lower surfaces, leading to mode conversion between longitudinal and shear waves. Part of the wave energy propagates as an in-plane horizontal shear wave, while the remainder forms out-of-plane Lamb waves. The propagation modes and characteristics of both wave types are depicted in Fig. 2.4.

It is assumed that there is a certain initial excitation source in the infinite plate to excite the GW signal, and the signal can be detected at any location in the plate. The time-space wave-field $Y(t,x)$ when GW reaches the position x can be calculated as follows [19]:

$$Y(t,x) = Ae^{-j(\omega t-k(\omega)x)} = \frac{1}{2\pi}\int_{-\infty}^{+\infty} F(\omega)e^{j(\omega t-k(\omega)x)}d\omega, \tag{2.1}$$

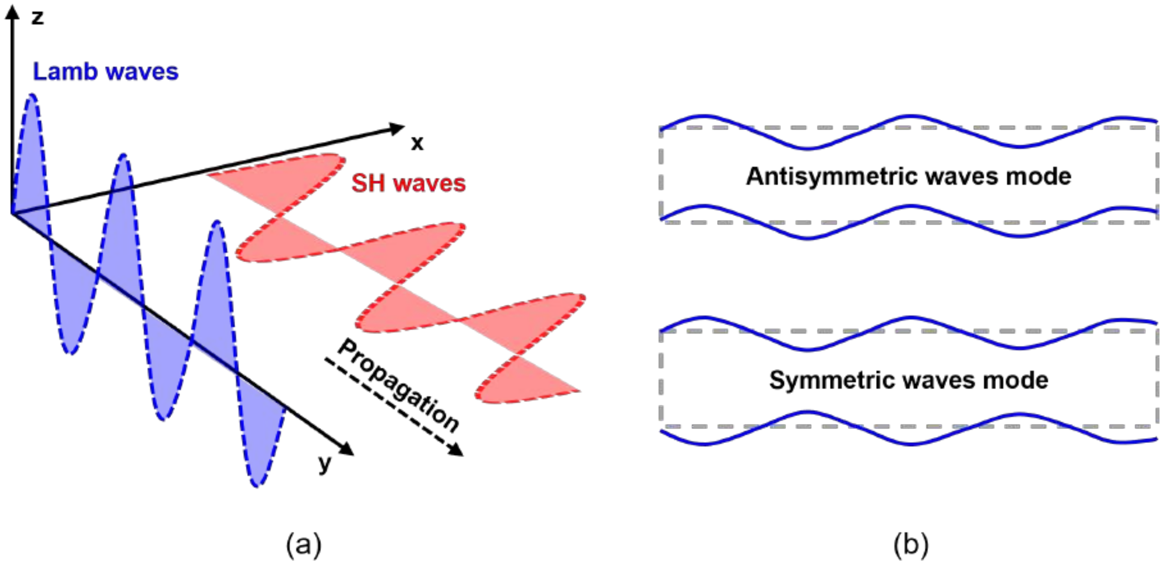

Figure 2.4 Wave propagation behaviour of SH and Lamb waves (a), and illustration of wave modes(b).

where $k(\omega)$ is the wavenumber of GW, A is the amplitude of GW and $F(\omega)$ is the FFT of an input signal $f(t)$. The frequency spectrum signal of $Y(t,x)$ is $Y(\omega,x)$, which can be calculated as follows:

$$Y(\omega,x) = F(\omega)e^{-jk(\omega)x}. \tag{2.2}$$

Based on the equations presented above, the nonlinear relationship exists between wavenumber and frequency during GW propagation, primarily due to the presence of exponential terms. As a result, dispersion inevitably occurs during wave propagation. According to the principles of elastic mechanics, the dispersion equation for GW propagating in an isotropic material can be expressed as follows:

$$\frac{\tan h\alpha}{\tan h\beta} = -\left[\frac{4\alpha\beta K^2}{(K^2-\beta^2)^2}\right]^{\pm 1}, \tag{2.3}$$

where h denotes the thickness of homogeneous media. K denotes the wavenumber and can be calculated by $K = \frac{\omega}{C_p}$. α and β are calculated by the following equations:

$$\alpha = \sqrt{\frac{\omega^2}{C_S^2} - K^2}, \tag{2.4}$$

$$\beta = \sqrt{\frac{\omega^2}{C_L^2} - K^2}, \tag{2.5}$$

where the C_p , C_L and C_S respectively represent the phase, shear wave, and longitudinal wave velocities of GW. Fig. 2.5(a) presents the evolution of the phase velocity of GW during propagation in carbon-fiber reinforced polymer (CFRP) as a function of frequency and thickness product [13]. Additionally, tuning curves for GW propagation have been computed under excitation with a 10 mm diameter piezoelectric transducer (PZT), demonstrating amplitude attenuation of GW across various frequencies as shown in Fig. 2.5(b). The normalized tuning coefficient (Normalized TC) is used to evaluate the efficiency of GW excitation at different frequencies. It is obtained by normalizing the wave amplitude relative to its maximum value. The excitation used in this study is a five-cycle tone burst signal with a central frequency ranging from 50 to 300 kHz. The adherend is two 1 mm thick CFRPs, and the adhesive is two-component epoxy resin.

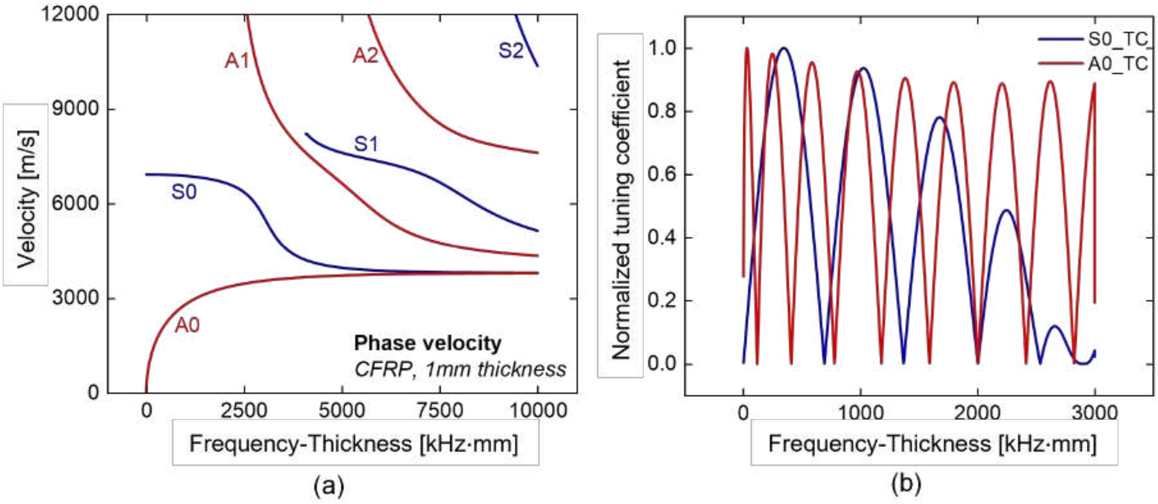

Figure 2.5 The group velocity and amplitude of GW propagating in CFRP thin plates change with frequency: (a) normalized tuning coefficient (TC) as a function of frequency for GW in a 1 mm-thick CFRP plate with a 10 mm PZT transducer.

There are various sensors for generating and receiving Lamb waves, such as PZT transducers [20, 21], while scanning laser Doppler vibrometery (SLDV) [22, 23] are also commonly used for full wave-field measurement. If GW are excited using PZT actuators without any signal pre-processing, multiple wave modes and dispersion effects will become more pronounced as the propagation distance increases. The resulting signal exhibits complex dispersion characteristics [24], making it difficult to intuitively extract damage information. To avoid such issues in SHM introduced by the dispersive nature of GW, various methods for mode separation and dispersion compensation have been proposed [25–27]. Zeng et al. [28] developed a dispersion-free restoration technique by applying pre-compensation and post-compensation strategies to the excitation signal. Harley et al. [29] utilised a frequency–wavenumber representation derived from GW propagation modelling and sparse sampling theory, and addressed multi-path interference using an ℓ_1-norm optimisation framework. Wang et al. [30] employed mode separation for dispersion compensation through received signal processing. Kudela et al. [31] integrated dispersion compensation into a phased array focusing algorithm, significantly improving imaging resolution. Cheng et al. [32] proposed advanced techniques for localising damage in plate-like structures by controlling GW propagation paths. In addition, Su et al. [33] introduced an SHM methodology that combines GW analysis with ML techniques to enable quantitative evaluation of through-thickness cracks in plate structures. Blachowski et al. [34] used modal and ultrasonic methods to detect bolt loosening in steel structures, showing that higher modes and proper sensor placement are key to identifying connection damage.

These studies have addressed the limitations of GW application in damage detection from three key perspectives: excitation, sensing, and signal processing. This dissertation focuses on damage detection using GW, with particular emphasis on the methodologies employed for damage diagnosis of adhesively bonded composite structures. The following sections provide a detailed overview of these approaches.

2.2.3 Damage detection based on guided waves

The GW is an essential method for detecting structural damage. Subsection 2.2.2 explains the principles of GW propagation and their modelling. GW propagation in solid structures demonstrates complex elastic wave behavior, especially when encountering structural and material discontinuities, such as boundaries, damage, or delamination. These discontinuities can significantly influence wave propagation through reflection and scattering, as illustrated in Fig. 2.6(a).

Two commonly used SHM techniques for damage detection using GW are the pitch–catch and pulse–echo methods. The selection of an appropriate technique depends on the sensor configuration and the specific testing conditions. In the pulse–echo approach, a single sensor is used to both excite and receive GW. As the wave propagates through the structure, encounters with reflective interfaces, e.g., crack or delamination, result in partial or full reflection of the wave energy. These scattered signals are captured by the same sensor, enabling the identification of structural irregularities.

In contrast, the pitch–catch method utilises two separate sensors: one for exciting the GW and the other for receiving it after interaction with the specimen or any reflective interface.

Fig. 2.6(b) presents a schematic illustration of both techniques, highlighting the interaction of GW with various structural interfaces. The key distinction between these methods depends on whether lies in the use of separate sensors for excitation and reception.

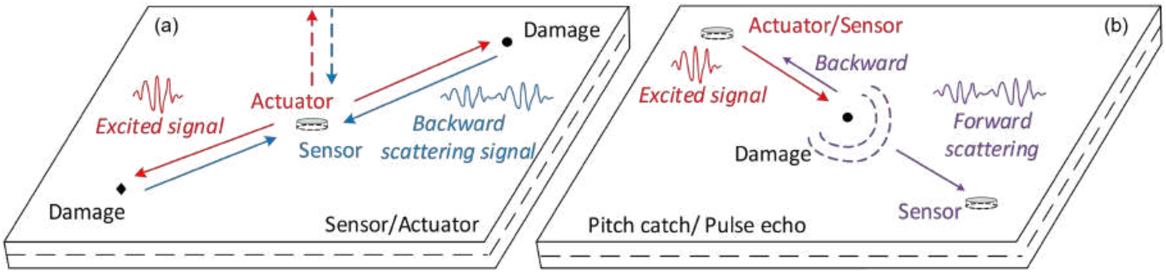

Figure 2.6 Diagram of the experimental method for damage detection using GW: (a) Sensing and actuating, (b) Pitch-catch and Pulse-echo.

The research on damage analysis of the adhesively bonded zone of composite structure using GW is mainly carried out in a pitch-catch method. The use of a single PZT transducer for both excitation and sensing in the pulse-echo method leads to rapid mode conversion, which complicates damage analysis, especially in small-sized structures. Therefore, the pitch-catch method is generally used by placing two PZTs on both sides of the bonding zone to assess its health status.

In practical applications, cracks in adhesive joints are typically complex and nonlinear, arising from stress concentrations and fatigue loading. Environmental conditions such as temperature, humidity, and ultraviolet exposure further accelerate bond degradation. Additionally, GW propagation in composite structures is complicated by phenomena including damage-induced scattering, boundary reflections, and mode conversions. These factors collectively pose significant challenges for GW-based SHM systems. Therefore, developing detection schemes tailored to specific damage characteristics is essential for improving diagnostic accuracy in complex wavefields.

Recent studies have proposed various strategies to improve damage localisation and quantification. For instance, phased array (PA) techniques have been extensively explored in the SHM of large composite assemblies. Rocha et al. [35] proposed a GW-based SHM strategy utilising PZT phased array systems to enhance the low signal-to-noise ratio typically observed in conventional PZT network configurations. Yang et al. [36] developed a signal processing framework based on the frequency response function, implementing a “single-input, multiple-output” configuration to enhance PA performance. Xu et al. [37] introduced a nonlinear Lamb wave PA approach for micro-damage imaging, utilising second harmonic responses to detect closed fatigue cracks. This methodology proved particularly effective in revealing localised acoustic nonlinearities associated with incipient damage. Yuan et al. [38] investigated the reverse-time migration imaging method for evaluating in-plane damage, achieving precise imaging of damage parallel to a linear array. Ostachowicz et al. [24, 39] explored sensor optimisation layouts and damage localisation of piezoelectric sensors on flat plate-like structures, with tests conducted on aluminium alloy and carbon fibre-epoxy composite specimen plates. Tavares et al. [40] proposed an integrated framework that combined SLDV data and ML to identify the damage in composite structures. They obtained the numerical simulation data by integrating finite element method (FEM) in the hybrid methods, which enriches the damage detection methodologies in transfer learning.

Effective signal processing techniques are essential for extracting damage-related features from recorded GW responses. Yu and Giurgiutiu [41] employed a non-uniform beamforming method to achieve rapid full-field scanning and damage localisation in large-scale metallic and composite plates. Yue et al. [42] proposed a GW imaging technique based on particle swarm optimisation, using binary histograms of particle distributions for visualising damage. Gruber et al. [43] introduced a time-reversal imaging method combined with multiple signal classification (MUSIC) to analyse complex, multiply scattered wavefields, enabling high-resolution imaging of multiple defects. Similarly, Wang et al. [44] developed a digital time-reversal imaging approach within distributed sensor networks, offering effective localisation and size estimation of structural damage. Sohn et al. [45] advanced a baseline-free damage detection technique using enhanced time-reversal processing for composite plates. More recently, Y. Yu et al. [46] developed a weighted delay-and-sum imaging algorithm using a denoising autoencoder to extract salient features and suppress noise, demonstrating strong robustness with limited input data. Luo et al. [47] proposed the hybrid BNN model, which integrates probabilistic modelling and DL for Lamb wave-based damage detection in composites. This approach improves noise tolerance and mitigates overfitting. Yuan et al. [48] introduced an integrated MUSIC array method that combines impedance curve filtering with co-cured PZT technology, significantly improving detection stability in composite structures. Xu et al. [49] proposed a focused MUSIC algorithm based on virtual time-reversal for baseline-free Lamb wave localisation in isotropic materials, and its effectiveness was validated experimentally on aluminium plates.

The above studies summarise mainstream GW-based damage detection techniques, ranging from conventional signal compensation schemes to more advanced methods incorporating ML, DT, and hybrid modelling frameworks. These approaches reflect the evolution of SHM methodologies, particularly in addressing the challenges of damage localisation and quantification under complex structural conditions.

2.3 Remaining useful life prognosis model

Currently, the RUL of composite structures is primarily predicted using ML approaches [50–53]. The observed variability across studies is primarily caused by input data and network architectures. Input data are influenced by detection methods and signal preprocessing strategies [54]. Recent efforts have focused on enhancing fault recognition through PA techniques to improve GW-based damage detection [36, 55]. This dissertation employs a GW-based damage detection method, with preprocessing centred on waveform decomposition and damage feature extraction, accounting for signal dispersion and multi-mode interference. The advantage of this approach lies in its direct correlation with damage location, supported by signal pre-compensation and post-processing techniques [28]. However, PA methods are not well-suited to SLJ structures due to sensor placement constraints and spatial limitations [39]. Therefore, a multi-sensor strategy [6] is adopted to analyse damage location based on the time of flight (ToF) [56, 57]. For RUL prediction, most studies utilise NN, particularly LSTM networks [58, 59], which are well-suited for time-series data due to their long-term memory capabilities. However, LSTM models face limitations when handling highly complex or long sequences. To address this, hybrid models have emerged, including LSTM–recurrent neural network (RNN) [60], LSTM–CNN [61], and LSTM–particle filter networks [62], which improve robustness and feature representation. Optimised variants of LSTM have shown promising results in processing time series [63], although most have been validated on systems like lithium-ion batteries and C-MAPSS engines [64], offering limited applicability to bonded composite structures.

The data-driven approach based on DL stands out as a highly effective method for SHM and RUL prognosis [65–67]. DL models offer a distinct advantage in processing extensive damage data and efficiently extracting damage features, making them particularly suitable for tasks such as GW signal analysis. The adaptability of DL models in categorizing diverse input data labels, coupled with their enhanced robustness relative to the CNN, significantly augments their efficacy in RUL prediction. Additionally, these models can effectively classify preprocessed data into various fault modes and accurately identify the damage characteristics [68–71]. In particular, RNN or LSTM demonstrate effectiveness in modelling time-dependent data and predicting future states, such as RUL and EoL. CNN excels in processing spatial data, including failure image analysis, thereby offering significant advantages for training with full-wavefield damage images. Additionally, ML models also exhibit strong transferability, enabling knowledge gained from training on one composite structure model to be effectively applied to predictions for other structures, as highlighted in the literature [72, 73]. However, a single NN exhibits several drawbacks in the application process of RUL prognosis. For instance, in the preprocessing of measured GW signals, NN models tend to be overly simplistic, lacking integration with the knowledge of damage mechanics, and inadequate representation of crack propagation information in damaged areas. Yuan F-G et al. [74] attempted to integrate GW technology, the cohesive zone method (CZM) theory, and the Markov Chain Monte Carlo sampling theory to propose a comprehensive RUL prediction framework for bonded metallic structures. This approach aimed to amalgamate mechanics with data-driven techniques, generating probabilistic output results accompanied by quantitative uncertainty. Słoński [75] used DL and digital image correlation to detect cracks and measure strain in concrete crane beams, enabling non-destructive and accurate condition assessment. Nazarko et al. [76] applied NN to process Lamb wave signals for early damage detection in aluminium and composite materials, showing good performance even with low-resolution data. Loutas et al. [52, 77] integrated the statistical method with the data from the AE method to generate more accurate RUL prediction results. They proposed a non-homogeneous hidden semi-Markov method to quantify uncertainty and enhance the accuracy of the RUL predictions [78]. The aforementioned hybrid models are based on the integration of ML techniques with probabilistic methods, and are essentially data-driven approaches for RUL prediction. This represents a significant research direction in RUL estimation. However, in recent years, another emerging approach is the use of DT, which aims to enhance prediction accuracy by integrating data-driven insights with physics-based modelling. DT-based methods offer significant advantages in handling large datasets [68, 79–81], constructing physical models, and interacting with simulation models. Currently, DT-based SHM and NDT primarily encompass two major aspects. The first aspect involves using a 3D virtual-physical interaction model based on DT for multi-level damage diagnosis of composite materials [82, 83]. The other involves employing a data management information system based on the DT method to facilitate information interaction and data processing with the physical model [84, 85]. DT-based research represents an advancement over current data-driven models, offering increased complexity and adaptability [86]. Meanwhile, this approach uses physical data to update simulation model parameters in real time, making it particularly suitable for tasks such as damage diagnosis, RUL assessment, and EoL prediction. In recent studies, efforts have been made to integrate dynamic sensor data and physical models into a DT framework to enhance reliability prognosis for in-service structures, thereby addressing uncertainties arising from both service loads and structural variability. For example, the method proposed in [87] effectively captures cumulative crack growth and extends the application of SHM to fatigue damage assessment in multilayer composite structures. Similarly, the works in [88, 89] introduce a DT-driven fault diagnosis strategy that integrates the Bernoulli equation with loss, control, and state parameters, forming a comprehensive model for addressing compound failure scenarios in complex systems.

FM provides a fundamental methodology for analysing fatigue crack growth. Classical models such as the Paris law and its extended formulations are extensively used in engineering to predict fatigue crack propagation and estimate RUL [10, 90]. Recent studies increasingly apply data-driven methods to identify the parameters of the Paris law, thereby enabling fatigue life prediction [15, 91–93]. However, acquiring high-quality data through fatigue testing remains challenging and costly, posing limitations on the development of reliable algorithms. To address this, researchers have integrated advanced sensing technologies with data-driven approaches [94, 95].

While the quantitative RUL prediction method based on GW and BNN is practical and accurate, it tends to overlook uncertain factors (uncertainty quantification) in the prediction results. A new fatigue crack growth prediction method, combining a particle filtering algorithm and GW, has been proposed to improve prediction accuracy [96], but determining the optimal number of particle prognosis models for predicting fatigue crack growth remains a problem. Therefore, more hybrid models are proposed to predict damage, such as multiple-NN [97, 98], DL [99], DT [13, 82, 84]. The hybrid models proposed in these studies effectively address the limitations of single-model approaches by achieving accurate and stable RUL predictions, even when the experiments are repeated multiple times.

2.4 Structural health monitoring based on digital twin technology

DT is increasingly applied across industries such as civil infrastructure, construction, and aerospace, functioning as an integrative platform for multi-model fusion. DT involves the acquisition of digital data either through sensors or derived from the physical system, which is then processed using specialised algorithms to enable remote monitoring, control, and visualisation. The technology supports functions such as information exchange, simulation, predictive modelling, and optimisation. In fields such as aerospace and civil engineering, DT has already demonstrated substantial utility in applications including service life monitoring, failure inspection, and disaster prevention and early warning systems [100–103]. Using extensive datasets generated through a measurement system, DT facilitates real-time combination between measured data and simulation models. Throughout the entire SHM lifecycle, this capability enables dynamic model correction, real-time condition assessment, and predictive safety management, thus establishing a comprehensive system for continuous monitoring, evaluation, and early warning.

The primary function of DT technology in the context of SHM for adhesively bonded composite materials is to serve as a comprehensive framework for failure analysis and predictive maintenance. In contrast to expert systems or hybrid ML architectures, the DT framework places a stronger emphasis on the integration of physical and virtual systems. Conventional failure detection and RUL prediction methods are often constructed as independent modules. For instance, experimental data are used to build training datasets for virtual models, which subsequently perform specific prediction tasks. However, such systems typically lack full integration, although the modules may interact during execution, there is generally no dynamic feedback mechanism among them.

The emergence of DT has overcome the limitations of conventional modular systems by facilitating the integration of physical and virtual domains. Through continuous synchronisation, parameters derived from the physical system are dynamically updated within the virtual environment to optimise overall system performance. For example, Vivek et al. [104] proposed an ML -based DT framework, enhancing computational efficiency of huge volume data. This approach employs linear dimensionality reduction algorithms and NNs to generate approximations of real-world signals. Milanoski et al. [105] introduced a multi-level damage diagnosis strategy based on a data-informative DT model, combining field data acquired via fibre Bragg grating sensors with finite element analysis (FEA). Also, Kim et al. [106] developed a physics-based DT model update method and a twin-crack identification technique for assessing fatigue damage in riveted lap joints. Their method incorporates Lamb waves to capture the uncertainty associated with crack propagation paths. In another study, Edwards et al. [107] established a DT system for damage evaluation and life prediction in welded structures, integrating sensor-based measurements with big data analytics. This system offers an innovative route for damage quantification while enhancing the accuracy of RUL prediction. Furthermore, Zhao et al. [12] proposed a DT model that integrates multiple SHM technologies, employing a semi-analytical FEM in conjunction with AE techniques to localise damage in wind turbine blades. Rather than relying on data-driven ML approaches, their method establishes explicit analytical correlations between the measurement and simulation, thereby improving the accuracy of damage localisation.

The integration of DT technology with SHM not only facilitates diagnostic tasks, such as damage quantification and crack identification, but also plays a vital role in predicting the RUL based on experimental data. The use of DL techniques is currently the most common approach to achieving the prediction process. Based on DT technology, predictive networks can learn from both experimental and simulation data, thereby enhancing the accuracy of prediction results. Ye et al. [108] employed DT technology for structural component inspection and damage prediction in the bridge inspection process. Hielscher et al. [99]

utilised DT techniques to visualise strain outputs from fibre optic sensors, comparing and evaluating structural responses over time to provide references for optimising maintenance strategies. Seshadri et al. [14] combined experimental and model data to manage the full lifecycle of damaged aircraft blades, including damage diagnosis and lifespan prediction. Zhu et al. [109] updated parameters through structural response data monitoring to achieve monitoring and predictive behaviour throughout the lifecycle. Rather than directly modifying parameters within the model, this method utilises an intermediate model for conditional analysis and parameter calculation, employing Bayesian methods to quantify uncertainty. Al-Hijazeen et al. [110] integrated DT technology with the support vector machine algorithm to monitor the health condition, enabling prediction and prevention of bridge damage or collapse. Giannaros et al. [83] developed high- and low-fidelity FEM to simulate the dynamic response of helicopter composite sandwich structures under bird-strike impact. These models were validated for accuracy and ultimately served as virtual tools to support future DT-assisted damage detection technologies. Wang et al. [82] proposed a DT-driven approach combining XFEM, high-precision approximation models, and BNN to achieve efficient and accurate structural fatigue life prediction. Zhang et al. [6, 13] proposed an integrated framework that connects ML and FM to achieve RUL prognosis for adhesively bonded structures. The difference between this model and a general DT model lies in the addition of a FM module and a data filtering module to the DT framework. These studies employ predictive DT technology for structural damage assessment from diverse perspectives, offering valuable insights for enhancing the precision of structural operation and maintenance.

Additionally, the emergence of new technologies is significantly influencing the application of DT within the SHM domain. Dang et al. [111] proposed a DT framework for SHM that leverages cloud computing and DL. By integrating internet technologies with cloud-based infrastructure, this approach facilitates the broader deployment of DT, effectively enabling real-time monitoring and proactive maintenance strategies. Lai et al. [112] achieved high-precision DT computation by employing multifidelity surrogate models, which were validated through experiments conducted on aircraft wing structures. In another study, Hu et al. [113] incorporated internet of things and digital signal processing technologies to autonomously acquire sensor data in real time within a building information modelling environment. Their method addresses the challenge of visualising structural behaviour and conducting damage analysis across various locations within structural components. All in all, these advancements underscore the expanding potential of DT in SHM, particularly in enhancing real-time monitoring, predictive maintenance, and structural diagnostics through the integration of advanced technologies. As research in this area progresses, further innovations in cloud computing, artificial intelligence, and internet of things are expected to accelerate the evolution and practical adoption of DT applications in structural health monitoring.

2.5 Summary

This chapter introduces three key aspects. First, it discusses damage detection technology based on GW, which constitutes one of the most widely adopted techniques in the field of SHM. A review of current research indicates that the primary challenge hindering its large-scale application lies in the effective analysis of the collected GW data, as dispersion and multimodality present significant obstacles to its widespread adoption.

Next, this chapter explores technologies for predicting RUL, focusing on several commonly used approaches, including NN, ML, statistical methods, and numerical simulations.

Finally, the chapter examines the application of DT technology in the SHM domain, introducing how it enhances SHM by enabling more accurate and efficient damage detection.

Chapter 3

Remaining useful life prognosis based on data-driven methods

3.1 Introduction

This chapter not only reviews existing methods in the literature but also explores potential improvements to adapt these approaches for damage detection and life prediction in bonded composite structures. The discussion covers CNN, RNN-LSTM, and BNN models, along with techniques for uncertainty quantification. Autoencoders are also introduced as a means of reducing high-dimensional input data. In addition, DT technology is addressed, including its application in this study for both damage detection and RUL prediction. The chapter concludes by presenting evaluation metrics for ML-based predictions and approaches for uncertainty quantification.

3.2 The framework of remaining useful life prognosis using data-driven techniques

RUL prognosis is a continuous, long-term predictive task. As illustrated in Fig. 3.1, the objective is not only to ensure the reliability of prediction results but also to support appropriate maintenance, which represents the ultimate goal of RUL prediction and prognosis health management (PHM). This dissertation focuses on signal acquisition, damage quantification, and RUL prognosis in the adhesive zone. The overall process is systematically divided into five key technical stages. First, GW are excited and acquired using PZT sensors bonded to the specimen surface. The registered data are then analysed to extract damage-related features under different damage conditions. Subsequently, the correlation between the damage signal and the baseline signal is calculated to determine the damage indicators (DI), thereby enabling the quantification of damage extent. The quantified damage extent is used as a label for RUL training dataset. Next, uncertainty quantification is performed on the predicted RUL to enhance the credibility of the prognosis. Finally, based on the uncertainty quantified prediction results, the current damage evolution of the structure is assessed to guide maintenance and operational decision-making.

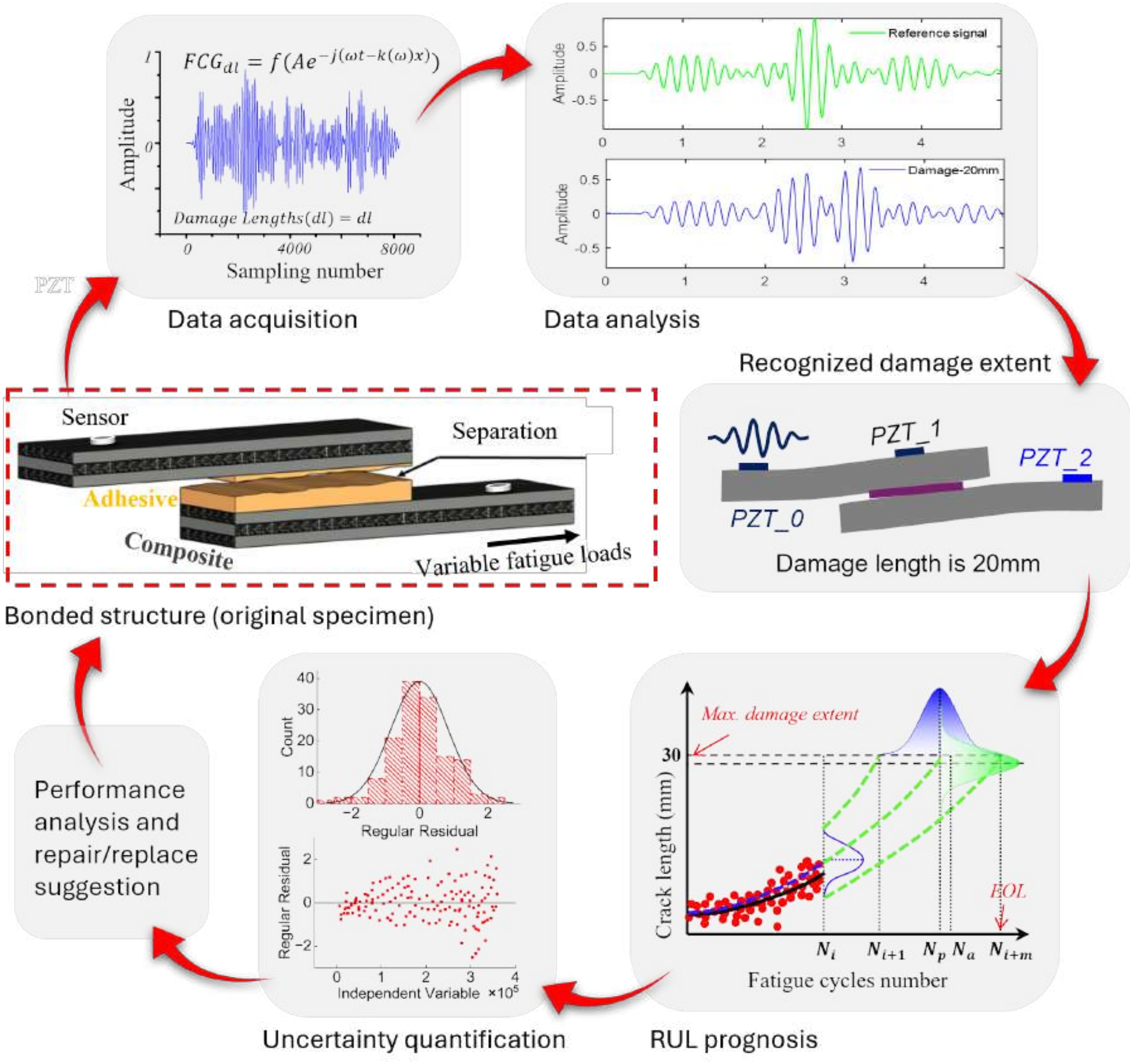

Figure 3.1 Framework for RUL prognosis and health management of bonded composite structures based on data-driven technology.

3.3 Neural networks in remaining useful life prediction

This section introduces NN related to SHM and NDT, which are widely used for training damage data and predicting RUL. Alongside the introduction of these networks, their basic architectures have often been modified to better suit prediction tasks.

3.3.1 Recurrent neural network

The RNN is a classical NN architecture particularly effective for sequential data. It is capable of capturing temporal dependencies, making it well suited for analysing fatigue damage data that involves time-series information. RNN also represents one of the earliest NN models applied to RUL prediction tasks.

In the context of lifespan for composite structures, let x_t denote the crack length observed at fatigue cycle t. The primary objective of the RNN model is to estimate the damage level at cycle $(t+1)$. The probability of a particular damage state occurring at cycle $(t+1)$ is expressed as follows:

$$(x_1, x_2, \ldots, x_{t-1}, x_t) \sim p(x_{t+1}). \tag{3.1}$$

The first step of establishing an RUL prognosis model is to find a $p(\text{damage})$ that represents future damage information. In this manner, future data can be predicted based on historical observations. This relationship can be further extended using conditional probability, such that:

$$p(x_{t+1}) = p(x_1) \cdot p(x_2|x_1) \cdot \cdots \cdot p(x_t|x_1, x_2, \ldots, x_{t-1}). \tag{3.2}$$

Using prior data to estimate future states introduces a key challenge: as the number of predicted fatigue cycles increases, the value of t grows large, making multivariate probability prediction computationally intractable, particularly in long-duration fatigue processes relevant to RUL prediction. To address this issue, a common approach is to apply the Markov assumption. This probabilistic model for sequential data posits that the current state depends only on a finite number of prior states and is conditionally independent of all earlier states. Accordingly, the probability of damage at a given cycle t can be defined as:

$$p(x_t|x_{t-1}, x_{t-2}, \ldots, x_1) = p(x_t|x_{t-1}, x_{t-2}, \ldots, x_{t-n}), n < t. \tag{3.3}$$

By adjusting the order n of the Markov chain, the dependency of the current state on previous states can be controlled, thereby reducing computational complexity. For example, if $n = 2$, the model becomes a second-order Markov chain, in which the current state depends only on the two most recent states. As such, Markov chains are used to keep a balance between computational efficiency and predictive accuracy in time-dependent applications.

Through this approach, complex time-series data are transformed into a formulation governed by the static hyperparameter n. The conditional probability $P(x_t \mid x_{t-1}, \cdots, x_{t-n})$ can be modelled using NN methods. A network is constructed that accepts n-dimensional input (i.e., $(x_{t-n}, \cdots, x_{t-1})$) with a single output node that predicts the value of x_t. Supervised training is then employed to optimise the model parameters.

The general architecture for damage detection in plate-like structures using RNN [24] is illustrated below. Unlike a standard fully connected NN, RNN incorporates feedback loops within the hidden layers. This feature enables the hidden state at time t to depend not only on the input damage data at that time step but also on the hidden state from the previous cycle $(t-1)$. Accordingly, the RNN structure can be mathematically described by Eqs. (3.4) and (3.5),

$$h_t = \sigma(W_{xh}x_t + W_{hh}h_{t-1} + b_h), \tag{3.4}$$

$$y_t = \text{softmax}(W_{hy} \cdot h_t), \tag{3.5}$$

where σ is an activation function, commonly chosen to be the tanh or rectified linear unit (ReLU) function. In this context, the softmax function is used to convert the output $(W_{hy} \cdot h_t)$ into a probability distribution for different classes, which makes it useful for classification tasks. Given a vector z of real values, the softmax function is defined as:

$$\text{softmax}(z_i) = \frac{e^{z_i}}{\sum_j e^{z_j}}, \tag{3.6}$$

where z_i is the i-th element of the vector z. This function ensures that each output value y_t lies within the range $[0,1]$, and that the sum of all elements in y_t equals 1, thereby forming a valid probability distribution. In a standard RNN, the hidden state h_t is computed from the current input x_t and the previous hidden state h_{t-1}. The hidden state h_t serves as a memory mechanism, retaining information from prior time steps. By propagating h_t through one or more layers, the output y_t at the current time step is obtained.

During training, a loss function is employed to quantify the discrepancy between the predicted output and the ground truth. This loss is used to update the model parameters W_{xh}, W_{hh}, W_{hy}, and the bias term b_h via backpropagation. If the recurrent weight matrix is removed (i.e., setting $W_{hh} = 0$), the RNN reduces to a feedforward NN. In this configuration, the hidden state is updated solely using W_{xh}, and temporal dependencies are no longer captured, resulting in a model that lacks memory of previous states.

The RNN architecture for damage signal prediction is illustrated in Fig. 3.2. This typical RNN structure consists of an input layer, one or more recurrent hidden layers that capture temporal dependencies, and an output layer. The model introduced in [24] is trained to predict signal responses across different damage extent by learning the sequential patterns embedded in the GW data.

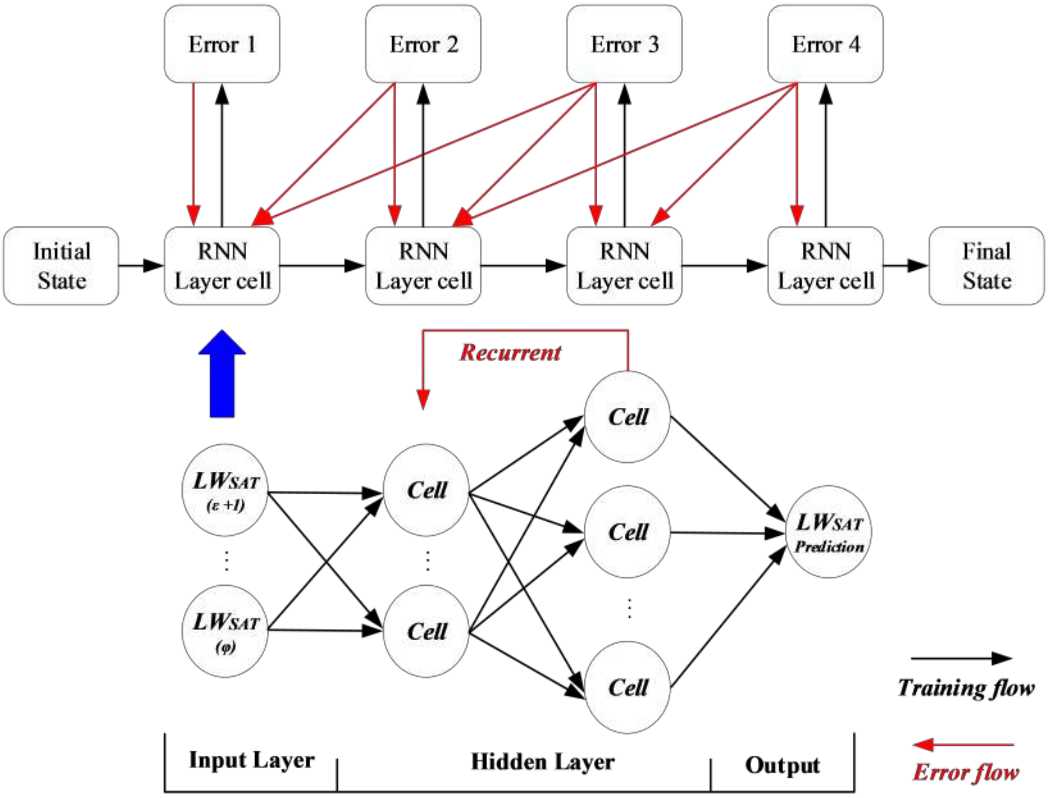

Figure 3.2 Classical architecture of the RNN model for predicting GW damage signal.

3.3.2 Temporal convolutional network

As one of the earliest models applied to RUL prognosis, the RNN has shown clear advantages in handling sequential data. However, its low computational efficiency and limited support for parallel processing have led many researchers to shift their attention to CNN. While classical CNNs are highly effective in processing spatial data, particularly images, they are less suited to time series applications. To address this limitation, this section introduces temporal convolutional networks as a means of adapting CNN for time-dependent problems.

A typical CNN architecture for RUL prediction is illustrated in Fig. 3.3. The model comprises an input layer, convolutional layers, pooling layers, fully connected layers, and an output layer.

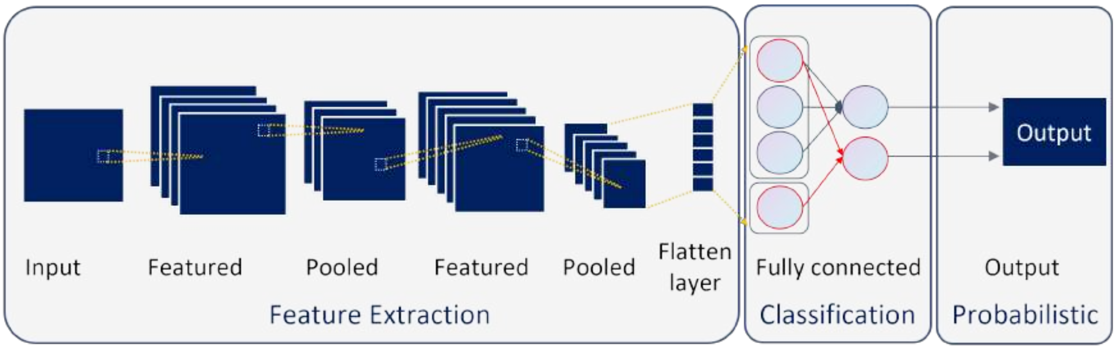

Figure 3.3 The typical CNN architecture for damage detection.

As the core of CNN, the convolutional layer is primarily responsible for feature extraction and computation on the input data. The convolution operation defined by the input and output is denoted as follows:

$$Y^l(m,n) = X^k(m,n) * H^{kl}(m,n) = \sum_{k=0}^{K-1}\sum_{i=0}^{I-1}\sum_{j=0}^{J-1} X^k(m+i,n+j)H^{kl}(i,j), \tag{3.7}$$

where X and Y represent the input matrix of the k-th layer and the output matrix of the l-th layer, respectively. The convolution kernel at the k-th row and l-th column is denoted as H.

CNN incorporates pooling layers between convolutional layers, primarily to reduce the dimensionality of feature maps, which reduces the risk of overfitting. The fully connected layer further compresses the extracted features for the final output. In forward propagation, the network sequentially computes the output of each layer, calculates the loss between the predicted output and the target function, and updates the weights to complete the training iteration. However, conventional CNNs are generally less effective than RNNs in handling time-series data, owing to their lack of temporal encoding and the absence of explicit connections between past and future states. Consequently, CNN is typically not used alone for RUL prediction. Enhancements to CNN models focus on enabling temporal feature extraction to better process sequential data.

Assuming the crack length at fatigue cycle t is obtained from testing, the objective of training the CNN is to predict the RUL at $(t+1)$. This requires the output y_t at time t to be influenced by historical data, including observations at $(t-1)$ and earlier. To address this, the improved CNN architecture has to allow each output at time t to be computed using information from both the current and previous, ensuring that all data used from time steps before t. To handle time-series problems, the network must possess a long-term memory mechanism capable of capturing patterns across extended time intervals. However, this typically requires a very deep architecture, which significantly increases computational complexity. To address this limitation, dilated convolution is introduced. This technique inserts a fixed convolutional operation unit F between adjacent layers, along with a dilation rate parameter that enlarges the receptive field of the convolutional kernels without increasing the number of parameters.

The dilation factor d controls the receptive field size of the enhanced CNN. When $d = 1$, the operation corresponds to a standard convolution. As d increases, the receptive field of the one-dimensional CNN expands, enabling the model to capture longer-term dependencies. This architecture allows deeper contextual understanding using a relatively shallow network. By adjusting the number k of dilated residual filters, various d values can be set to extract temporal features at different scales. The receptive field can be calculated as follows:

$$\text{Receptive Field} = [(k-1)\cdot d + 1]. \tag{3.8}$$

The relationship between different dilation rates and the number of NN layers is illustrated in Fig. 3.4. By appropriately increasing the parameters of the residual filters, the computational loading associated with deep network architectures can be effectively reduced. Furthermore, the incorporation of residual modules ensures dimensional consistency between the input and output of the CNN, thereby facilitating stable training and efficient information propagation through the network.

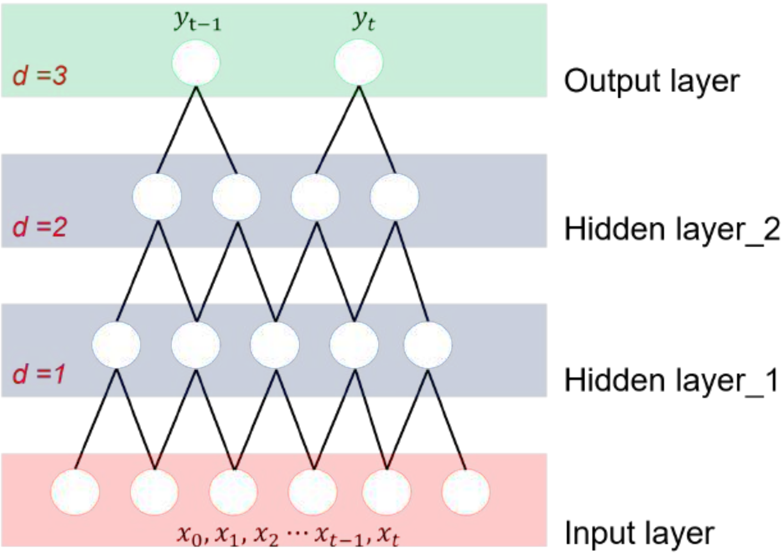

Figure 3.4 Temporal convolutional network structures corresponding to different receptive fields.

3.3.3 Long short-term memory network

The LSTM network was developed as an extension of the RNN, specifically designed to address its limitations in processing long time-series data. In many RUL prediction scenarios, it is necessary to analyse the cumulative damage at time t because only calculating based on damage at time $(t-1)$ is insufficient. A more accurate approach involves utilising all data from time 0 to $(t-1)$. This is particularly important because the initial damage state significantly affects the extent of the damage and the RUL of the composite. As a result, RNN is greatly limited when handling long time-series cases. To overcome this, the LSTM was proposed by Hochreiter [114] to explicitly avoid the long-term dependency problem. The ability to store long-term state data and information is a key feature of LSTM. Like all RNN, LSTM has a chain structure of repeating NN modules. LSTM not only possesses the memory capability for short-sequence data but also includes control units for storing long-term memory. In the RNN-LSTM hybrid model, the neurons result from a combination of logical operations and a tanh activation layer, as illustrated in Fig. 3.5.

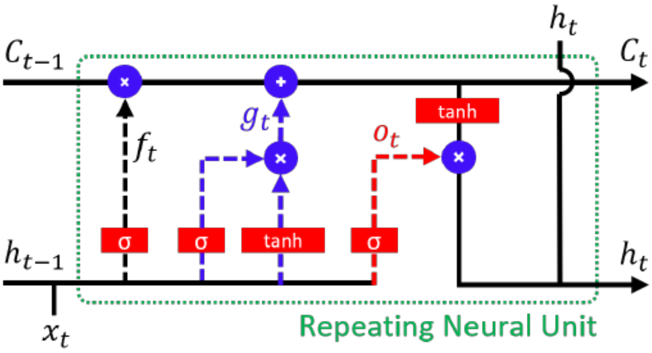

Figure 3.5 The typically LSTM repeating neural unit.

LSTM networks manage both long-term and short-term information through gated control units. These include the input gate, output gate, and forget gate, which regulate the flow of information into, out of, and within the memory cell. Specifically, the forget gate determines the proportion of the previous cell state at time $(t-1)$ that should be retained or discarded in the current state. The cell state of forget gate f_t is defined as follows:

$$f_t = \sigma\left(W_f \cdot [h_{t-1}, x_t] + b_f\right). \tag{3.9}$$

The forget gate serves as the core control mechanism in the LSTM architecture, regulating how much information from the previous state should be discarded. It operates by receiving the previous hidden state h_{t-1} and the current input x_t, which are first subjected to a linear transformation. This is followed by a sigmoid activation function that produces an output in the range $[0,1]$, representing the proportion of information to retain or forget. The forget gate is expressed as:

$$C_t = f_t * C_{t-1} + \sigma\left(W_i \cdot [h_{t-1}, x_t] + b_i\right) * \tanh\left(W_C \cdot [h_{t-1}, x_t] + b_C\right). \tag{3.10}$$

The cell state C_t forms the core of memory in the LSTM architecture. It determines how the previous state influences the current state by combining two ways: the retained portion of the previous cell state, regulated by the forget gate ($f_t \cdot C_{t-1}$), and the weighted update of the current input, controlled by the input gate ($\sigma(W_i \cdot [h_{t-1}, x_t] + b_i)$). This process is formulated as:

$$h_t = \sigma\left(W_o \cdot [h_{t-1}, x_t] + b_o\right) * \tanh\left(C_t\right). \tag{3.11}$$

The output h_t is the hidden state at the current cycle. It determines the output of the next state. As shown in Eq. (3.11), the output is controlled by the cell state C_t. Specifically, the output gate applies a nonlinear transformation to the cell state C_t using the tanh function, and then multiplies the result by the activation value of the output gate (obtained via the sigmoid function) to produce the final hidden state h_t.

Above is the forward propagation process of the LSTM. As a NN, back propagation of the error is essential. Let E be the loss function of the LSTM, then the error calculated from the output is described as follows:

$$\delta_t = \frac{\partial E}{\partial h_t} = \prod_{j=k}^{t-1} \delta_{o,j}^T W_{oh} + \delta_{f,h}^T W_{fh} + \delta_{i,h}^T W_{ih} + \delta_{\bar{c},j}^T W_{ch}, \tag{3.12}$$

where W_{oh}, W_{fh}, W_{ih}, and W_{ch} represent the weights of the outputs from different gates, which measure their respective contributions to the error. Expanding the Eq. (3.12) to the entire NN gives the following result:

$$\frac{\partial E}{\partial W_{fx}} = \frac{\partial E}{\partial h_{f,t}} \frac{\partial h_{f,t}}{\partial W_{fx}} = \delta_{f,t} x_t^T, \tag{3.13}$$

$$\frac{\partial E}{\partial W_{cx}} = \frac{\partial E}{\partial h_{\bar{c},t}} \frac{\partial h_{\bar{c},t}}{\partial W_{cx}} = \delta_{\bar{c},t} x_t^T, \tag{3.14}$$

$$\frac{\partial E}{\partial W_{ox}} = \frac{\partial E}{\partial h_{o,t}} \frac{\partial h_{o,t}}{\partial W_{ox}} = \delta_{o,t} x_t^T . \tag{3.15}$$

The hidden outputs of different gates are represented by h with subscripts. By calculating the partial derivatives, the error can be used to represent the back propagation process. The result of back propagation is to compute the error at each layer, then use gradient descent to continually update the weights, thereby updating the outputs of the forward computation. This process is repeated iteratively until the stopping criteria are satisfied.

3.3.4 Autoencoder hybrid networks

RUL prediction is a typical data-driven task that relies on large volumes of preprocessed input data, such as damage features, stress-strain (S-S) curve, and fatigue cycles, to ensure accurate forecasting. The preceding subsections outlined methods for handling sequential data. While RNN was one of the earliest models applied to RUL prediction, it has gradually been replaced by temporal convolutional networks and LSTM due to its limited ability to extract high-dimensional features from sequence inputs.

However, a common limitation among these networks is the lack of dimensionality reduction for input data. High-dimensional inputs impose significant computational demands, making dynamic hyperparameter tuning difficult. To address this, methods that integrate NN with efficient batch processing and dimensionality reduction have been proposed. One such method is the autoencoder, which compresses input data into a lower-dimensional representation and attempts to reconstruct the original signal. The model structure is shown in Fig. 3.6.

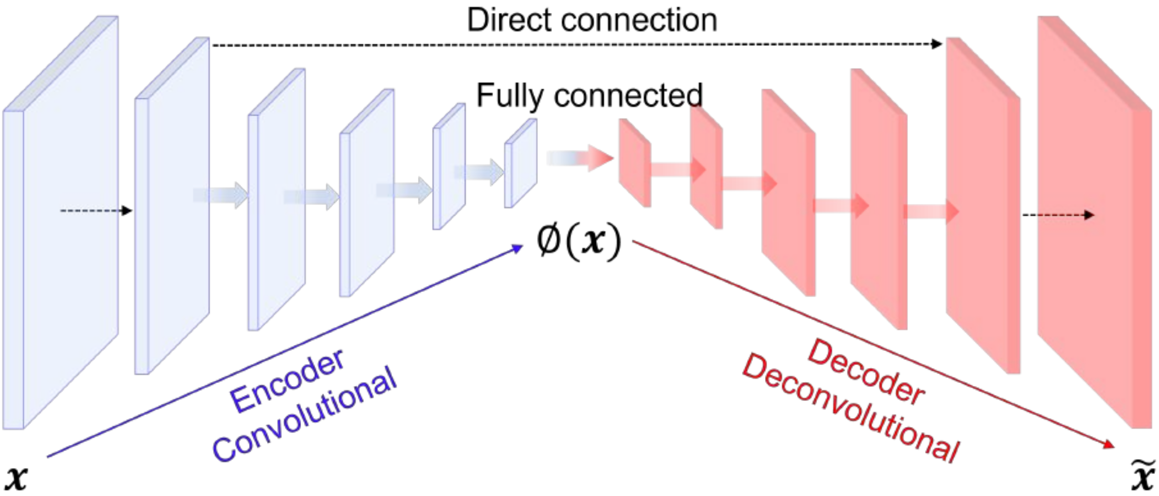

Figure 3.6 Diagram of the auto-encoding of input data by an autoencoder using a CNN as an example.

The autoencoder consists primarily of an encoder and a decoder. When applied it to process input data of RUL prediction models, its objective is to transform high-dimensional input data **x** into an intermediate representation $\phi(x)$, which is subsequently converted into a simplified version $\tilde{\mathbf{x}}$. The training goal is to ensure that the reconstructed output $\tilde{\mathbf{x}}$ closely approximates the original input **x**. In the context of RUL prediction, the autoencoder operates as an unsupervised NN that first encodes hidden features from large volumes of input data and then decodes them to reconstruct the original input.

The function of the autoencoder in preprocessing is analogous to that of principal component analysis. However, RUL models frequently involve high-dimensional inputs containing complex nonlinear relationships, where damage features cannot be represented as linear combinations of input variables. These nonlinearities can be effectively addressed by using nonlinear activation functions within the NN-based autoencoder. Owing to the strong function approximation capabilities of NN, the model can capture complex nonlinear transformations and extract representative high-dimensional features.

The encoder maps the high-dimensional input **x** into a lower-dimensional latent feature space. This transformation is achieved through a linear mapping followed by a nonlinear activation function, as explained in the following equation:

$$\phi(\mathbf{x}) = \sigma(\mathbf{W}_\phi \mathbf{x} + \mathbf{b}_\phi), \tag{3.16}$$

where $\mathbf{W}_\phi$ and $\mathbf{b}_\phi$ represent the weight and bias, and σ is the activation function (such as ReLU or Sigmoid). The core goal of the encoder is to extract the key features from the original input data while reducing the dimensionality of the data and retaining as much useful information as possible. The decoder is used to transform the low-dimensional feature **z** generated by the encoder back into a reconstruction $\tilde{\mathbf{x}}$ that is as similar as possible to the original input **x**.

The transformation carried out by the decoder is similar to that of the encoder and can be expressed by the following equation:

$$\psi(\mathbf{z}) = \sigma(\mathbf{W}_\psi \mathbf{z} + \mathbf{b}_\psi), \tag{3.17}$$

where $\mathbf{W}_\psi$ and $\mathbf{b}_\psi$ are the decoder parameters. Meanwhile, the autoencoder optimises its parameters through backpropagation so that the encode features can be restore the original input data.

The reconstruction loss function is introduced to evaluate the quality of the feature representations, which measures the difference between the reconstructed data and the original data. Using mean squared error (MSE) as the loss function, the total loss can be defined as:

$$\mathscr{L}(\phi,\psi) = \frac{1}{2}\sum_{i=1}^{N} \|\mathbf{x}_i - \tilde{\mathbf{x}}_i\|^2 = \frac{1}{2}\sum_{i=1}^{N} \|\mathbf{x}_i - \psi(\phi(\mathbf{x}_i))\|^2, \tag{3.18}$$

where $\mathbf{x}_i$ denotes the i-th sample, and $\tilde{\mathbf{x}}_i$ represents the reconstruction result from the decoder. By minimising the reconstruction loss, the parameters of both the encoder and decoder can be optimised to ensure that the features extracted by the encoder preserve as much information as possible from the original input.

There are various approaches to designing the encoder and decoder. If sufficient prior knowledge of the structural damage data distribution is available, it may be possible to construct explicit encoding and decoding functions based on this information. However, in most cases, the distribution of sample data is highly complex and cannot be easily inferred using analytical methods. As a result, NN are employed to learn the encoder and decoder directly, with their parameters updated automatically through backpropagation or other optimisation techniques. This data-driven approach is the most commonly adopted method in RUL prediction workflows.

3.4 Digital twin

DT has become a research hotspot in SHM, with increasing emphasis on integrating physical systems and virtual simulations to enhance the accuracy of RUL prediction. Compared to conventional RUL prediction methods, DT distinguishes itself by combining virtual model with physical model within ML-based frameworks.

The overarching goal of DT is to facilitate real-time monitoring and analysis of physical systems through virtual representations, supporting the assessment of fatigue damage, crack growth, and corrosion-induced failure in structures. However, constructing a full-scale virtual replica is often impractical and unnecessary. The acquisition of detailed geometric data and deployment of extensive analog/digital modules and sensor arrays for continuous microstructural monitoring are costly and may exceed practical requirements. As a result, recent research has shifted towards expert system-based DT frameworks that integrate multiple data sources to improve the accuracy of RUL prediction. Studies such as [13, 82, 89, 105] present comprehensive examples of DT applications in RUL estimation. These works primarily focus on integrating various NN architectures and combining numerical simulations with experimental validation. As a multi-physics, multi-scale, and probabilistic methodology, DT enables damage prediction and SHM by synthesising physical models, real-time sensor data, and historical records.

Crack propagation prediction represents one of the key applications of DT in SHM. Traditional numerical methods such as FEM, boundary element methods, and XFEM have been instrumental in crack analysis, though they are often limited by a lack of validation against empirical data. Integrating these simulations with real-world detection data has become a widely adopted DT strategy for RUL prediction. Additionally, the incorporation of surrogate models has improved the efficiency and reliability of crack propagation analysis. Fig. 3.7 illustrates representative technical solutions and frameworks for applying DT to RUL prediction within the SHM domain. This approach provides an effective means of addressing uncertainties in crack propagation and contributes to future advancements in SHM.

The core concept of DTHM proposed in this dissertation involves the following process: first, nonlinear crack propagation paths are simulated using FM based on FEA simulation data, producing numerical data that is labelled accordingly. This simulation data is then combined with experimentally measured data through a preprocessing stage to construct a comprehensive dataset. The resulting dataset serves as input for training and testing RUL prediction models, enabling RUL prediction and uncertainty quantification.

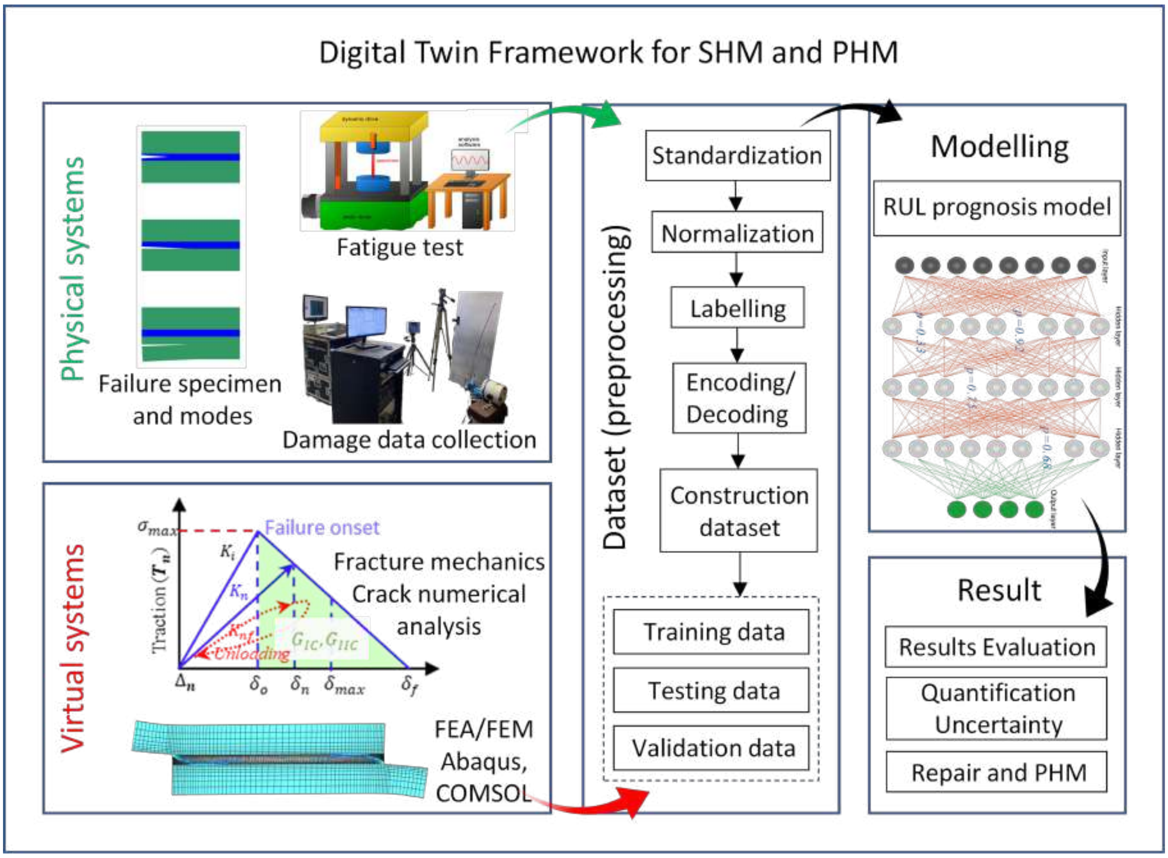

Figure 3.7 The framework of using DT techniques to predict the RUL of adhesively bonded structures.

3.5 Uncertainty quantification

In aerospace and other high-safety industries, RUL predictions must not only be accurate but must also incorporate uncertainty quantification to ensure sufficient confidence in the results. If the predicted RUL exceeds the structural health threshold, the system may progress towards irreversible failure, thereby undermining the fundamental purpose of SHM. Consequently, it is essential that RUL predictions be evaluated and that their associated uncertainties be quantified, particularly those stemming from sensor-based measurement uncertainty. In predicting the RUL of a structure, several sources of uncertainty must be taken into account: measurement uncertainty introduced by sensors, model uncertainty inherent in the RUL prediction model, and random uncertainty associated with prediction variability. Accurate quantification of these factors is critical to achieving reliable prognostics.

Many strategies have been proposed to address uncertainty. These include performing multiple measurements to reduce measurement uncertainty and deploying interconnected DL models to address predictive uncertainty. With ongoing advances in ML, an increasing number of studies now integrate uncertainty quantification directly into RUL prediction. ML techniques are especially effective in learning complex damage and predicting RUL and EoL from limited measured data. Nonetheless, predictions produced from a single deterministic model still offer limited practical value. Although adjusting model parameters or network architectures may reduce internal uncertainty, such approaches do not address uncertainties originating from noisy or variable input data. As a result, the output of a conventional NN is a single-value estimate for RUL or EoL, which is highly sensitive to variations in input conditions. Even slight changes in the test environment or input dataset can significantly affect the output, limiting its reliability for real-world decision-making. Moreover, single value estimates offer limited interpretability in practical engineering applications, as they fail to capture the probabilistic nature of structural degradation. Thus, beyond single-value predictions, RUL prognosis must include a reliability assessment, specifically, the construction of confidence intervals. Characterising prediction uncertainty is essential not only for validating the underlying model but also for reducing the randomness and instability inherent in individual predictions.

To date, relatively few studies have focused on comprehensive uncertainty quantification in RUL prediction. The primary research directions include NN-based uncertainty modelling and the formulation of prediction confidence intervals. The most widely adopted method in this area is the BNN, which addresses the limitation of conventional NN models in expressing uncertainty. Unlike standard NN, the BNN considers node parameters as random variables governed by probability density functions, thereby enabling robust representation of parameter uncertainty.

The following section introduces the BNN as a commonly used and foundational model for uncertainty quantification in RUL prediction.

3.5.1 Uncertainty classification and quantification

Uncertainty in RUL prediction can be broadly categorised into two types based on its origin: aleatory uncertainty and epistemic uncertainty. Aleatory uncertainty arises from inherent randomness in the observation process and is considered irreducible within the context of NN prediction. Common sources include noise introduced by PZT during GW excitation or sensing, as well as internal noise generated during signal processing. This type of uncertainty cannot be eliminated through larger datasets or advanced signal processing techniques; rather, it may only be reduced by changing measurement methods and improving data handling standards.

In contrast, epistemic uncertainty stems from the prediction model itself and is also referred to as model uncertainty. Unlike aleatory uncertainty, epistemic uncertainty is reducible and can be reduced by increasing the size of the training dataset or optimising model parameters. It can be further subdivided into parameter uncertainty and structural uncertainty. Parameter uncertainty involves assumptions about the distribution of model parameters (typically a Gaussian distribution) followed by estimation of posterior distributions based on observed data. Structural uncertainty relates to the choice of model architecture or assumptions made during model construction, such as symmetry or distributional constraints. In practice, uncertainty quantification often requires probabilistic analysis of both model parameters and outputs. Epistemic uncertainty can be addressed by placing prior distributions on network weights, while aleatory uncertainty is typically assessed by analysing the distribution of model outputs. A summary of these uncertainty types is presented in Tab. 3.1.

Table 3.1 Classification of uncertainty in Bayesian modeling

Uncertainty	Sub	Definition	Characteristics	Decrease
Aleatory	Homo-scedastic	Uncertainty level is the same for all inputs	Minor impact, easy to handle	No
	Hetero-scedastic	Different inputs lead to different levels of uncertainty	More common, increases prediction difficulty	Hard

Table 3.1 (continued)

Uncertainty	Sub	Definition	Characteristics	Decrease
Epistemic	Parameter	Uncertainty in the distribution of model parameters	Requires prior distribution assumption	Bayesian inference
	Structural	Uncertainty due to different model choices	Influenced by modeling methods	Improving model architecture

Common methods for uncertainty quantification include prediction variance, variance ratio, prediction entropy, and mutual information. However, not all of these techniques are widely adopted within the SHM domain. Among them, prediction variance is the most frequently used approach for quantifying uncertainty in RUL prediction. It evaluates uncertainty by computing the variance of the posterior distribution of the model's outputs. The variance ratio, in contrast, is typically applied to classification models; it is calculated based on the predicted probabilities of different categories and serves as an indicator of model confidence. In addition to these approaches, uncertainty quantification can also be achieved through Bayesian inference methods, such as Markov chain Monte Carlo sampling and deep Gaussian processes, as well as ensemble-based techniques, including variance analysis in ensemble ML frameworks. Each of these methods is suited to specific tasks, including classification, regression, and adversarial sample detection. In this dissertation, MC sampling is employed within the proposed model to perform uncertainty quantification.

3.5.2 Bayesian neural networks

The BNN is a representative model used for uncertainty quantification, introducing probabilistic reasoning into the classical NN framework. While the topological structure of a BNN is similar to that of a conventional NN, it differs by treating network weights and outputs as probability distributions rather than deterministic values. Consequently, the model parameters become random variables, enabling uncertainty to be quantified through probability distributions. BNN introduces a prior distribution $p(\omega)$ over the model parameters ω, allowing the training process to incorporate uncertainty in RUL prediction. Given a training dataset (X,Y), where $X = \{x^{(i)}\}_{i=1}^{N}$ represents the input data and $Y = \{y^{(i)}\}_{i=1}^{N}$ the corresponding outputs, the model parameters ω are inferred using Bayesian inference to obtain the posterior distribution $p(\omega \mid X, Y)$, which is then used for prediction. The posterior distribution for the RUL model can be defined by Eq. (3.19) using a likelihood function expressed as $\prod_{i=1}^{N} g(y^{(i)} \mid f^{\omega}(x^{(i)}))$, where $g(\cdot)$ denotes the Gaussian distribution, such that:

$$p(\omega \mid X, Y) = \frac{p(\omega) \prod\limits_{i=1}^{N} g(y^{(i)} \mid f^{\omega}(x^{(i)}))}{\int p(\omega) \prod\limits_{i=1}^{N} g(y^{(i)} \mid f^{\omega}(x^{(i)})) d\omega}. \tag{3.19}$$

Since the integral in Eq. (3.19) is intractable, approximation techniques such as variational inference (VI) or Markov chain are typically employed. The following section introduces the use of VI combined with dropout, which represents one of the most widely adopted approaches in current research.

BNN introduces uncertainty quantification in predictions, consisting of epistemic uncertainty and aleatoric uncertainty, which is described in Subsection 3.5.1. For classification tasks, epistemic uncertainty is modeled by parameter uncertainty, typically using a Softmax likelihood function,

$$p(\omega|X, Y) = \frac{\exp(f_c^{\omega}(x))}{\sum_{c'} \exp(f_{c'}^{\omega}(x))}. \tag{3.20}$$

The RUL prediction process can be considered as a regression problem, the output is defined to follow a Gaussian distribution,

$$p(\omega|X, Y) = \mathcal{N}(y; f^{\omega}(x), \tau^{-1} I), \tag{3.21}$$

where $f^{\omega}(x)$ is the prediction result of NN, and τ^{-1} controls the noise variance, representing aleatoric uncertainty.

Since computing the posterior is hard, it is necessary to approximate it with a variational distribution $q_{\theta}(\omega)$ and minimize the Kullback–Leibler (KL) divergence,

$$KL(q_{\theta}(\omega) \| p(\omega|X, Y)) = \int q_{\theta}(\omega) \log \frac{q_{\theta}(\omega)}{p(\omega|X, Y)} d\omega. \tag{3.22}$$

The variational inference objective function is

$$\mathcal{L}_{VI}(\theta) := \int q_{\theta}(\omega) \log p(\omega|X, Y) d\omega - KL(q_{\theta}(\omega) \| p(\omega)). \tag{3.23}$$

The goal of KL divergence is to measure the difference between the approximate distribution $q_\theta(\omega)$ and the true posterior distribution $p(\omega \mid X,Y)$. Connecting the Eq. (3.19) and Eq. (3.22), the KL divergence of $q_\theta(\omega)$ and $p(\omega \mid X,Y)$ can be organised as follows:

$$\begin{aligned} KL(q_\theta(\omega) \| p(\omega \mid X,Y)) = & \int q_\theta(\omega) \log \frac{q_\theta(\omega)}{p(\omega)} d\omega \\ & - \sum_{i=1}^{N} \int q_\theta(\omega) \log \left(l \left(y^{(i)} \mid f^{\omega} \left(x^{(i)} \right) \right) \right) d\omega \\ & + \log \left(\int p(\omega) \prod_{i=1}^{N} l \left(y^{(i)} \mid f^{\omega} \left(x^{(i)} \right) \right) d\omega \right), \end{aligned} \tag{3.24}$$

where $KL(q_\theta(\omega) \| p(\omega))$ as the first term in the right side of the Eq. (3.25), represents the KL divergence between the approximate distribution $q_\theta(\omega)$ and the prior distribution $p(\omega)$. Minimizing this term ensures that $q_\theta(\omega)$ remains close to the prior. The second term is the expected log-likelihood concerning $q_\phi(\omega)$, which measures how well the model explains the data. This term determines the fitting quality of the NN model. The last one means a constant that has no relationship with the variable. Thus, the optimization process involves minimizing $KL\left(q_\phi(\omega) \| p(\omega)\right)$ while maximizing the following term:

$$\sum_{i=1}^{N} \int q_\phi(\omega) \log \left(l \left(y^{(i)} \mid f^{\omega} \left(x^{(i)} \right) \right) \right) d\omega. \tag{3.25}$$

Since the dataset volume N is typically large, summing over all samples results in a high computational cost. Besides, the RUL prediction model $f^{\omega}(x)$ is often complex and obscure, making high-dimensional integration over ω difficult. To address this issue, Gal et al. proposed the dropout method in [115], interpreting Dropout as a variational approximation to the distribution of NN weights, thereby enabling Bayesian inference. This method treats dropout as a way of sampling from $q_\theta(\omega)$ without explicitly computing the posterior distribution. It is calculated by the MC sampling method as follows:

$$\mathbb{E}_{q_\theta(\omega)} [\log l(y \mid f^{\omega}(x))] \approx \frac{1}{T} \sum_{t=1}^{T} \log l(y \mid f^{\omega_t}(x)), \tag{3.26}$$

where ω_t represents the weights sampled using dropout, and T is the number of samples. Since dropout applied to weights can be considered as a specific form of variational distribution, it demonstrated that dropout approximates Bayesian inference over $p(\omega)$, allowing the

KL divergence to be simplified as an L2 regularization term:

$$KL\left(q_{\phi}(\omega)\|p(\omega)\right) \approx \lambda\|\theta\|^2, \tag{3.27}$$

where λ depends on the dropout rate and prior assumptions. This method avoids the need to change the entire distribution, requiring only random neuron masking during forward passes.

The optimization objective for variational inference can be further expressed as

$$\mathscr{L}(\theta,p) = -\frac{1}{N}\sum_{i=1}^{N}\log p\left(\omega \mid x_i,y_i\right) + \frac{1-p}{2N}\|\theta\|^2, \tag{3.28}$$

where the N and p denote the volume of samples and probability of dropout, respectively.

Furthermore, uncertainty estimation can be achieved through MC sampling, thereby avoiding the computational burden associated with traditional MC sampling methods. In this context, uncertainty quantification within a BNN is based on the posterior distribution $p(\omega \mid X,Y)$. By incorporating variational inference techniques alongside dropout, the inference process becomes computationally tractable, enabling uncertainty quantification during prediction. Model training still relies on standard stochastic gradient descent (SGD) optimisation, while predictive uncertainty is quantified through the computation of the mean and variance of multiple forward passes. Detailed mathematical equations for implementing the evidence lower bound (ELBO) using KL divergence, as well as for performing uncertainty quantification via dropout, are provided in the literature [115]. Fig. 3.8 illustrates the BNN-based framework for RUL prediction.

3.6 Evaluation indicators of remianing useful life

Data-driven approaches are popular for predicting RUL. These methods utilise system state monitoring data as input and apply predictive models (as discussed in Section 3.3) to estimate the duration from the onset of damage to the EoL. Within this predictive process, the validation of results and the quantification of associated uncertainties are essential for assessing the reliability of the prognosis. This section introduces commonly used evaluation metrics for RUL prediction. The application of these metrics allows for an analysis of prediction results. The appropriate use of such indicators is a critical step in translating predictive models into practical tools for PHM.

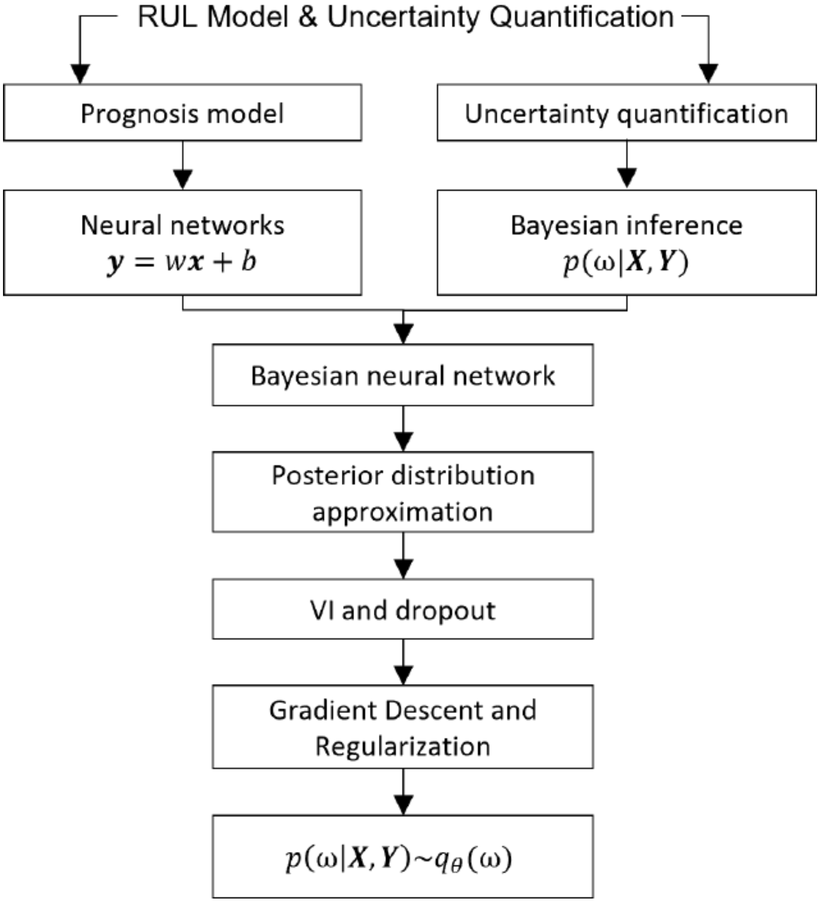

Figure 3.8 The flowchart of employing BNN to quantify uncertainty.

3.6.1 Error-based evaluation methods

For regression-based prediction models, error metrics are essential for evaluating the performance of ML algorithms. Commonly adopted metrics include MSE, root mean squared error (RMSE), and mean absolute error (MAE).

The RUL prediction task is considered as a typical regression problem, the error between the actual RUL ($\mathrm{RUL}_{\mathrm{actual}}$) and the predicted RUL ($\mathrm{RUL}_{\mathrm{pre}}$) at a given time t_i is defined as $E_{\mathrm{RUL}}(t_i)$. Here, t_i denotes any time point i during the prediction process, where $t_i \in [0, \mathrm{EoL}]$. The MSE for RUL prediction is defined as:

$$\mathrm{MSE}_{\mathrm{RUL}} = \frac{1}{n}\sum_{i=1}^{n}\left(\mathrm{RUL}_{\mathrm{actual}}(t_i) - \mathrm{RUL}_{\mathrm{pre}}(t_i)\right)^2. \tag{3.29}$$

The model is considered to perform optimally when the predicted results closely align with the actual RUL. A larger error corresponds to a higher MSE value, indicating reduced reliability of the prediction. RMSE offers a more interpretable measure by expressing the average prediction error in the same units as the original data. It reflects the typical deviation between predicted and actual values and is defined as follows:

$$\mathrm{RMSE}_{\mathrm{RUL}} = \sqrt{\frac{1}{n}\sum_{i=1}^{n}\left(\mathrm{RUL}_{\mathrm{actual}}(t_i) - \mathrm{RUL}_{\mathrm{pre}}(t_i)\right)^2}. \tag{3.30}$$

The RMSE is often used as an evaluation metric for the loss function of prediction models. It is based on the assumption that the errors follow a normal distribution. Therefore, before predicting the RUL, it is necessary to verify whether the sample data meet the condition of normal distribution. Additionally, smoothing processing is usually applied to the data in order to avoid the impact of outliers.

To overcome the limitation of absolute error being scale dependent, considering percentage error is a feasible solution. The mean absolute percentage error (MAPE) is one of the most widely used error metrics in the industry due to its simplicity and intuitive interpretation. However, MAPE-estimated prediction models tend to produce lower prediction results, so it is crucial to ensure consistency between the prediction target and the error metric during use, such that

$$\mathrm{MAE} = \frac{1}{n}\sum_{i=1}^{n}\left|\mathrm{RUL}_{\mathrm{actual}}(t_i) - \mathrm{RUL}_{\mathrm{pre}}(t_i)\right|, \tag{3.31}$$

$$\mathrm{MAPE} = \frac{100\%}{n} \sum_{i=1}^{n} \left| \frac{\mathrm{RUL}_{\mathrm{actual}}(t_i) - \mathrm{RUL}_{\mathrm{pre}}(t_i)}{\mathrm{RUL}_{\mathrm{actual}}(t_i)} \right|. \tag{3.32}$$

Tab. 3.2 presents a comparison of commonly used error evaluation metrics for assessing RUL prediction performance. In practical applications, it is essential to recognise the specific risks and limitations associated with each metric and to avoid relying solely on a single criterion when evaluating model accuracy or formulating maintenance decisions.

Table 3.2 Error Metrics and Their Application in RUL Prediction

Metrics	**Advantages**	**Disadvantages**	**Suitable for RUL Prediction**
MAE	Easy to interpret	Sensitive to outliers	Evaluation lose function and results
RMSE	Emphasizes larger errors	Highly sensitive to outliers	Loss function, evaluation lose function and results
MAPE	Intuitive and simple to calculate	Sensitive to outliers, not suitable for values near zero	Evaluation results

3.6.2 Accuracy-based evaluation methods

In addition to analysing the performance of errors in the prediction process, precision is also a factor often considered in the RUL prediction process. The precision can be defined as follows:

$$\mathrm{Precision} = \sqrt{\frac{\sum_{i=1}^{n} (E_m(t_i) - \overline{E_m}(t_i))^2}{n-1}}, \tag{3.33}$$

where n denotes the total number of time steps or data points corresponding to the EoL of the prediction model N_{EoL}. Precision is a relative metric that measures the degree to which errors E_m deviate from the mean error $\overline{E_m}$ during the prediction process.

$$E_m(t_i) = RUL_{\mathrm{actual}}(t_i) - RUL_{\mathrm{pre}}(t_i), \tag{3.34}$$

with $t_i \in [1, n]$. Prediction precision can be regarded as the MSE of the error, where a smaller value signifies more concentrated RUL predictions, reduced fluctuation in the data, and consequently, more reliable results. In contrast, a larger value may suggest that the RUL prediction model is either insensitive to input damage features or exhibits instability in its predictions.

To more accurately assess the proportion of prediction error relative to the actual service life, the metric of relative accuracy (RA) is commonly employed. RA at a specific fatigue time t_i, denoted as $RA(t_i)$, quantifies prediction accuracy at that point and is defined as follows:

$$RA(t_i) = 1 - \left| \frac{E_m(t_i)}{RUL_{\text{actual}}(t_i)} \right|, \tag{3.35}$$

where $E_m(t_i)$ is the prediction error at t_i, $RUL_{\text{actual}}(t_i)$ denotes the actual RUL at cycle t_i. RA quantifies the proportion of error in the prediction process relative to the actual RUL. When $RA(t_i)$ approaches 1 at a given time t_i, it indicates that the prediction error $E_m(t_i)$ is close to zero, suggesting that the predicted value closely matches the actual RUL. Conversely, if $RA(t_i) = 0$, the prediction significantly deviates from the true RUL, reflecting poor performance of the prognosis model.

The RA metric is useful for evaluating a model's ability to predict EoL at a specific instance, as it represents the deviation of a single prediction from the actual value. However, RA is limited when assessing accuracy across the entire RUL prediction process, as it only captures isolated measurements. To address this, cumulative relative accuracy (CRA) is introduced to evaluate the overall prediction accuracy over time. CRA represents the aggregated prediction performance across multiple time steps and is defined as follows:

$$CRA = \frac{\sum_{i=1}^{n} RA(t_i)}{n}, \tag{3.36}$$

where $RA(t_i)$ is the relative accuracy at time t_i. Thus, CRA represents the average value of $RA(t_i)$ across all fatigue cycles and serves as a comprehensive metric for evaluating the precision of an RUL prediction model over the entire lifecycle. Therefore, CRA is particularly suitable for assessing the overall predictive performance of a system over extended periods and is commonly employed to compare the effectiveness of different RUL prediction models in long-term prognostic tasks.

3.6.3 Scoring function

The scoring function represents another important approach for evaluating the prediction results. While the above error-based metrics are useful, they often do not account for the differing consequences of underestimation and overestimation. Such asymmetries are particularly relevant in practical scenarios, where incorrect predictions may affect maintenance scheduling and operational safety. To address this, customised scoring functions have been developed that apply asymmetric penalties, thereby making evaluation outcomes more meaningful and actionable for prognostics and maintenance planning.

The primary function of a scoring metric is to quantify the deviation between the predicted and actual RUL, while simultaneously providing insights into the reliability of the model. By employing an asymmetric formulation, the scoring function imposes different penalties depending on whether the predicted RUL is an overestimation ($h_i < 0$) or an underestimation ($h_i \geq 0$). The mathematical formulation of the scoring function is given as follows:

$$\text{Score} = \begin{cases} \sum_{i=1}^{n} \left(e^{\frac{h_i}{13}} - 1 \right), & h_i < 0 \\ \sum_{i=1}^{n} \left(e^{\frac{h_i}{10}} - 1 \right), & h_i \geq 0, \end{cases} \tag{3.37}$$

where h_i represents the error between the predicted RUL and the actual RUL. A lower score indicates superior prediction performance. The scoring function differentiates between underestimation ($h_i < 0$) and overestimation ($h_i \geq 0$), assigning a higher penalty to the latter. Overestimation is penalised more heavily because it may not allow sufficient time for timely maintenance, thereby increasing the risk of unexpected structural failure. In contrast, underestimation is generally considered less critical, as it introduces a conservative buffer that enables earlier intervention. This asymmetric scoring approach ensures that model evaluation reflects the practical consequences of prediction errors, thereby improving the relevance of RUL predictions and application.

3.7 Summary

This chapter highlights the critical role of uncertainty quantification in the RUL prediction process. As a key component in evaluating the credibility of prediction outcomes, uncertainty quantification is indispensable for ensuring that the results are both trustworthy and of practical engineering value. The chapter begins by introducing the various sources of uncertainty inherent in RUL prediction, including sensor measurement uncertainty, model-related uncertainty during prediction, and random uncertainty in the prediction outcomes. Next, many NNs that have been used for predicting RUL are introduced. Although conventional

NN-based models can estimate RUL, they typically generate only a single deterministic value without providing confidence intervals. This limitation reduces their applicability in real-world engineering scenarios. Reliable prognostic models should not only produce point estimates for the EoL but also quantify uncertainty, thereby offering insight into the reliability of the prediction and mitigating the effects of uncertainty.

To address these challenges, numerous uncertainty quantification methods have been proposed, with the BNN model being among the most prominent. This chapter introduces the inference mechanism of BNN and explains how it achieves uncertainty quantification. In contrast to conventional NN, BNN assigns probability distributions to model parameters, thereby capturing parameter uncertainty and enabling the generation of predictions accompanied by confidence intervals. This probabilistic framework enhances the reliability of RUL estimates by offering more informative outputs than single-point predictions. The BNN model discussed in this chapter serves as a fundamental approach to uncertainty quantification and is also used as a baseline for comparison with the DTHM model proposed in this dissertation.

Chapter 4

Diagnosis-prognosis framework

4.1 Introduction

This chapter proposes an integrated DT-based framework for damage diagnosis and RUL prognosis of bonded composite structures. The framework employs a hybrid model methodology for RUL prediction and introduces an innovative DT model that integrates the XFEM with FM. Furthermore, to address uncertainty in RUL prediction within the DTHM, this chapter proposes a CNN-LSTM with dropout method to approximately replace traditional Bayesian uncertainty quantification techniques, thereby enhancing the reliability of predictions.

4.2 Integrated framework for damage diagnosis and remaining useful life prognosis

This chapter proposes an integrated framework based on a DT-ML technique for damage diagnosis and RUL prognosis of the adhesively bonded joints under fatigue loading. The core contribution of this dissertation lies in acquiring damage information and predicting RUL by measuring the GW signal and employing the DTHM model. These aspects are detailed in Subsections 4.2.1 and 4.2.2, respectively. The integrated framework is illustrated in Fig. 4.1. The diagnosis–prognosis framework constitutes the core of this dissertation and is proposed based on the analysis conducted in the preceding four chapters. Its primary innovation lies in the integration of FCP with a hybrid modelling approach to enable damage assessment of bonded composite structures. The framework incorporates two data sources: simulation and experiment, as illustrated in Fig. 4.1(a). In this figure, red data flows represent the simulation path, while blue indicates the experimental path.

The simulation branch consists of two key components. First, FEA based on the XFEM is performed in Abaqus to simulate crack propagation within the adhesive region. This process is governed by a traction-separation (T-S) law and is illustrated in Fig. 4.1(b). The second component involves FCP computations, which simulate the nonlinear crack propagation behaviour through numerical calculations. These are informed by the damage parameters, crack evolution, and strain energy release values obtained from the XFEM simulations. Further details of this process are presented in Subsection 4.3.3.

Similarly, the experiment is shown in Fig. 4.1(c), where measured GW are employed to quantify damage extent. This constitutes a key part of the diagnosis process within the framework.

Finally, the collected data are used to train the RUL prediction model, as illustrated in Fig. 4.1(d).

4.2.1 Damage diagnosis

The damage diagnosis focuses on measurement methods, signal processing, and damage extent quantification. The main research objectives are as follows:

- Using GW to analyse damage of adhesively bonded composite structures;
- Conducting the simulation and experiment;
- Signal processing techniques for extracting damage features;
- The relationship between the measured GW and damage extent, along with the calculation of the DI;
- Quantitative and qualitative evaluation of damage identification accuracy.

4.2.2 Remaining useful life prognosis

RUL prediction is primarily based on the integration of multi-model ML techniques with FM approaches. The key challenges addressed in this study are summarised as follows:

- Developing data preprocessing techniques to determine the appropriateness of the input database;
- Developing a fatigue crack propagation simulation method based on a multi-model approach, specifically using XFEM and FCP;

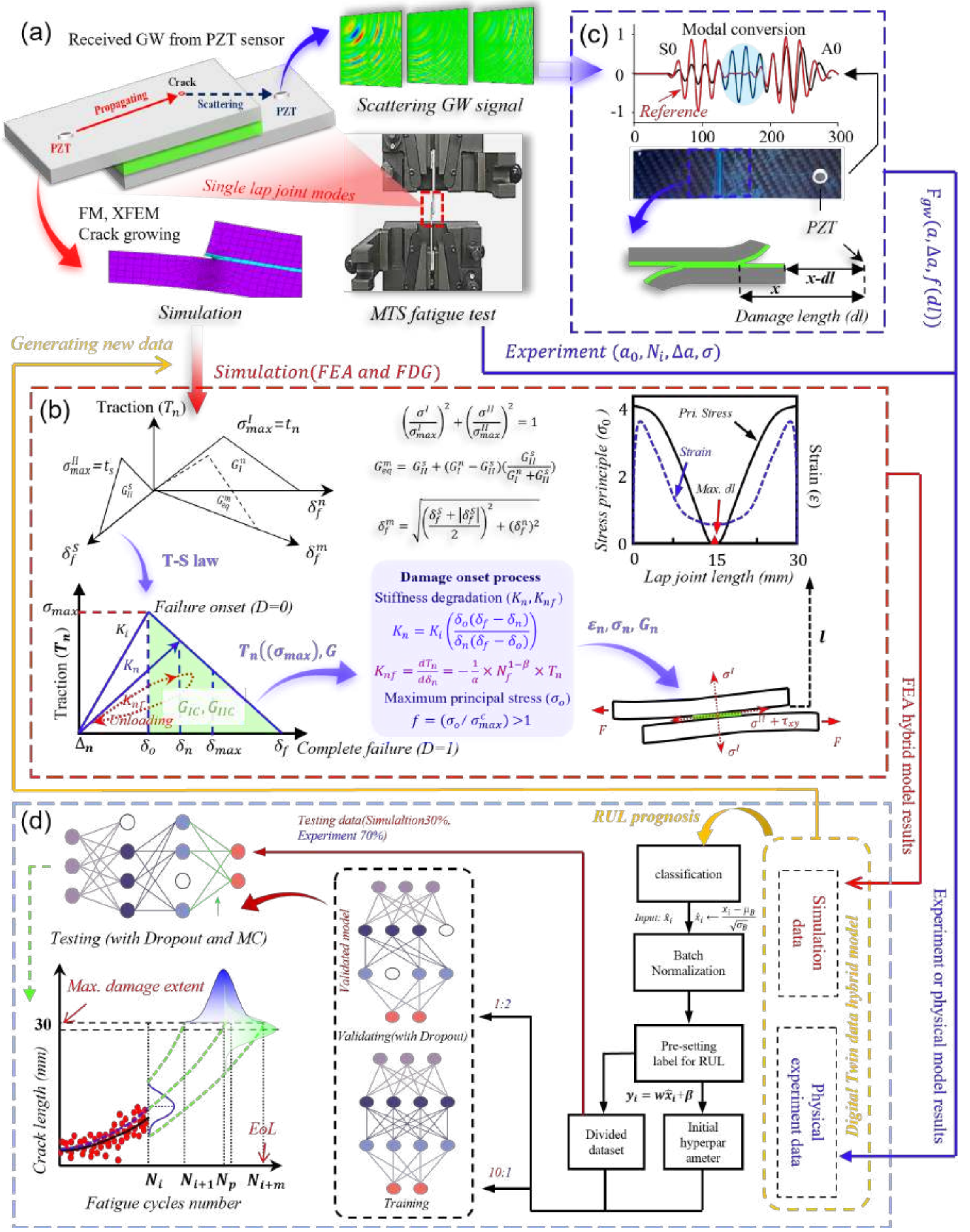

Figure 4.1 An integrated framework for damage diagnosis and RUL prediction in bonded composite structures based on DT techniques.

- Establishing the DTHM for damage extent calculation by integrating virtual and physical models, incorporating FM into the DT framework to improve prognosis accuracy;
- Employing a CNN-LSTM architecture combined with dropout and MC sampling to approximately replace traditional BNN, enabling both RUL prediction and uncertainty quantification;
- Defining evaluation indicators and combining experimental data with a 95% confidence interval to qualitatively analyze prediction results;
- Providing constructive recommendations for practical applications combined with DTHM.

4.3 Analysis of modules in the diagnosis-prognosis integrated framework

The structure of the diagnosis-prognosis framework is shown in Fig. 4.1. This section introduces the functions of each module within the framework and explains how they contribute to damage diagnosis and RUL prediction.

4.3.1 Finite element analysis simulation module

The FEA module illustrated in Fig. 4.1(b) utilises a combination of finite element tools and XFEM cohesive theory to simulate crack propagation in the bonded zone. The resulting simulation data are incorporated into a DT database to support the training of a DL model. Specifically, this module calculates the damage evolution across fatigue cycles using FEA, offering valuable input data for FCP model. Furthermore, it generates key FM parameters that can be employed in subsequent analyses.

The integration of XFEM with the cohesive constitutive model facilitates accurate simulation of crack propagation within the adhesive region. The principal advantage of this approach lies in XFEM to compute crack growth directly, enabling cracks to propagate in random directions with minimal sensitivity to mesh alignment—an improvement over conventional CZM, which is more mesh-dependent. This capability renders XFEM more representative of actual crack paths in adhesively bonded joints. This module also addresses the issue of parameter estimation by extracting two critical parameters from simulation data: the maximum traction force ($T_{\max}$) and the strain energy release rate (G) in the T-S law, thereby eliminating the need for extensive experimental testing. The mechanism underpinning the simulation model is depicted in Fig. 4.2, which shows the damage criterion employed for the bonded region. The linear elastic T–S law defines the macroscopic relationship between traction force and displacement. When the traction reaches a predefined critical value, corresponding to damage initiation, stiffness degradation begins—illustrated in Fig. 4.2 as the transition from k_i to k_n, and subsequently to k_{nf}, where k_{nf} represents the stiffness degradation path under fatigue loading. The criterion adopted to define damage onset is based on the maximum principal stress.

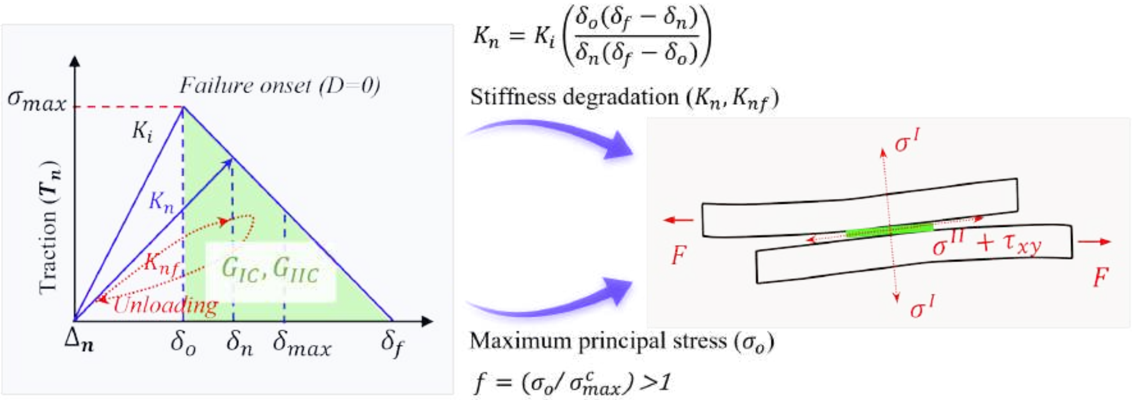

Figure 4.2 Damage onset and propagation process based on the T-S law.

The principle of XFEM for crack propagation is to add the enrichment function of crack surface and crack tip displacement based on FEM, which is described in Eq. (4.1),

$$u = \sum_{i=1}^{n} N_i \left(u_i + H a_i + \sum_{j=1}^{4} Q_j b_{ij} \right), \tag{4.1}$$

where u denotes the displacement approximation function, N_i is the FEA shape function, u_i, a_i and b_{ij} are the classical and additional degree of freedom, Q_j represents displacement function at the area of crack tip, i and j denote the number of nodes for the whole region and crack tip, H represents the Heaviside function that crosses the level of the crack. The crack calculation method of XFEM is shown in Fig. 4.3. This figure demonstrates two enrichment functions used in XFEM. The background mesh represents the standard finite element mesh, while the blue line represents the crack path. The Heaviside function is applied primarily to the nodes on the crack surface to capture displacement discontinuities. The crack tip enrichment function is applied to the nodes around the crack tip to accurately represent the singular stress field.

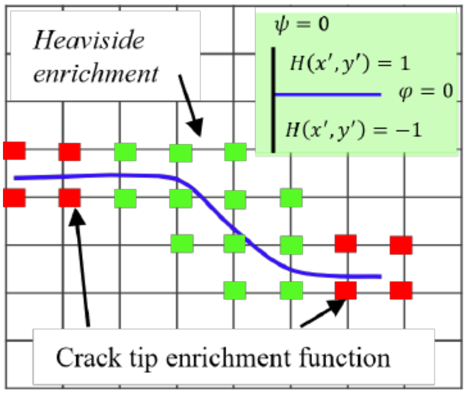

Figure 4.3 The diagram of the XFEM method using the finite element crack surface enrichment function and crack tip displacement to calculate crack propagation.

The XFEM method is combined with a cohesive constitutive model based on the T–S law to simulate the crack propagation within the cohesive zone, as illustrated in Fig. 4.2. To address the problem of crack extension under mixed-mode loading conditions, this dissertation adopts the maximum principal stress criterion to determine the onset of cracking. This criterion is expressed in Eq. (4.2), as follows:

$$f = \frac{\sigma_{Io}}{\sigma^{I}_{\max}} + \frac{\sigma_{IIo}}{\sigma^{II}_{\max}} = 1, \tag{4.2}$$

where σ_{Io} denotes maximum principal normal stress at tensile condition, $\sigma^{I}_{\max}$ is maximum permission normal stress of adhesion. When the principal stress satisfies the damage initiation criterion, the cohesive zone will start the stage of damage degradation. Simultaneously, the critical stress intensity factor and crack extension variable under mixed mode are described using the Benzeggagh-Kenane fracture criterion [116], which can be calculated using Eq. (4.3), such that:

$$MMR = \left(\frac{G_{\text{shear}}}{G_{\text{total}}}\right)^{\eta} = \left(\frac{G_{II}}{G_I + G_{II}}\right)^{\eta}. \tag{4.3}$$

Thus, the critical energy release rate under mixed mode can be defined as:

$$G_{MC} = G_{IIC} + (G_{IC} - G_{IIC})MMR. \tag{4.4}$$

A bilinear T-S constitutive model of the interface is utilised to describe the process of stiffness degradation. This dissertation combines the S-S curve and T-S law of the bonded zone to illustrate the change in stress at the onset of damage [117]. Similarly, the relative displacement of the interface under mixed mode can be defined as:

$$\delta_n^m = \sqrt{(\delta_n^I)^2 + (\delta_n^{II})^2}, \tag{4.5}$$

$$\delta_0^m = \delta_0^{II} \sqrt{\frac{1 + \left(\frac{\delta_n^{II}}{\delta_n^I}\right)^2}{(\delta_0^{II})^2 + \left(\frac{\delta_0^I \delta_n^{II}}{\delta_n^I}\right)^2}}, \tag{4.6}$$

$$\delta_f^m = f(K_n, \delta_0^m, G_{IIC}, G_{IC}). \tag{4.7}$$

where δ_n^I and δ_n^{II} represent the normal (Mode I) and tangential (Mode II) components of the separation displacement at the interface, respectively. Their combination yields the mixed-mode equivalent separation displacement δ_n^m. δ_0^I and δ_0^{II} denote the critical separation displacements for damage initiation under pure Mode I and Mode II loading, respectively, while δ_0^m is the corresponding equivalent value under mixed-mode conditions. δ_f^m denotes the final mixed-mode separation displacement associated with complete failure, and is computed as a function of the interfacial stiffness K_n, the mixed-mode initial separation δ_0^m, and the fracture energies G_{IC} and G_{IIC}, which correspond to the energy release rates for Mode I and Mode II, respectively. As shown in Eq. (4.7), the complete damage displacement at the interface in the bonding zone is determined by two key parameters: the maximum traction and the cohesive energy. Accurate determination of these parameters is essential for applying the T–S law in engineering contexts. At present, extensive experimental testing remains the most common method for parameter acquisition; however, this approach is both time-consuming and costly. Since the objective of this dissertation is to predict the RUL, it does not aim to explore the variations arising from different parameter estimation methods. Therefore, based on the methods proposed in [118, 119], a mechanical parameter estimation model is developed, as illustrated in Fig. 4.4. By identifying the fatigue point N_f corresponding to adhesive cracking, the associated strain value is first obtained from the stain-fatigue curve. This strain is then used to locate the corresponding point on the J-integral versus strain curve, derived from FEA, in order to determine the Mode II fracture energy (about 0.31).

This method enables the determination of cohesive energy and strain parameters within the T-S law. Subsequently, the corresponding strain is applied to the actual S–S curve to calculate the maximum traction. The S–S curve used in this chapter is derived using Eqs. (4.8) and (4.9), following the approach outlined in [119], as follows:

$$\sigma = \sigma_{\text{nominal}}(1 + \varepsilon_{\text{nominal}}), \tag{4.8}$$

$$\varepsilon = \ln(1 + \varepsilon_{\text{nominal}}). \tag{4.9}$$

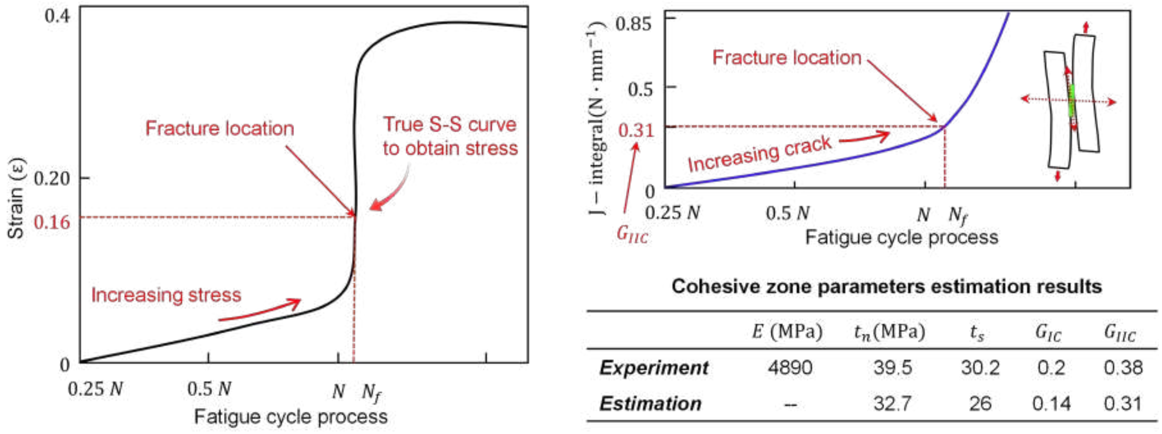

Cohesive zone parameters estimation results

	E (MPa)	t_n(MPa)	t_s	G_{IC}	G_{IIC}
Experiment	4890	39.5	30.2	0.2	0.38
Estimation	–	32.7	26	0.14	0.31

Figure 4.4 The parameter estimation principles for maximum traction and cohesive energy are adopted in this study, with the material properties of the AV138 adhesive [120].

Properties parameters for a commonly used adhesive material are determined using the estimation method illustrated in Fig. 4.4. The results demonstrate that the application of theoretical parameter estimation techniques has minimal impact on the uncertainty associated with RUL prediction. Nonetheless, this approach significantly reduces the need for labour-intensive and repetitive experimental procedures, offering considerable savings in both time and cost. Consequently, based on the estimation parameters listed in Fig. 4.4 and the FEA based on XFEM, a user-defined subroutine for high-cycle fatigue is presented in Fig. 4.5. In XFEM simulation, high cycle fatigue simulation requires user-defined subroutines. Under this program, fatigue crack initiation and propagation under cyclic loading can be accurately simulated. This dissertation is implemented in ABAQUS by developing user materials UMAT to define custom fatigue damage evolution criteria, update stress changes by calculating degraded stiffness, and then determine the failure process. The subroutine calculates fatigue damage accumulation based on the local stress history at each integration point.

4.3.2 Experiment module

The experimental section primarily comprises two parts: fatigue testing and damage diagnosis using GW. Overview diagram of the experiment in this dissertation is shown in Fig. 4.6.

The core emphasis was placed on GW-based damage diagnosis, which was conducted using both SLDV and PZT. In GW-based simulations, PZT sensors were employed to excite and record GW signals. The acquired data served as the basis for damage quantification and were also used as labels for training NN. In contrast, SLDV was not used for quantitative analysis but rather to visualise the full-field wave propagation. This enabled a detailed obser-

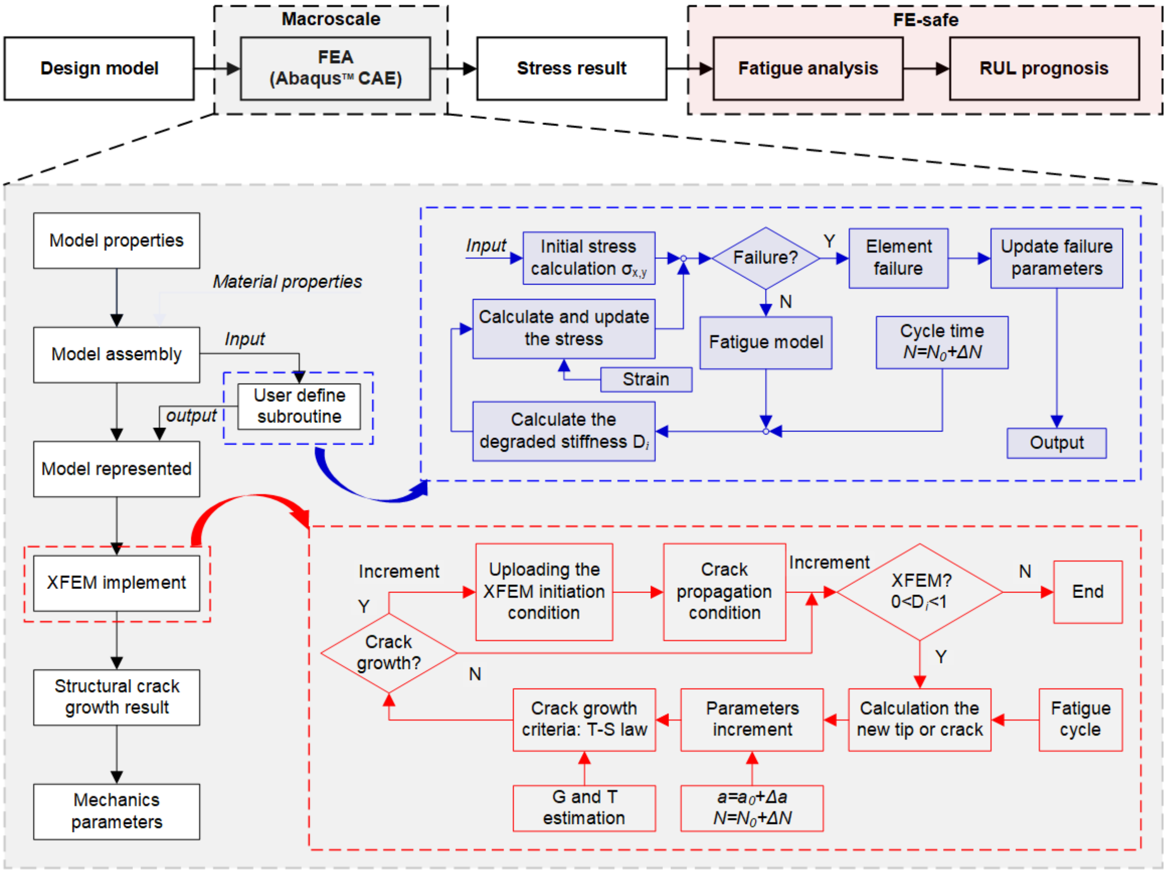

Figure 4.5 Flowchart for fatigue crack growth simulation and framework for high-cycle fatigue subroutines.

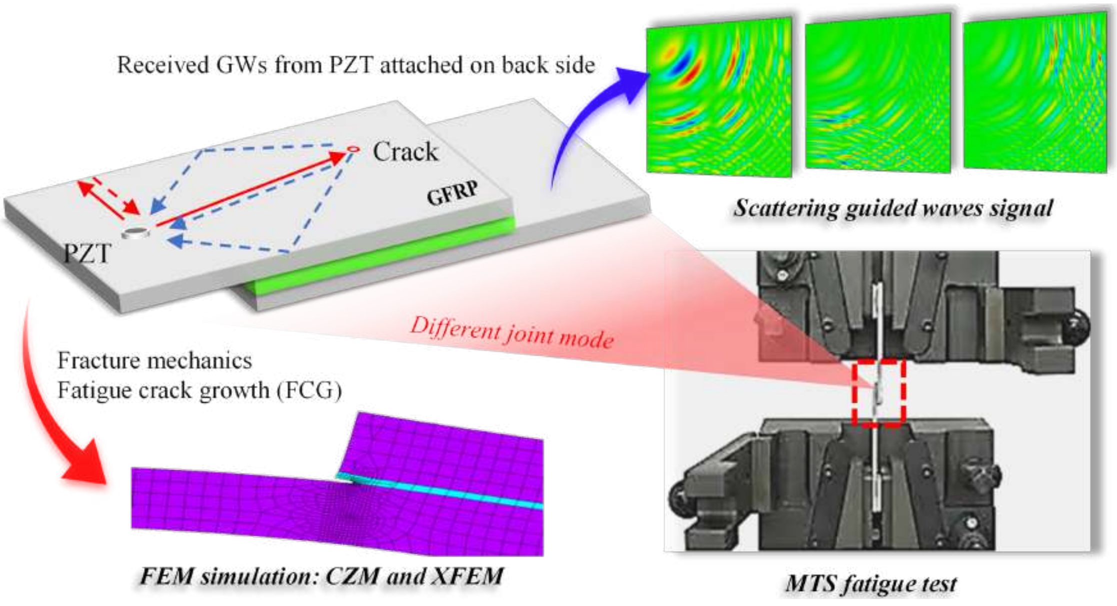

Figure 4.6 Schematic of the SLJ structure experimental process.

vation of GW interactions across the bonded zone, such as signal reflection and scattering at damage sites. The insights gained from SLDV supported the validation of the numerical model and enhanced the interpretability of the diagnostic framework.

The fatigue testing data used in this dissertation is referenced from the validated experimental framework proposed by [73, 121]. Due to limitations in the available experimental data, the dataset was extended by introducing additional Gaussian white noise to simulate variability.

The original fatigue experiments were conducted on SLJ specimens with a 30 mm bonded overlap length, 0.2 mm adhesive thickness, and 3 mm adherend thickness. Fatigue loading was applied under constant amplitude fatigue conditions using a sinusoidal waveform, with a stress ratio of $R = 0.1$ and a maximum load corresponding to 50% of the static failure strength of SLJ. The loading frequency was set to 10 Hz, optimised to balance experimental efficiency and mitigate thermal effects. Damage monitoring was carried out at fixed intervals of every 200 cycles, allowing high-resolution tracking of crack initiation and growth while minimising test interruptions. At each inspection point, the following were recorded: the cycle count N, and the estimated damage length α. Fatigue testing was terminated either when the damage length reached the full overlap or upon complete interfacial failure.

Another important experiment in this experiment focused on the use of GW to quantify damage extent, which is also a common method for obtaining damage extent in fatigue tests. In the physical experiment, structural information must be acquired via sensors attached to the specimen in order to collect real damage data and the corresponding EoL values of the adhesively bonded composite material, as illustrated in Figs. 4.1(a) and (c).

The recorded GW signals are preprocessed to extract relevant damage-related features. These features are then correlated with damage evolution in the bonded zone to establish a relationship between damage extent and the measured GW. To this end, a multi-indicator quantification approach is adopted. The measured signals are first segmented using a windowing technique based on varying ToF. Subsequently, the correlation between the processed signals and the reference signal is computed to derive DI. The aim is to establish a damage detection method tailored specifically to adhesively bonded composite structures, rather than relying on general-purpose SHM techniques. The experimental procedure for damage extent quantification is illustrated in Fig. 4.7.

Fig. 4.7 shows the experimental setup for GW-based damage diagnostics in bonded CFRP structures. The SLDV controller and signal generator form the central control unit, which drives the PZT actuators via amplifiers. The generated signals are transmitted to the PZTs attached on the surface of the CFRP adherend. The SLDV scanning head located in front of the sample performs a non-contact full-field laser scan, which allows visualization of

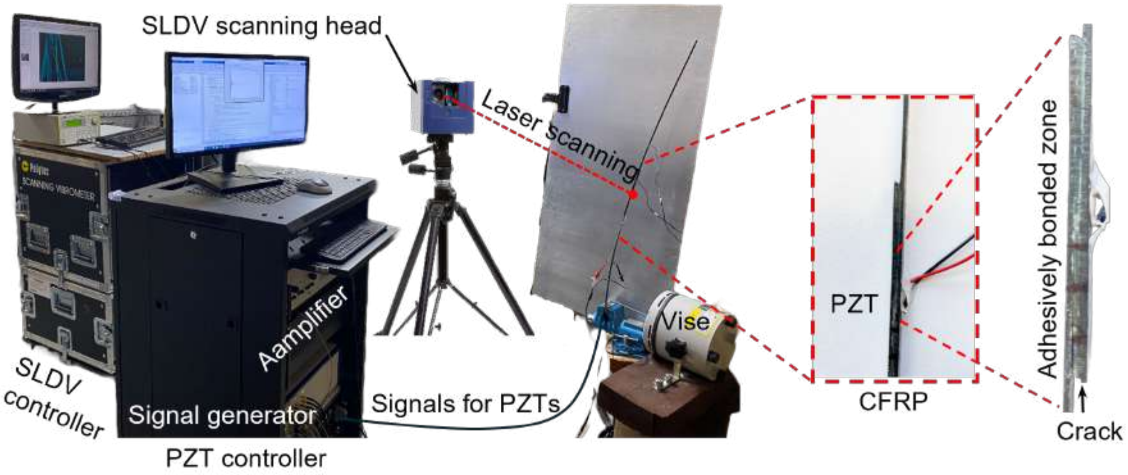

Figure 4.7 The experimental setup for damage detection and quantification of adhesively bonded structures.

the GW propagation in the bonding area. This helps to identify reflections and scattering caused by damage. The vise holds the test sample during the measurement. The image on the right shows a sample with a crack. This configuration allows simultaneous acquisition of point-by-point PZT measurements and full-field visualization via SLDV, supporting both quantitative analysis and qualitative verification of crack-induced GW scattering phenomena.

4.3.3 Crack growth model based on fracture mechanics and finite element analysis

RUL prediction constitutes the core of the DTHM framework. It integrates multiple NN and ML techniques and is composed of two primary modules: the data preprocessing module (Subsection 4.3.3) and the prediction module (Subsection 4.3.4).

The data preprocessing module handles input preparation for RUL prediction using both virtual (simulation) and physical (experimental) sources. Its primary objective is to combine ML algorithms with FCP theory in FM to enable nonlinear numerical simulation of crack growth. As illustrated in Fig. 4.8, the module consists of three components: a NN model, an FCP solver, and a data filtering and storage unit.

The initial database is established using data from both virtual and physical models. This includes stress–strain responses, FM parameters such as G_{IIC} and α_0, along with experimental measurements of damage and fatigue cycles. As shown in Fig. 4.8, the ML network is employed to fit the parameters c and m in Paris' law using a combination of simulation data and a subset of experimental results. Additionally, it predicts strain evolution

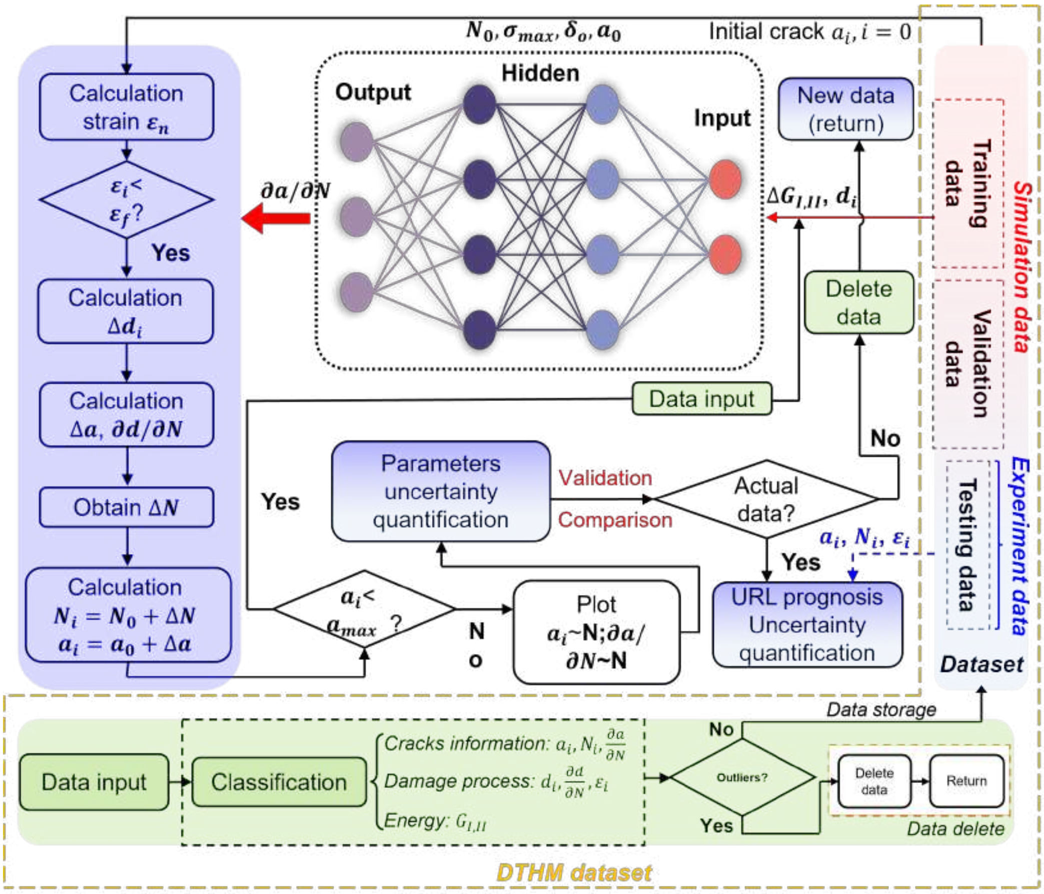

Figure 4.8 The diagram of the numerical damage analysis and crack growth model that combines simulation data with physical data, including fatigue crack growth calculations, data filtering algorithm, and data preprocessing.

along the adhesive interface to determine whether the maximum allowable strain threshold has been exceeded. The processed outputs are then input into the FM-based hybrid model to compute crack length and corresponding fatigue cycles.

The following introduces the details of crack growth calculation approaches. Considering the cohesive T-S law model shown in Fig. 4.2, the normal stress σ_n (or T_n) and stiffness degradation d_n during the fatigue cycle process can be expressed as:

$$T_n = k_n \delta_n (1 - d_n), \tag{4.10}$$

$$d_n = \frac{\delta_f(\delta_n - \delta_o)}{\delta_n(\delta_f - \delta_o)}, \tag{4.11}$$

where k_n denotes the initial contact stiffness, δ_n is the crack opening displacement, and d_n is the fatigue damage factor, which represents the stiffness degradation during fatigue cycling. From δ_o to $\delta_{\max}$, the process represents the transition from initial crack opening to maximum crack propagation. The integral region corresponds to the maximum strain energy release rate (SERR) $G_{\max}$, which can be expressed as:

$$\begin{aligned} G_{\max} &= \frac{\sigma_{\max}\delta_f}{2} - \left(\frac{\delta_f - \delta_{\max}}{\delta_f - \delta_o}\right)^2 \frac{\sigma_{\max}(\delta_f - \delta_o)}{2} \\ &= \frac{\sigma_{\max}}{2}\left(\delta_f - \frac{(\delta_f - \delta_{\max})^2}{\delta_f - \delta_o}\right). \end{aligned} \tag{4.12}$$

The energy difference during the crack growth process is derived from the relationship between the maximum SERR and the load ratio R, as follows:

$$\Delta G = G_{\max} - G_{\min} = \frac{\sigma_{\max}}{2}\left(\delta_f - \frac{(\delta_f - \delta_{\max})^2}{\delta_f - \delta_o}\right)(1 - R^2), \tag{4.13}$$

where R satisfies $R^2 = G_{\min}/G_{\max}$. Then, the crack propagation rate in the adhesive zone can be initially estimated using the Paris law, represented as:

$$\frac{\partial a}{\partial N} = C_i \times \left(\frac{\Delta G}{G_c}\right)^{m_i}, \tag{4.14}$$

where G_c is the total mixed-mode fracture toughness under a specific mode ratio, which equals $(\sigma_{\max} \times \delta_f)/2$ for the bilinear T-S law. Based on Eqs. (4.12) and (4.13), the SERR and its variation can be obtained through the T-S law. Meanwhile, the relationship between crack growth rate and crack length can be trained using the RNN model based on Eqs. (4.14) and (4.15).

The training samples for the NN comprise both experimental and simulation data. Additionally, fatigue damage evolution rate at the ith cycle, which characterises the progression of crack growth and the extent of damage in the adhesively bonded zone, is calculated as follows:

$$D_i = \frac{\partial d}{\partial N} \times \frac{\partial a}{\partial N} = \frac{(d_{i+1} - d_i)}{\Delta a} \times C_i \times \left(\frac{\Delta G}{G_c}\right)^{m_i}, \tag{4.15}$$

where d_i and d_{i+1} represent the damage variable at successive crack lengths, while Δa is the corresponding crack extension increment. C_i and m_i are material-specific fatigue parameters, which obtained from NN fitting. ΔG is the range of energy release rate during a loading cycle, and G_c is the energy release rate. In summary, the crack propagation solver is developed by combining DT technology and FM theories and is presented in Algorithm 1.

According to Algorithm 1, preliminary data are stored before entering an iterative loop, provided that the crack length has not yet reached the defined maximum. After completing k iterations, the loop terminates, and the resulting quantified uncertainty data are compared against experimental values stored in the database. If all values fall within the 95% confidence interval of the experimental results and exhibit a proportional relationship between crack growth and fatigue cycles, the data are considered valid for use in RUL prediction. Otherwise, the dataset is discarded, and the simulation–experiment loop continues to generate new data.

4.3.4 Digital twin hybrid model for remaining useful life prognosis

This subsection introduces the RUL prognosis model, composed of multiple NNs. Along with the damage extent quantification and FCP solver described in Subsection 4.3.2 and 4.3.3, it forms the predictive component of the diagnostic–prognostic framework proposed in this dissertation.

The model adopts an approximate Bayesian approach for uncertainty quantification and employs an LSTM network to handle time-series data. A CNN–LSTM architecture integrated with dropout and MC sampling is implemented. This method leverages the strengths of DL while addressing the limitations of conventional CNN-based approaches in data-driven RUL prediction, and avoids the complexity of full BNN modelling. Although dropout is commonly used to mitigate overfitting in ML, it is also effective for uncertainty estimation. It helps reduce the model complexity and training cost typically associated with Bayesian methods, and avoids frequent updates to hidden-layer node parameters.

Algorithm 1

The algorithm design of fatigue crack propagation solver and data preprocessing.

```
Input: Initial crack parameters, $a = a_0$, sample number $k$
// Training NN by simulation and experimental data
 1:         XFEM and cohesive FEA crack extent $\rightarrow a$
 2: for $j = 0$ to $n$ do
 3:         extract data $d_j$ and $\delta_f, \delta_o$ from dataset
 4:         calculating $\Delta G$ by Eqs. (4.12) and (4.13)
 5:         Obtaining data $\left(\frac{\partial a}{\partial N}\right)_j$ then
 6:         Output $C_j$ and $m_j$ through Eq. (4.14) & NNs
 7: end for
 8: while $a_i < a_{\max}$ do
 9:     for $i = 0$ to $k$ do
10:             initial input $a = a_0$, $d_i$, $\Delta G_i$
11:             input data to NN
12:             calculating $\Delta d_i$
13:             small crack increment $\Delta a_i$ from FEA
14:             calculating $D_i$ using Eq. (4.15)
15:             $a_{i+1} = a_i + \Delta a_i$
16:             $N_{i+1} = N_i + \Delta N_i$
17:             $i = i + 1$
18:     end for
19: end while
Output: $\left\{a_i, N_i, \left(\frac{\partial a}{\partial N}\right)_i, D_i\right\}$

Input-output data // data filtering
 1:         $S_i \leftarrow \left\{a_i, N_i, \left(\frac{\partial a}{\partial N}\right)_i, D_i\right\}$
 2: if $S_i \cap$ (interval confidence) $\neq \emptyset$ then
 3:         write data to the dataset
 4:         return step 19
 5: else
 6:         delete data
 7:         return initialisation
 8: end if
```

The preprocessed input data serve as training data for RUL prediction, satisfying Eq. (4.16), which defines the mapping between input features and predicted RUL,

$$Y(x)_{RUL} = w^T X_{GW} + b. \tag{4.16}$$

Performing MC sampling on the result and calculating the covariance, such that:

$$\mathrm{Cov}(x,y)_{MC} = \frac{1}{n} \sum_{n=1}^{n} \sigma(w^T x + b)\sigma(w^T y + b), \tag{4.17}$$

where given the input x and w and b parameters for the NN, the covariance can be calculated by Eq. (4.17). Similarly, when the parameters w and b satisfy the $p(w)$ and $p(b)$ distributions respectively, the predicted probability distribution can be calculated through the following equation:

$$p(Y \mid X) = \int p(w,x,b)p(w)p(b)\, dw\, db, \tag{4.18}$$

where the w denotes the matrix of w_n. The above reasoning explains how a RUL prediction model implements parameter adjustment and probability prediction. Then, similar to Bayesian uncertainty quantification, variational inference of the posterior distribution is also required in this context. KL divergence is employed to perform approximate variational inference. The derivation process for calculating the ELBO is detailed in the literature [115, 122]. The uncertainty in RUL prediction can be quantified as the divergence between the predicted and actual results, which can be expressed by the following equations:

$$\begin{aligned} \log p(Y|X) &= \mathrm{ELBO}\ q(Y|X) + \mathrm{KL}[q(Y)||p(Y|X)] \\ &= \int q(w,b) \log p(w,x,b)\, dw\, db. \end{aligned} \tag{4.19}$$

Furthermore, the ELBO term can be formulated as:

$$\mathrm{ELBO}\ q(Y|X)_{MC} = \sum_{n=1}^{N} \log \int q(w)p(y_n|x_n,w)dw - \mathrm{KL}(q(w)\|p(w)), \tag{4.20}$$

where the $\log p(Y|X)$ represents statistical constant about the dataset, namely evidence. As described above, the purpose of the calculation is to optimize KL term, that is, to minimize the value of KL. Therefore, the essence is to maximize the ELBO term, such that:

$$\begin{aligned} q^*(Y) &= \arg\min \mathrm{KL}[q(Y)||p(Y|X)] \log p(Y|X) \\ &= \arg\min \left[-\int q(Y) \log \frac{p(Y|X)}{q(Y)} dx \right]. \end{aligned} \tag{4.21}$$

By integrating the preceding equations, the sampled ELBO can be approximated through n iterations of MC sampling. The model parameters w and b are represented as multidimensional vectors formed by a linear combination of Gaussian and Bernoulli distributions. Based on the findings in [115], the modified objective function corresponds to minimising the KL divergence between the approximate distribution $q(\omega)$ and the true posterior $p(\omega \mid X,Y)$ in a deep Gaussian process framework. Consequently, the resulting objective functions are denoted as L_{dropout} and the modified form L_{Modified}, respectively.

$$L_{\text{dropout}} = \frac{1}{N} \sum_{i=1}^{N} E(y_i, \hat{y}_i) + \lambda \sum_{i=1}^{L} (||W_i||_2^2 + ||b_i||_2^2), \tag{4.22}$$

and

$$\begin{aligned} L_{\text{Modified}} \propto & \frac{1}{N} \sum_{n=1}^{N} \left(-\frac{\log p(y_n|x_n, \hat{\omega}_n)}{\tau} \right) \\ & + \sum_{i=1}^{L} \left(\frac{p_i l^2}{2\tau N} ||M_i||_2^2 + \frac{l^2}{2\tau N} ||m_i||_2^2 \right), \end{aligned} \tag{4.23}$$

where L_{dropout} denotes the objective function for the NN with dropout. It comprises a loss function and a regularization term (L2). N denotes the number of the layer nodes. $E(y_i, \hat{y}_i)$ represents the loss function that measures the difference between the actual output y_i and predicted output $\hat{y}_i$. λ is the weight decay of L2 regularization. τ denotes the precision parameter for the model, which helps in balancing the loss function and regularization term. l is the length-scale parameter, which is used to balance the regularization terms in the objective function. The matrix M_i and vector m_i represent the variational parameters for layer number i in the NN.

Fig. 4.9 illustrates the initial parameter settings for DL in the RUL prediction model, along with the mechanism by which dropout approximately replaces Bayesian estimation. A preprocessing algorithm is first applied to convert the measured GW signals into input parameters suitable for the model. These inputs include the crack length in the bonding zone and the corresponding fatigue cycle count. Some inputs are obtained from simulation, while others are from experiment. The majority of experimental fatigue lifecycle data for SLJ structure is based on research [121, 123]. In the dropout-based approximation, the network weights are resampled at each forward pass due to the stochastic nature of dropout, resulting in a different set of active weights each time. The training and testing are conducted with 800 epochs, with a learning rate adjustment step set at 50 starting from epoch 150. In addition to maximising the log-likelihood, the model incorporates a prior distribution over the weights, typically assumed to follow a Gaussian distribution. This prior is implemented as the L_2 norm of the weights, serving as a regularisation term during training. It plays a critical role in the initial prediction of damage extent in the bonded region. The total loss function, comprising the negative log-likelihood and the weight regularisation term, is optimised via gradient descent, as described in Eq. (4.23).

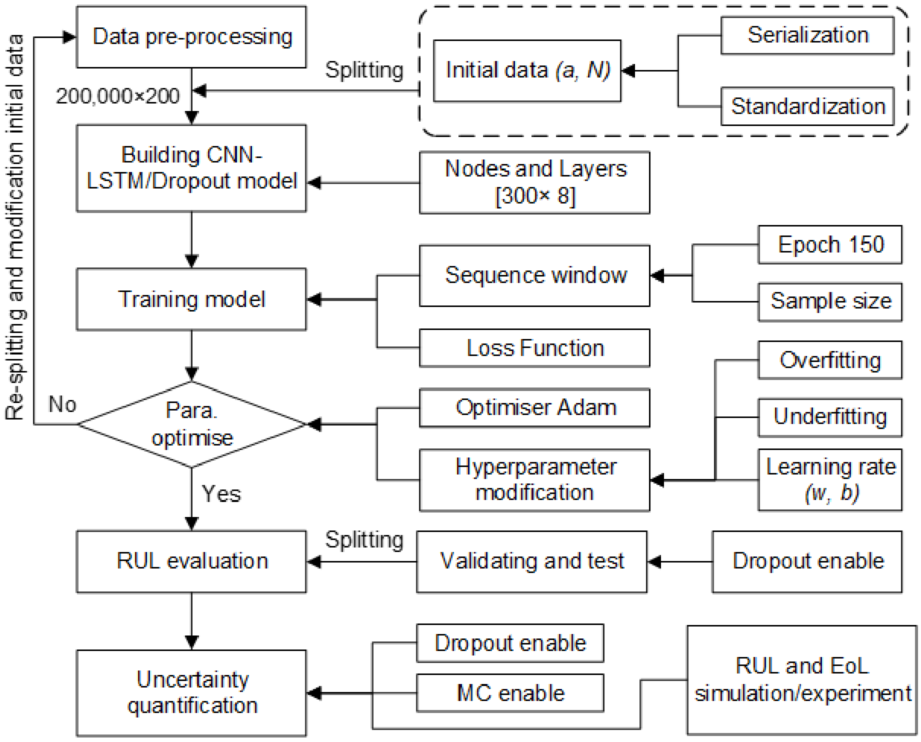

Figure 4.9 Flowchart illustrating the initial parameter configuration for RUL prognosis and the application of dropout to quantify uncertainty.

Conventional DL-based RUL prognosis methods typically produce only point estimates without providing confidence intervals, which can result in significant economic losses in practical applications due to prediction errors. To overcome this limitation, Subsection 3.5.2 introduces BNN, which incorporate probabilistic modelling of parameters. By leveraging training samples and variational inference, BNN continuously updates the posterior distributions of model parameters, thereby enhancing noise robustness and generalisation performance. Furthermore, the probabilistic output of BNN enables the quantification of predictive uncertainty. However, representing weights as probability distributions introduces additional hyperparameters, complicates the inference process, and significantly increases the computational cost of both training and prediction. To balance prediction reliability with computational efficiency, this dissertation adopts dropout as an approximate Bayesian inference technique. Compared with full BNN, the dropout-based approach achieves uncertainty quantification with minimal structural modifications and lower computational overhead.

Fig. 4.10 presents the detailed structure of the RUL prognosis model referenced in Fig. 4.1. The input data is processed following the flowchart shown in Fig. 4.1(d). After data extraction from the DTHM, normalisation is applied as a preprocessing step. The dataset is then divided into training, validation, and testing subsets, according to the proportions indicated in Fig. 4.1(d). This partitioning helps reduce overfitting and enhances the generalisability of the DL model. It is noteworthy that the volume of experimental data is significantly lower than that of simulation data (200,000 × 200).

The preprocessing of input data for training the network is a critical step, as illustrated in Fig. 4.1(d), where the inputs (x) consist of crack length (α) and fatigue cycle count (N). When dealing with compound labels (namely, damage extent and fatigue cycles), the partitioning of training data for RUL prediction must be carefully designed.

In the early stages of model development, determining optimal hyperparameter configurations is particularly challenging. The model developed in this dissertation includes three key parameters: weight (w), bias (b), and learning rate, all of which are influenced by epoch count, batch size, and dropout probability. Consequently, actual data were not used during the initial training phase to avoid wasting limited experimental data and compromising model performance. Although introducing dropout effectively mitigated overfitting, it led to underfitting. To enhance model generalisation, experimental data were incrementally incorporated into the training set. This strategy underpins the 10:1 simulation-to-experiment data ratio adopted in the training phase, as depicted in Fig. 4.1(d). Similarly, distinct partitioning strategies are applied to the validation and testing sets to ensure the model generalises well to previously unseen damage levels and fatigue cycles.

By learning damage patterns ranging from mild to severe and across varying fatigue stages, the model improves its adaptability to broader scenarios. In the course of ongoing parameter tuning, the selective inclusion of experimental data has proven effective in enhancing the reliability of the test outcomes. During the testing stage, prognosis results are evaluated with dropout enabled in both validation and test phases. This configuration ensures variability in DL architecture across iterations, yielding multiple RUL estimates. The mean (μ) and variance (Y) of these predictions are then calculated to derive an approximate confidence interval, thereby quantifying uncertainty.

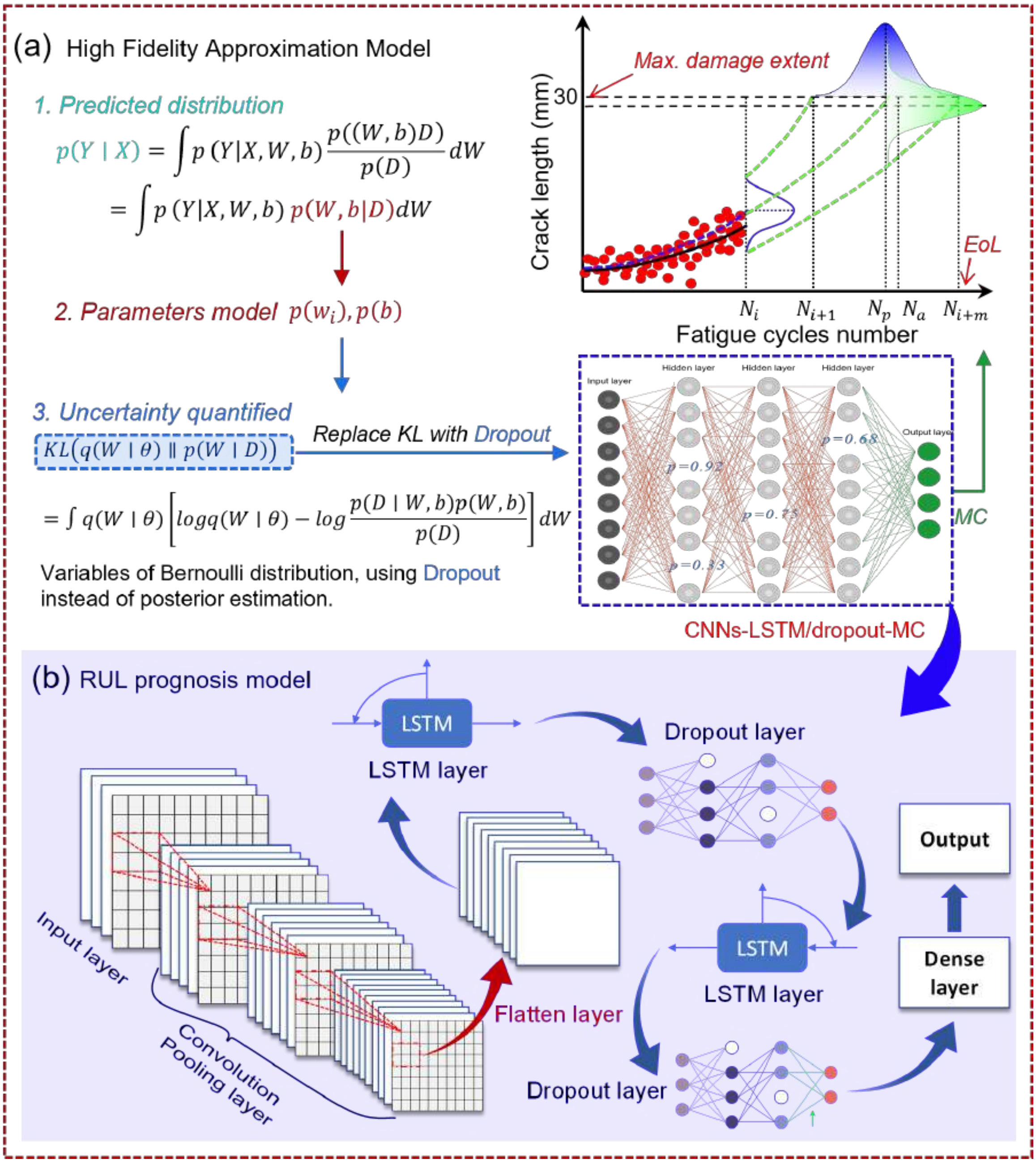

Figure 4.10 The architecture and mechanisms of the CNN–LSTM architecture with dropout and multi-connection NN.

4.4 Summary

This chapter introduces in detail the damage diagnosis and RUL prediction framework based on GW and DT. The DT integrates multiple damage analysis modules, including FCP solvers, FEA simulations, and experimental data, to simulate failure processes and predict RUL in the bonded zone of adhesively bonded composite structures. Compared with the traditional BNN, the proposed CNN-LSTM with dropout method simplifies the network structure without assigning probability distributions to each layer's nodes, thus improving prediction accuracy. Moreover, the RUL predicted using data from the FCP solver and fatigue tests demonstrates higher accuracy than relying solely on FEA. The next chapter presents the results based on this model, including experimental validation, simulation outputs, and RUL prognosis.

Chapter 5

Results and discussion

5.1 Introduction

This chapter analyses and discusses the results obtained from the diagnostic–prognostic framework presented in Chapter 4. The content is structured into three parts. First, the GW-based approach is applied to evaluate damage extent in the bonding zone of the SLJ structure, which consists of a CFRP adherend and a two-component epoxy adhesive. Second, the FCP model is used to generate the damage–fatigue cycle curve and simulate the crack growth rate. Third, the DTHM model introduced in Section 4.2 is implemented to predict the RUL and perform uncertainty quantification. Finally, the predicted RUL outcomes are validated against experimental results and benchmarked against existing models in the literature, thereby demonstrating the advantages of the proposed method.

5.2 Damage diagnosis based on guided waves

This section presents the results and analysis of damage diagnosis using GWs. In practical applications, obtaining damage information for bonded composites requires structural data collected through sensors attached on the structure. Accordingly, PZT sensors attached to the adherend are used in this study to acquire structural health information from the adhesive zone. The primary objective of GW-based quantification is to establish a correlation between the measured GW and the damage extent.

5.2.1 Simulation results of damage detection

A set of simulation experiments was first conducted in COMSOL. This section introduces a damage detection strategy for a typical CFRP plate structure to preliminarily evaluate the sensitivity of different sensor placements to damage. Subsequently, a series of GW signals under various crack lengths was obtained to qualitatively demonstrate the DI calculation method used in this study, specifically the signal windowing technique in the time domain.

To better demonstrate the reflection of the damage-related signal during GW propagation, as well as modal conversion between waveforms, a series of simulations was conducted using a bar with the same dimensions as the SLJ structure. These simulations confirmed the feasibility of using the front-end wave packet to assess the damage extent.

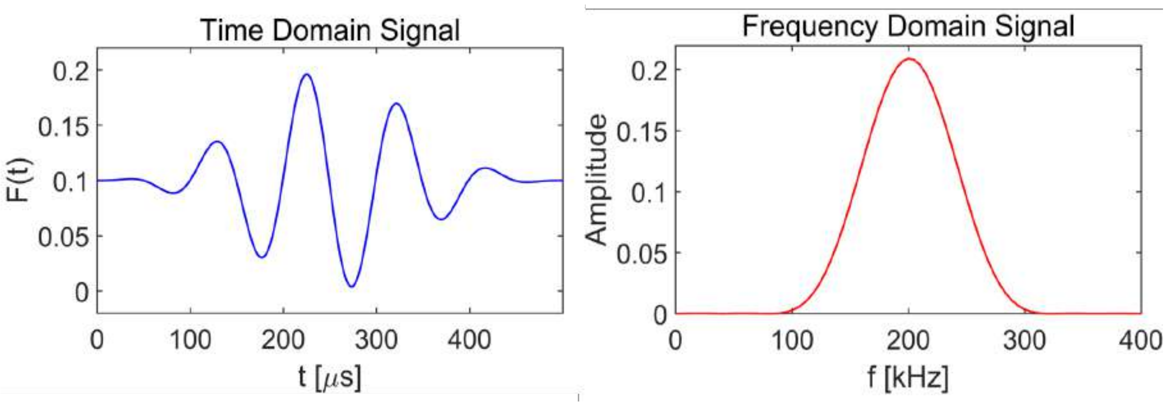

Figure 5.1 The time and frequency signal distribution of a five-cycle tone burst signal centred at 200 kHz.

A 10 mm PZT sensor was employed to excite and record GW signals, aiming to establish the correlation between crack length and the corresponding scattered signal. Initially, a simulation was conducted on a single CFRP bar containing a 0.5 mm crack. A five-cycle tone burst excitation signal centred at 200 kHz, as illustrated in Fig. 5.1, was applied to verify the effectiveness of GW-based detection, with the results shown in Figs. 5.2 and 5.3.

By comparing the GW signals recorded at three different measurement points, it is observed that the scattered signals at points 1 and 2 produce similar effects during analysis, making it difficult to separate damage-related information when both are used simultaneously. A comparison between points 2 and 3 reveals that the modal conversion and scattering behaviours observed upon encountering damage are also similar. Therefore, selecting points 2 and 3 as the locations for signal reception is effective for damage assessment. In this study, PZT sensors are placed on both sides. Consistent with the simplified model, it is feasible to measure scattered signals corresponding to damage of the adhesive zone using this configuration. Fig. 5.4 shows the geometric model with two PZTs implemented in the simulation environment.

The experimentally measured GW signals corresponding to three crack lengths are shown in Fig. 5.5. A windowing method is applied to capture the useful information from the second

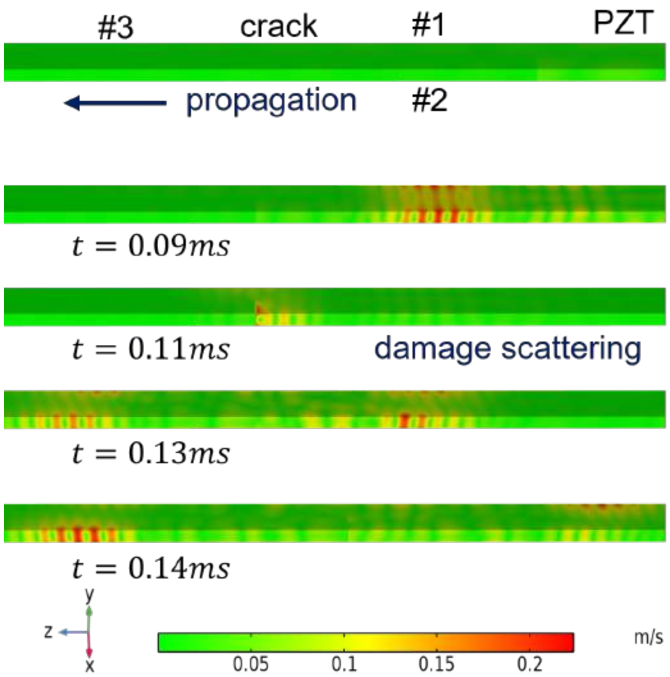

Figure 5.2 GW field and damage scattering signal of strip structure damage detection at different times.

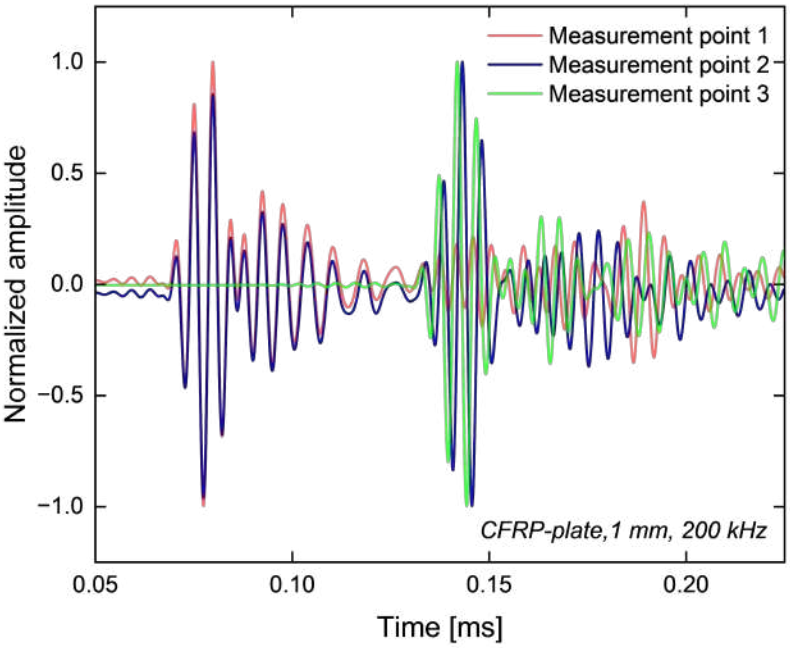

Figure 5.3 The GW signals obtained at different measurement points for the sample in Fig 5.3.

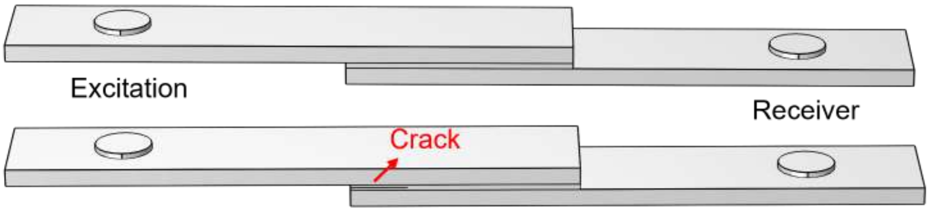

Figure 5.4 The geometric model of the SLJ structure with and without damage in COMSOL FEA simulation environment.

wave packet, and the correlation coefficient between this signal and the reference signal is calculated to obtain a preliminary DI.

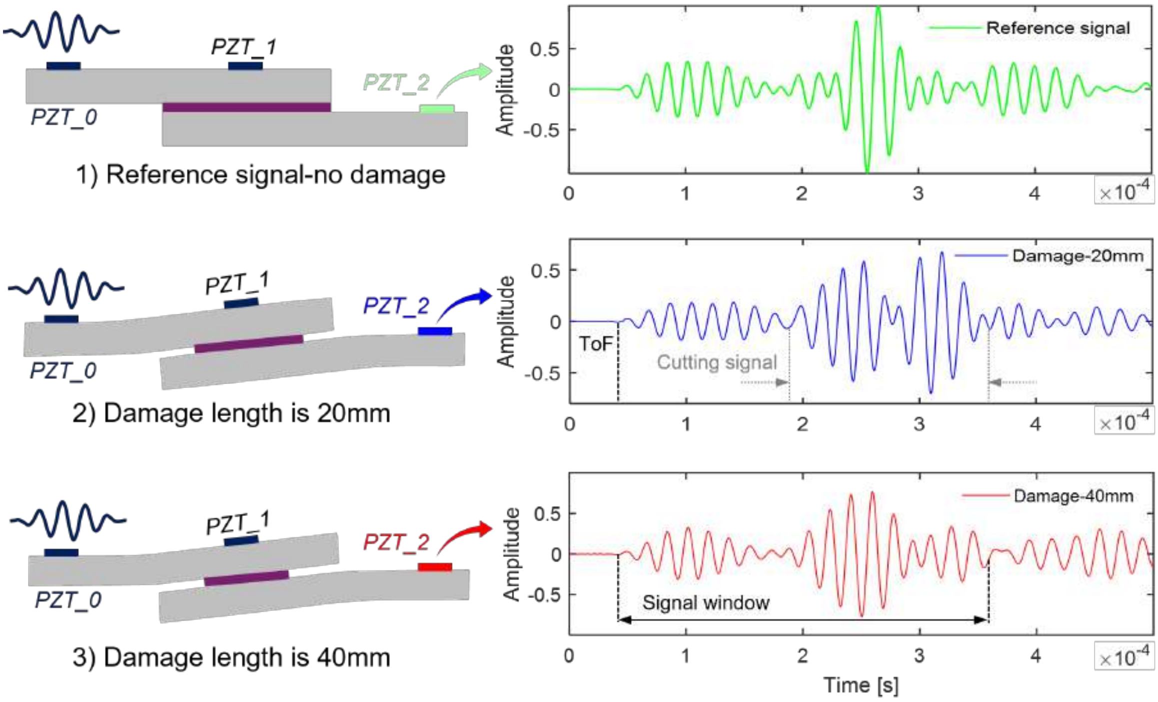

Figure 5.5 The diagram of the measured GW signals corresponding to different damage extents of the bonding zone and signal processing method.

Fig. 5.5 presents the results demonstrating the signal windowing approach employed in this study. The analysis emphasises the extraction of the first two wave packets, which are rich in damage-related information and primarily reflect the structural integrity of the bonding zone. By calculating the ToF at various centre frequencies, the initial two damaged wave packets are isolated. These extracted signals are then subjected to correlation analysis based on the method defined in Eq. (5.1). The resulting values are fitted to establish the relationship between DI and crack length (α). This analytical process underpins the research findings presented in this dissertation, such that:

$$DI = \frac{\mathrm{Cov}(\mathrm{GW}_h, \mathrm{GW}_d)}{\sqrt{Var(\mathrm{GW}_h)Var(\mathrm{GW}_d)}} = \frac{E\left[(\mathrm{GW}_h - E(\mathrm{GW}_h))(\mathrm{GW}_d - E(\mathrm{GW}_d))\right]}{\sqrt{Var(\mathrm{GW}_h)Var(\mathrm{GW}_d)}}, \tag{5.1}$$

where the mathematical operators Cov, E, and Var represent the covariance, mean, and variance of the signal, respectively. GW_h and GW_d denote the reference GW signal and the damage-scattered signal (windowed) at the same sensor location.

5.2.2 Experiments on damage detection using guided waves

This subsection first introduces the experimental setup, followed by a description of the geometric parameters of the specimen. Subsequently, full wavefield scanning of the SLJ structure was conducted using SLDV. Finally, the GW signals acquired by PZT sensors were used to compute the DI.

First, the experimental set-up and on-site equipment are shown in Fig. 5.6 and 4.7. PZT sensors positioned on both sides of the bonding zone are used to excite and measure the GWs. This experiment focuses on capturing the scattered GW generated by damage within the bonding zone, computing the DI using the method described in Eq. (5.1), and subsequently estimating the damage extent.

Subsequently, Fig. 5.7(a) introduces the geometric parameters of the specimen and PZT positions related to the bonding zone, while Fig. 5.7(b) presents the GW signals measured under varying damage levels. The three measured signals indicate that, with the propagation of the crack in the bonding zone, the GW response increasingly exhibits modal conversion components. In particular, the initial wave packet recorded by the PZT sensor contains pronounced modal conversions. The presence and progression of damage can be inferred by analysing the first and second wave packets.

The SLDV experiment was then carried out based on the same specimen described in Fig. 5.7(a). It should be noted that the SLDV data were not incorporated into the proposed framework. Instead, they served exclusively as a supplementary tool for visualising the detailed propagation behaviour of GW through the bonding region. This facilitated a deeper understanding of the wave propagation phenomena and provided a reference for validating the numerical model. Fig. 5.8 shows an on-site photograph of the SLDV experiment conducted on an SLJ structure containing a 20 mm crack, while Fig. 5.9 presents the corresponding full wavefield distribution captured under a 150 kHz excitation.

The full wavefield scanning results demonstrate that a crack in the bonding area produces a weak reflected wave detectable via SLDV. Although this reflection resembles boundary-

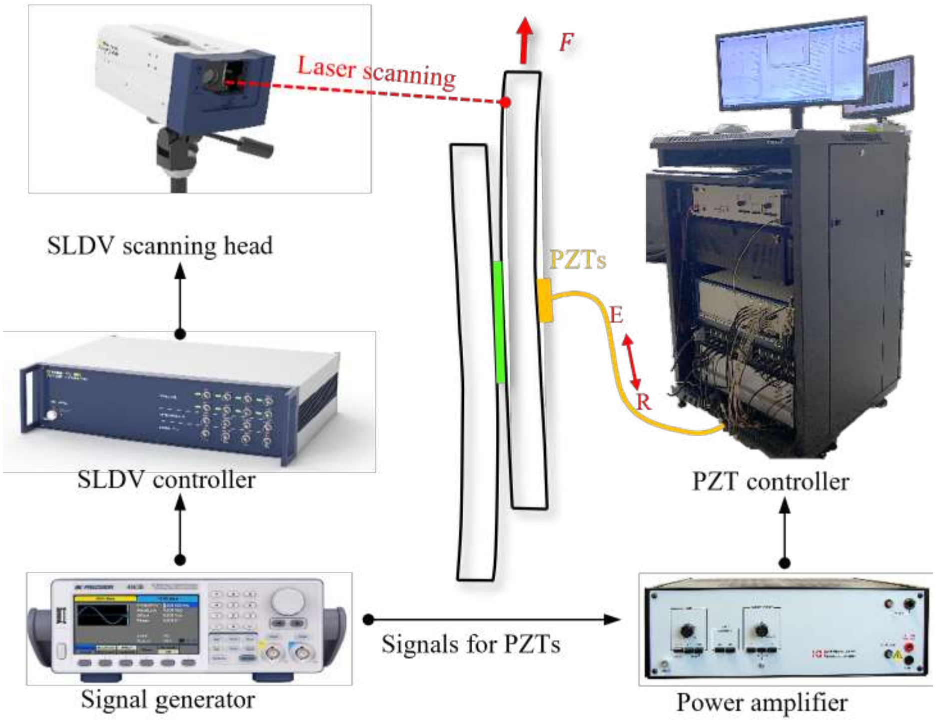

Figure 5.6 Diagram of the experimental set-up.

induced reflections in appearance, it possesses significantly lower energy. This observation further confirms the feasibility of using recorded GW for damage analysis in bonded structures.

In addition to the GW experiments under varying damage conditions shown in Fig. 5.7(b), this dissertation also analysed the GW signals recorded at different excitation frequencies. To further identify the most suitable frequency for assessing damage in the bonding zone, a series of GW-based experiments was conducted under fixed damage conditions while varying the excitation frequency. By comparing the responses measured by the PZT across these frequencies, the optimal range for capturing damage-related features was determined, as illustrated in Fig. 5.10.

As shown in Fig. 5.10, excitation signals with lower centre frequencies struggle to capture damage-related characteristics in a specific period. Therefore, higher-frequency signals are generally preferred for assessing damage in multi-layered structures, despite their increased susceptibility to noise and dispersion. This is because higher-frequency GWs are more sensitive to small cracks and provide better signal amplitude within a given time window, which facilitates clearer signal separation and enhances the measurement resolution.

The measurement locations, excitation frequencies, and measured signals are analysed in conjunction with the method described in Fig. 5.5. PZT-1 and PZT-2 are selected as

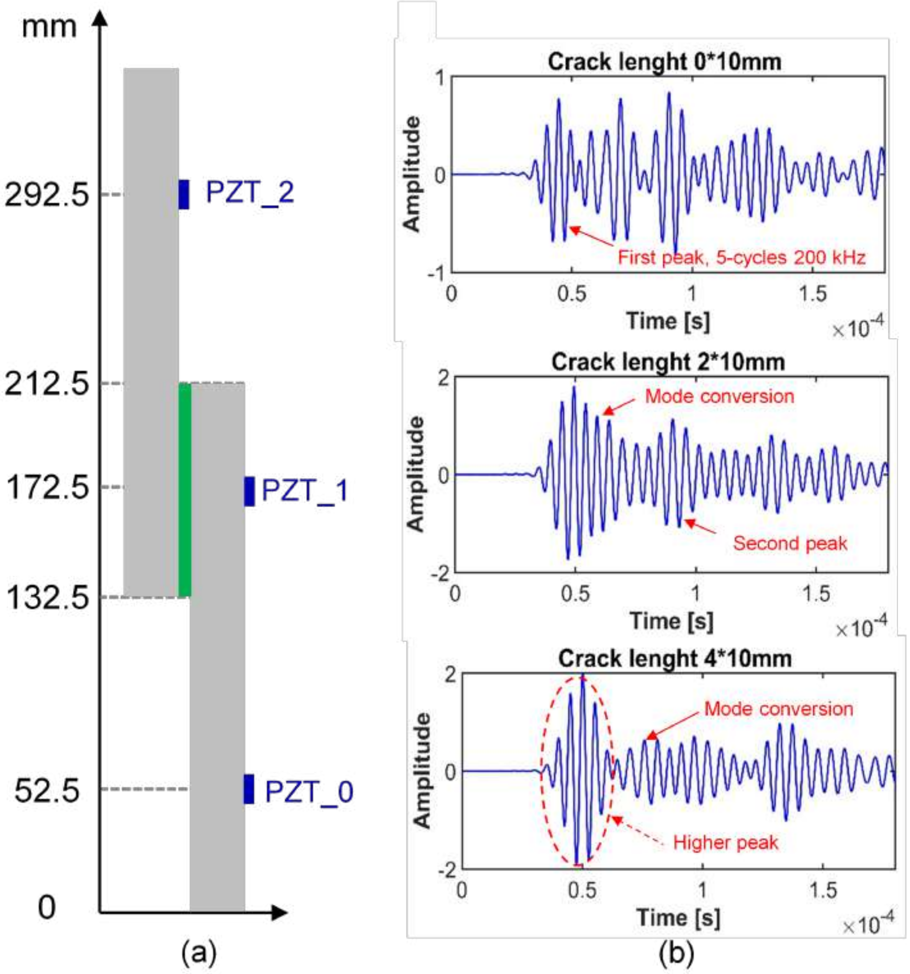

Figure 5.7 The GW signals of the damaged SLJ specimen obtained by experimental measurement, (a) geometric parameters of the experimental specimen, (b) measured GW signals corresponding to different damage extents.

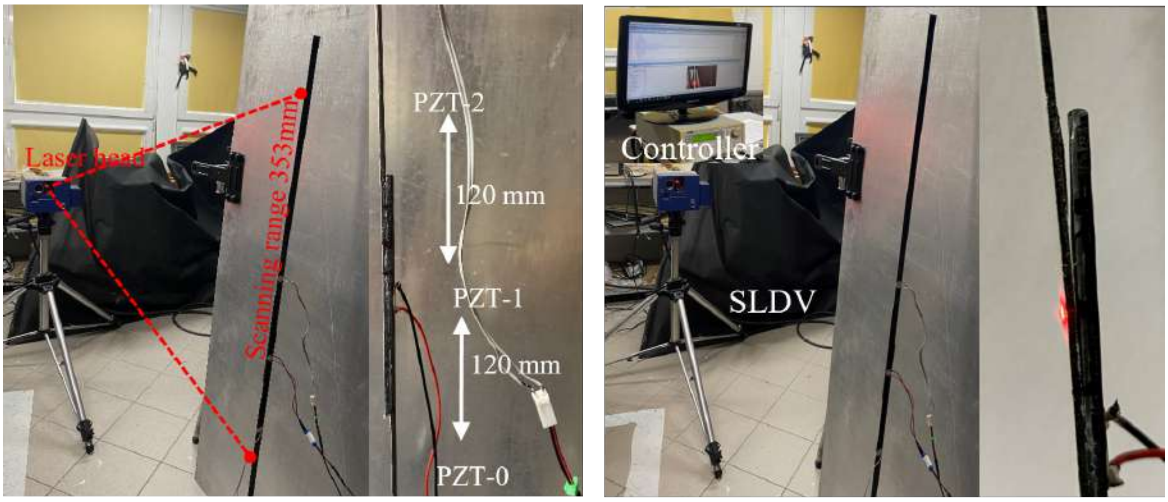

Figure 5.8 SLDV experiment on an SLJ specimen with a 20 mm crack.

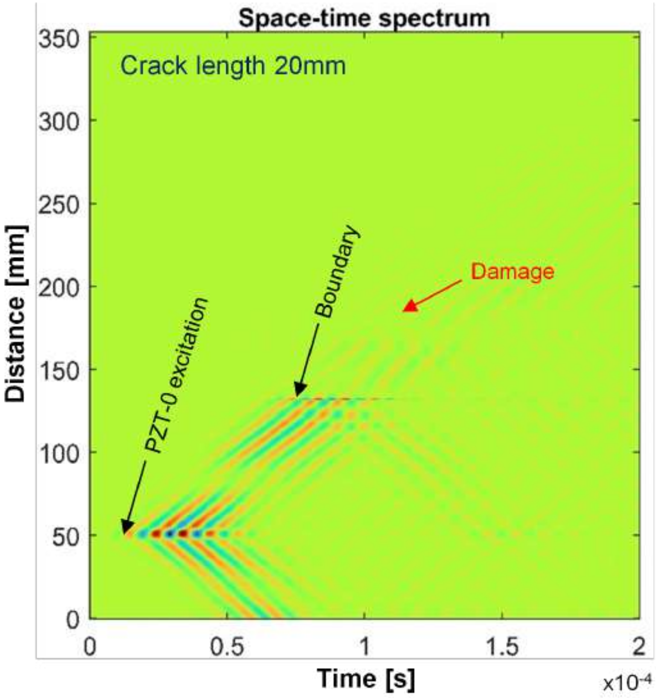

Figure 5.9 The full wavefield diagram obtained by SLDV for SLJ specimen with 20 mm crack.

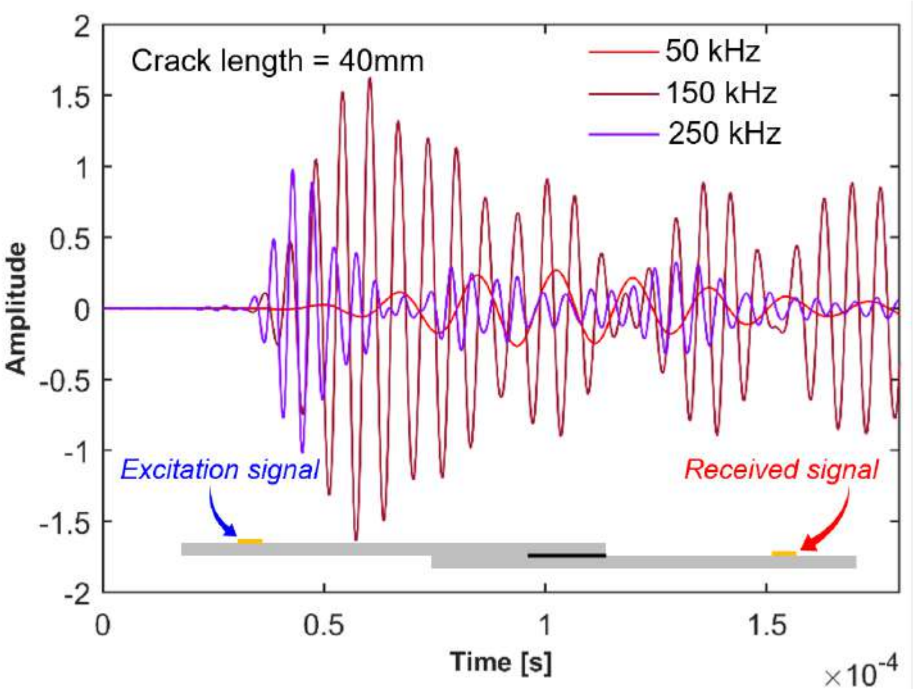

Figure 5.10 Measured GW signal at different frequencies in the adhesive zone with a 40 mm crack length.

receivers for recording GW. DIs are calculated to quantify the damage extent using high-frequency excitation signals (over 100 kHz) based on the analysis of Fig. 5.10. The signal is excited by PZT-0, and the resulting DI values at locations 1 and 2 are used to evaluate which measurement point is more suitable for quantifying the damage extent. Fig. 5.11 presents the DI for frequencies from 100 to 300 kHz calculated using the method described in Subsection 5.2.1.

The relationship between crack length and the correlation coefficient becomes more quantifiable when the excitation frequency is 180 kHz or higher. Different DI values can be used to estimate crack length based on the DI curve. Fig. 5.11 shows that PZT-2 exhibits greater sensitivity to damage extent than PZT-1, as its DI shows larger variation and is more suitable for quantifying crack length. To further examine this correlation, the DI curve corresponding to the 200 kHz excitation was extracted, as illustrated in Fig. 5.12.

A notable difference is observed when quantifying damage using data from PZT-2, where the DI calculation exhibits a minor error. Fig. 5.12 further demonstrates that PZT-2 data provides greater precision than PZT-1 for estimating the extent of damage and offer a more stable assessment at a specific period.

The experimental results shown in Figs. 5.11 and 5.12 indicate that a single DI curve cannot be used to quantify all damage levels across all excitation frequencies. However, a

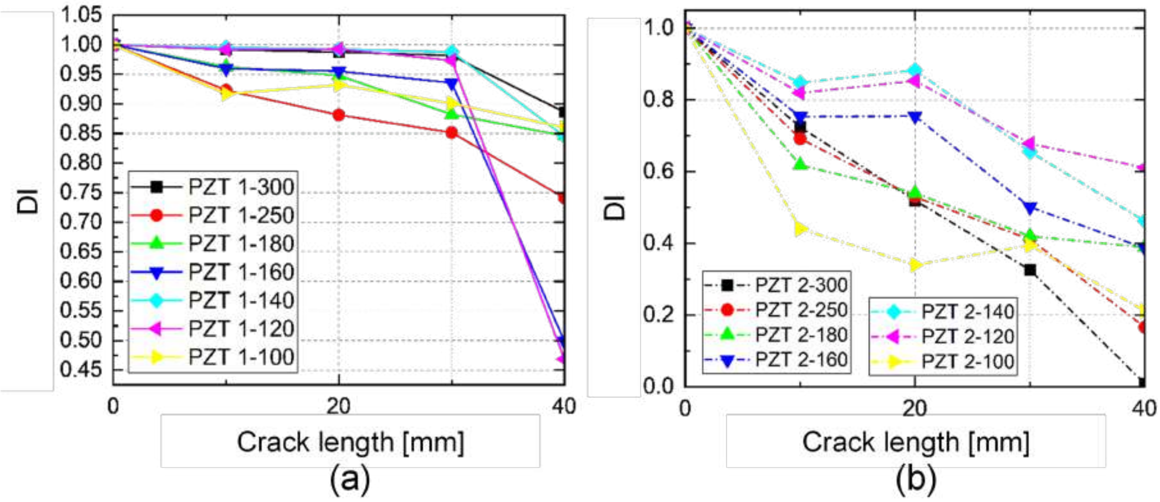

Figure 5.11 DI curves calculated at different frequencies for various measurement locations, (a) PZT-1 is the sensor, (b) PZT-2 is the sensor.

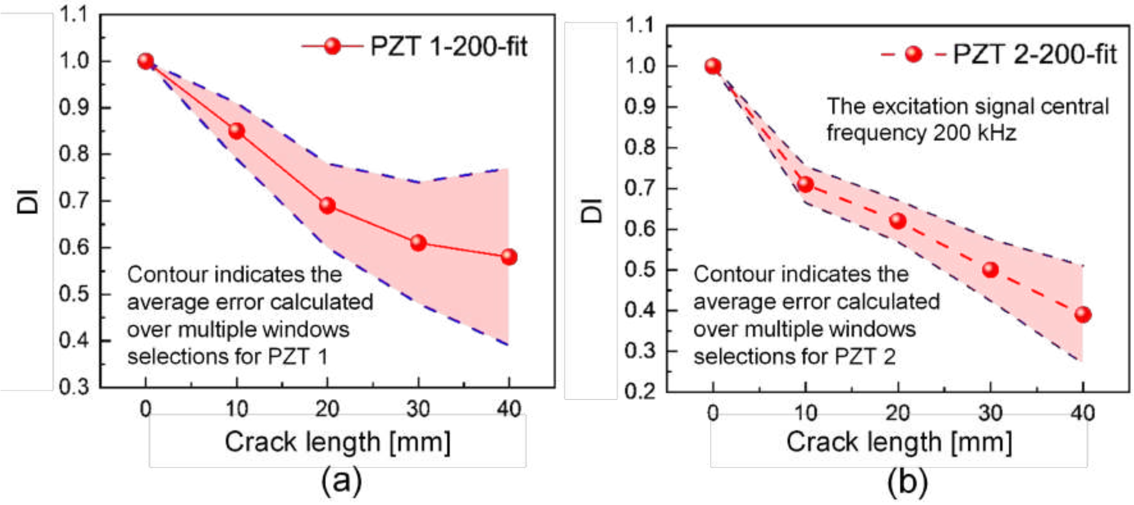

Figure 5.12 DI curves calculated with 200 kHz excitation signal, (a) PZT-1 is the sensor, (b) PZT-2 is the sensor.

DI curve corresponding to a specific frequency can approximately represent damage extent by defining an acceptable error band. In the RUL prediction section, the damage extent is quantified by using the 200 kHz DI curve, as shown in Fig. 5.12(b). This variation is more relevant for assessing the extent of damage progression rather than determining an exact crack length or a specific numerical value of the damage. This dissertation focuses on using a single-frequency DI curve for damage quantification, rather than covering the full frequency spectrum. Within a limited error margin, the DI curve still reflects the relationship between crack length and damage extent. In the SLJ structure with larger cracks, more signal components are present, including not only damage-related scattering but also various boundary reflections. As a result, the selection of windowing signal components for DI calculation may become more complex, leading to larger errors compared to cases with smaller cracks. The comparative results are presented in Fig. 5.13.

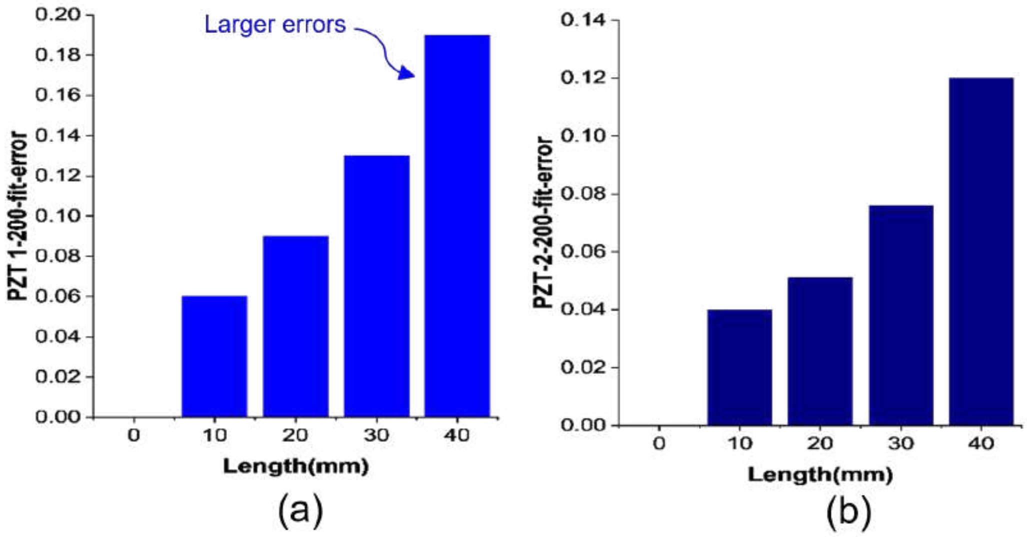

Figure 5.13 Error bar graph of DI calculated for PZT-1 and PZT-2 at different damage extents.

5.3 Fatigue crack propagation simulation

Crack propagation is modelled using the FCP solver in conjunction with FEA. The FEA provides the necessary input parameters for the solver, while the FCP model generates the crack–fatigue curve, enabling the simulation of the nonlinear crack growth process.

High-cycle fatigue behaviour is simulated using the XFEM with an initial crack size of 5 mm and user-defined subroutines. The simulation parameters include a load ratio of 0.1 and a maximum principal stress of 10 kN. The specimen geometry is shown in Fig. 5.7. The stress–strain curve and material properties used in the model are presented in Fig. 5.14 and Tab. 5.1, respectively.

Table 5.1 Material properties of 8552 carbon fiber/epoxy UD laminates and AV138 two-component epoxy.

Property	**8552 carbon fiber**	**AV138 two-component epoxy**
Elastic modulus E (MPa)		
E_{11}	11380	–
E_{22}	320	–
E_{33}	320	–
E	–	4890
Tensile strength (MPa)		
t_n	–	39.5
t_s	–	30.2
Poisson's ratio ν		
ν_{12}	0.43	–
ν_{23}	5.17	–
ν_{13}	0.43	–
ν	–	0.35
Shear modulus G		
G_{12}	3980	–
G_{23}	739	–
G_{13}	3980	–
G	–	1560
Fracture toughness G_{IC} / G_{IIC}		
G_{IC}	–	0.2
G_{IIC}	–	0.38

The experiment is conducted using 8552-carbon fibre composites as the adherend and AV138 adhesive as the bonding material. To reduce the number of fatigue loading cycles and computation time, a segmented fatigue loading strategy is employed. A static load is initially applied to accelerate structural degradation, and a non-damage model is adopted as the static constitutive relationship. Based on the S–S curve presented in Fig. 5.14, fatigue loading is introduced once the maximum load is reached. At this point, the mechanical behaviour of

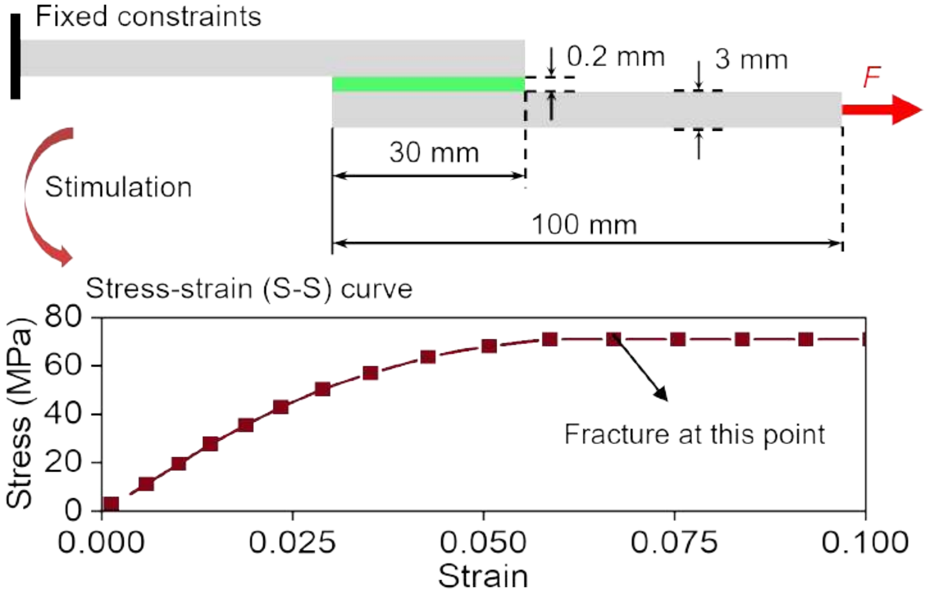

Figure 5.14 Stress-strain curve of SLJ structure.

the integration points in the elements is governed by the fatigue constitutive model. The corresponding loading strategy for fatigue stress is illustrated in Fig. 5.15.

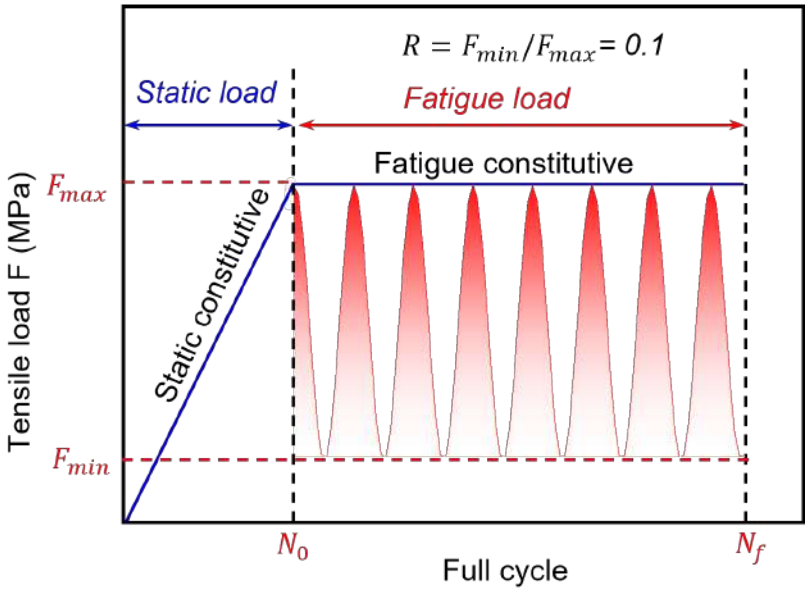

Figure 5.15 Fatigue stress loading strategy for SLJ structures.

The fatigue stress propagation in the SLJ structure is shown in Fig. 5.16, presenting the simulation results under different ultimate fatigue damage cycles (N_f) based on the user-defined fatigue subroutine.

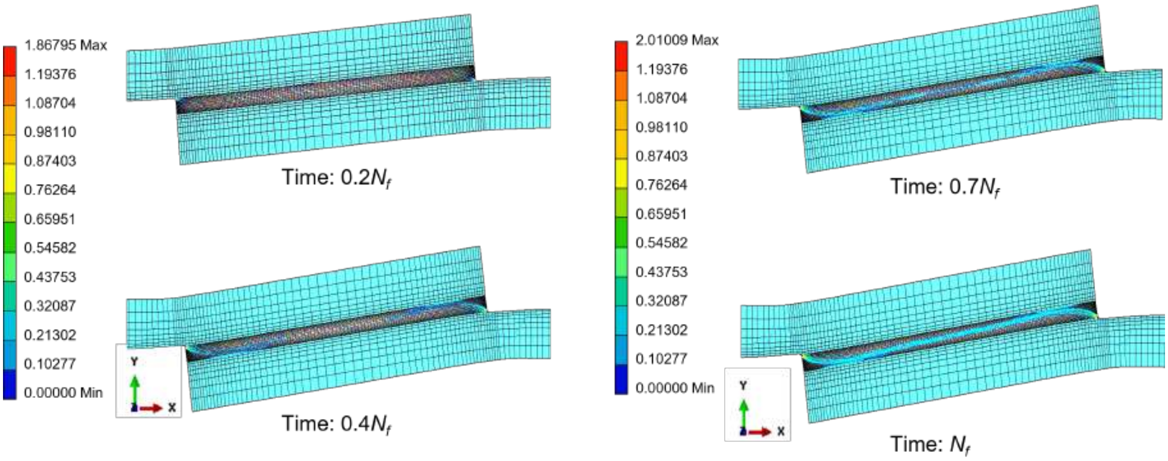

Figure 5.16 Simulation results of fatigue stress propagation in SLJ structure.

It can be observed that the damage in the bonding zone gradually extends from the initial crack location to the bonding boundary and then extends to the middle position. Thus, employing a method that neglects the adhesive thickness and crack propagation direction does not accurately reflect the actual crack propagation process. Additionally, the FEA results reveal that as the crack approaches the EoL, its propagation rate ($d\alpha/dN$) increases significantly, indicating a typical nonlinear crack growth behaviour. To more intuitively illustrate this nonlinearity, the corresponding trend is illustrated in Fig. 5.17.

Finally, Fig. 5.18 presents the simulation data obtained using the FCP solver and FEA, which shows the trend of crack growth in the bonding area as the fatigue cycles progress (α-N_f). XFEM method does not simplify the information in the bonded zone as CZM, highlighting the deflection of cracks in the bonded area and thus more accurately representing the actual crack phenomenon.

5.4 Predicted results with quantified uncertainty

This section analyses the results obtained from the CNN–LSTM architecture with dropout. The prediction model primarily uses the experimental and simulation data described in Sections 5.2 and 5.3. The focus is on the RUL of the SLJ structure under fatigue loading, along with an evaluation of the predicted results and the quantified uncertainty. Additionally, prediction outcomes from several comparative models are presented to highlight the significance and advantages of the method proposed in this study.

Firstly, a preliminary analysis of fatigue test data and simulation data is conducted, as shown in Fig. 5.19. Specifically, Fig. 5.19(a) presents the fatigue test results for the SLJ

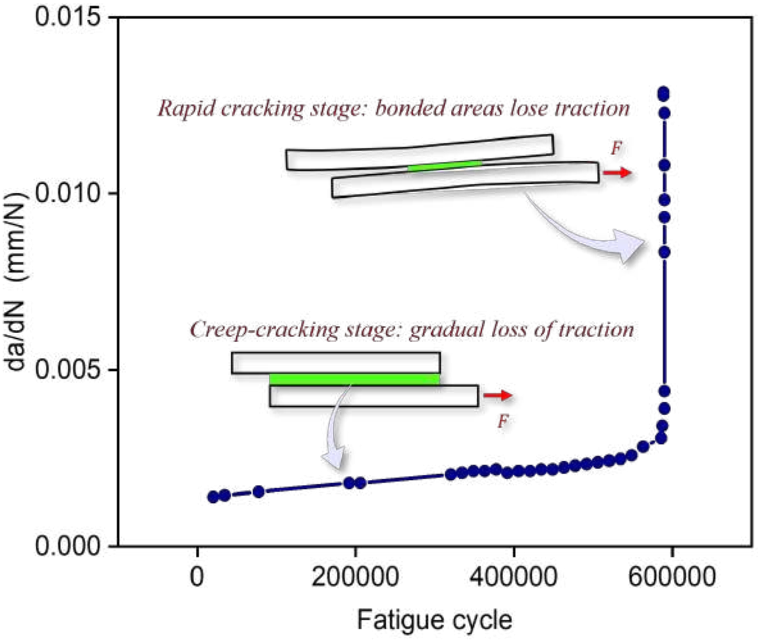

Figure 5.17 The crack propagation rate is calculated based on XFEM.

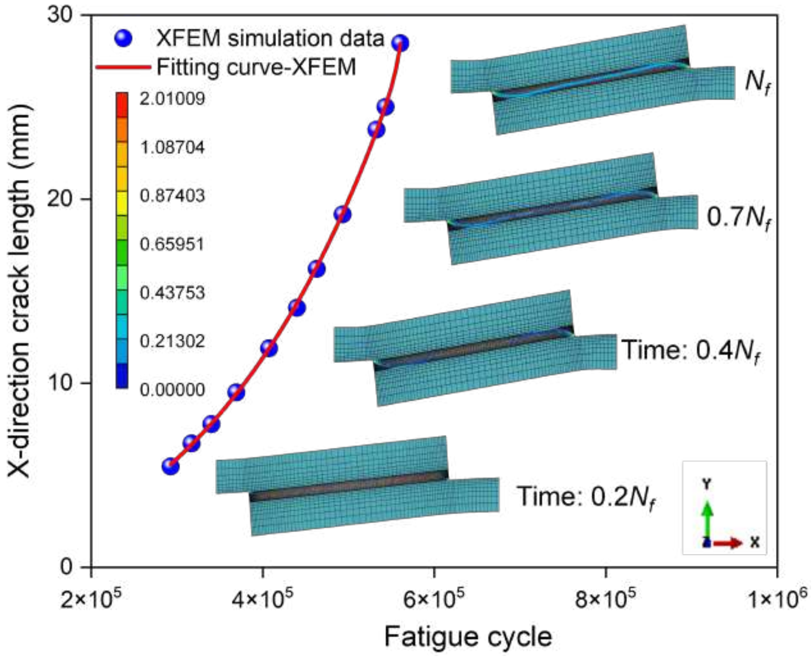

Figure 5.18 Diagram of crack propagation and structural deformation calculated by XFEM method.

structure, which corresponds to the same configuration used in the simulation model. The experimental data were processed by retaining only the points near the fitted curve, thereby emphasizing the overall crack growth trend. Fig. 5.19(b) presents the simulation data with confidence band. To highlight the general trend of the simulation results, a subset of data points that reflect the progression of crack propagation was selected. It should be noted that this does not represent the full set of simulation data obtained.

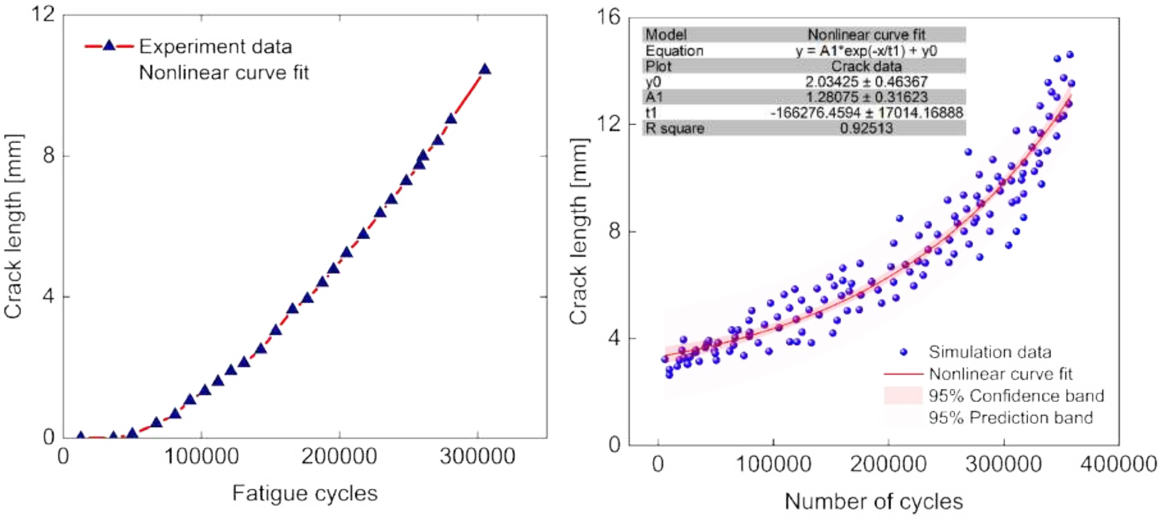

Figure 5.19 Fatigue damage propagation curves of the bonding zone in the SLJ structure obtained by experiment (a) and simulation (b).

A nonlinear curve representing crack propagation is obtained by fitting the experimental and simulation data. The normal probability plots presented in Fig. 5.20 shed light on the statistical characteristics of the crack length datasets obtained from experiments and simulations. In Fig. 5.20(a), the experimental data show notable deviation from the reference line, particularly at the lower percentiles (below 15%), suggesting increased scatter in the early stages of crack growth. This deviation is likely attributed to initial manufacturing defects, measurement uncertainty, or inconsistencies during data acquisition. The corresponding statistical parameters ($\mu = 6.83$, $\sigma = 3.28$) reinforce this observation, indicating a relatively wide spread and a higher level of uncertainty in the measured data. Given the limited availability of experimental data, Gaussian noise is introduced into the experimental data to enrich the dataset and improve the robustness of the subsequent RUL modelling. The simulated data in Fig. 5.20(b) demonstrate a stronger alignment with the reference line across most percentiles, implying that the numerical results follow a near-normal distribution. The mean value is slightly elevated ($\mu = 7.10$), while the standard deviation is reduced ($\sigma = 3.10$), suggesting enhanced consistency and a more controlled representation of crack progression under simulated conditions.

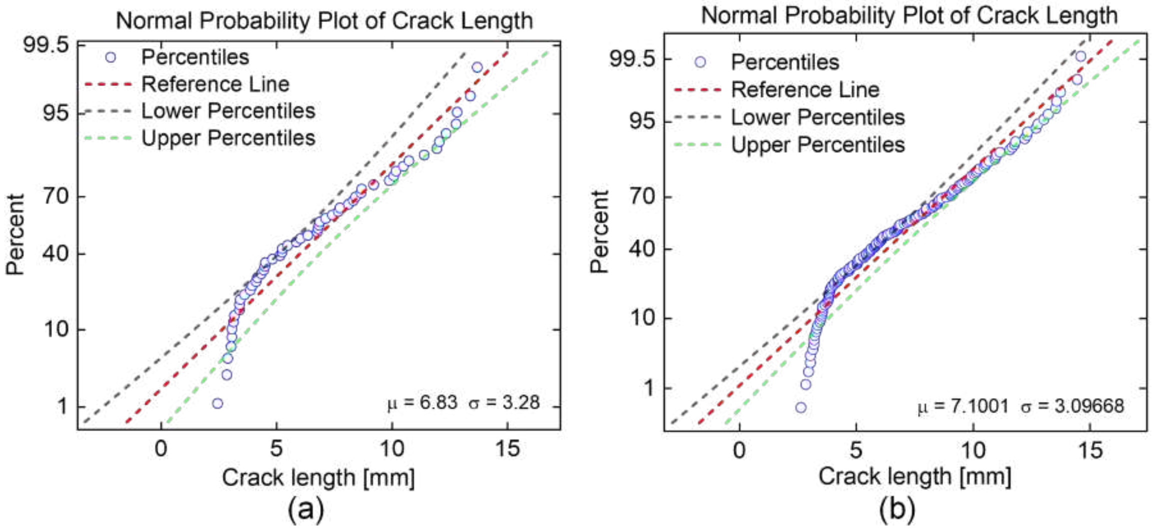

Figure 5.20 Normal probability of crack length data obtained from experiments (a) and simulations (b).

The fitting residuals and corresponding percentages, shown in Fig. 5.21(a), are used to evaluate the quality of the experimental data. Additionally, the normal probability plot assists in identifying outliers within the dataset. Data points that deviate from the reference line are regarded as outliers. This helps explain the substantial deviation observed during the initial stage of RUL prediction, which is likely caused by a high concentration of outliers in both the experimental and the simulation data sets.

Sub-figs. (b) in Figs. 5.19 to 5.21 present the corresponding statistical parameters for the simulation data. The distribution results show that the residuals of the preprocessed data are small, indicating that the overall trend of fatigue crack propagation is similar to the experiment.

The predictive performance of three different RUL models is compared. The input for all models consists of labelled damage extent data in the adhesive zone, represented as α–N_f. The basic parameter settings include an epoch of 150 and a sample size of 200,000×100. Based on experimental results, an approximate EoL of the SLJ structure is determined and used as the benchmark for error evaluation. Tab. 5.2 summarises the performance differences among the three computational models. Accuracy refers to the outcome of single-value RUL predictions made by a NN without MC sampling. A total of 10,000 individual prediction runs were performed, and the number of predictions falling within 5% of the true EoL value was recorded.

Analysis of the computational results indicates that the model proposed in this dissertation offers notable advantages in terms of accuracy and error control. The CNN–LSTM with dropout does not require frequent adjustment of node parameters, in contrast to the BNN,

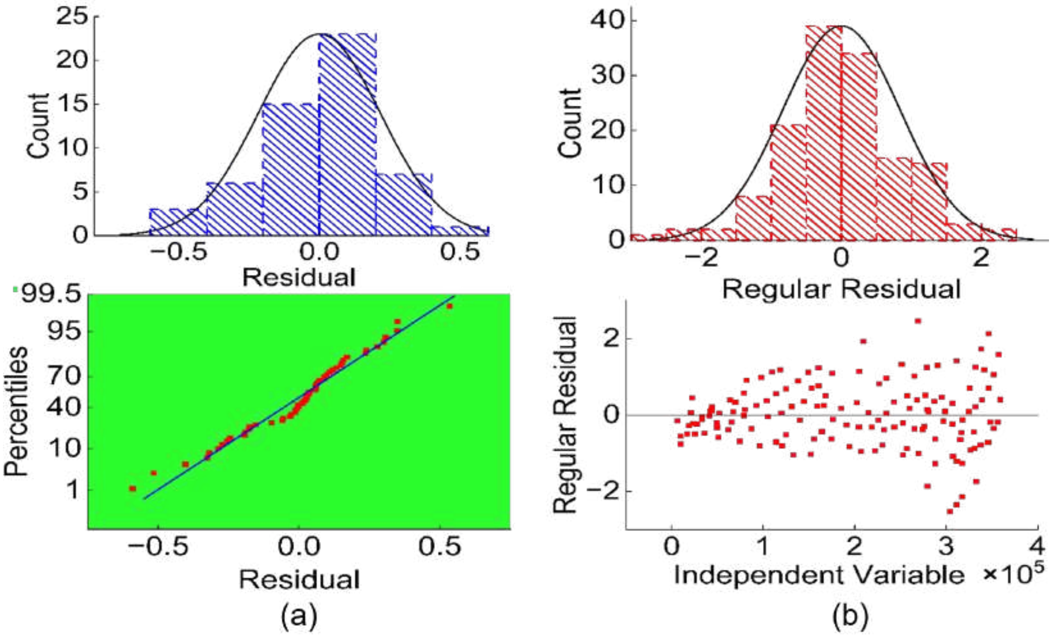

Figure 5.21 Residual distribution and percentiles of the α-N_f curves obtained from experiments (a) and simulations (b).

which involves assigning probabilities to each node and regularly tuning model parameters. As a result, the computation time is also reduced. The results are presented in Fig. 5.22, where Figs. 5.22(a), (c), and (e) show the predictive outcomes of the three different models, while Figs. 5.22(b), (d), and (f) present the corresponding probability density distributions.

In Fig. 5.22(b), the joint probability density plot demonstrates that the high-density (dark blue) is concentrated near the EoL range, approximately between 2.5×10^5 to 3.5×10^5. It is important to note that the density distribution captures all prediction outcomes, including those with significant deviation, such as predictions near 2.0×10^5, thus representing the global uncertainty rather than merely the best-performing outputs. By contrast, the high-density regions in Figs. 5.22(d) and (f) are exhibiting asymmetry and a wider spread. This reflects increased variance and reduced predictive precision, suggesting that these models struggle to produce consistent and accurate RUL predictions across different fatigue stages.

The performance of the CNN model in predicting RUL exhibits relatively large fluctuations compared to CNN–LSTM and BNN, as illustrated in Fig. 5.22(e). These substantial variations introduce instability in practical applications and complicate uncertainty quantification. From the comparative results in Fig. 5.22(a) and (c), it is evident that the CNN–LSTM model (without sampling) yields a prediction (3.45×10^5) that is closer to the experimental EoL (approximately 3.60×10^5). Simultaneously, from the comparison between Fig. 5.22(b) and (f), the overall prediction probability of CNN–LSTM with dropout is significantly higher

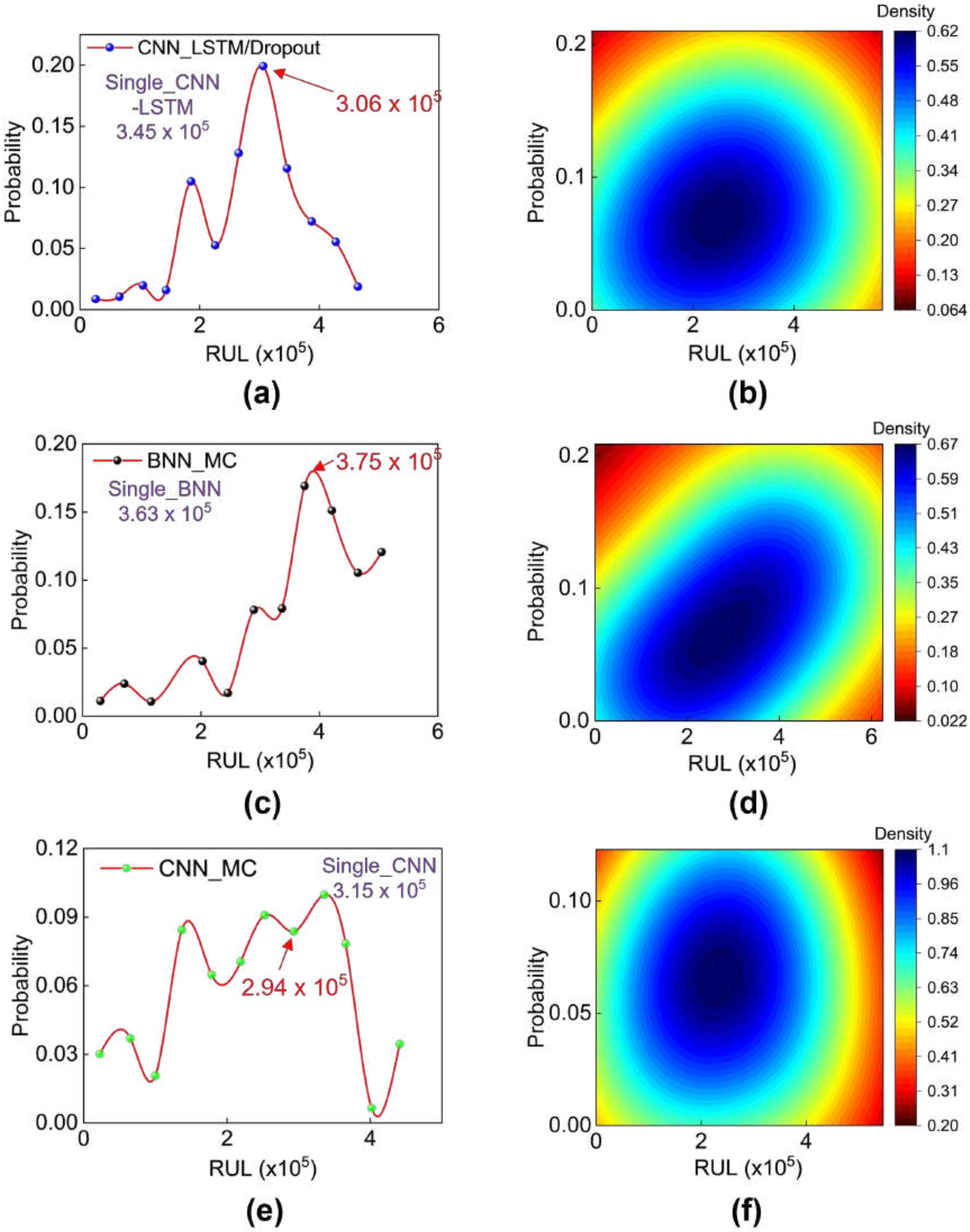

Figure 5.22 Prediction of the EoL using different models, (a) value and probability curve of EoL calculated using the model proposed in thesis, (c) prediction results after MC sampling calculated using the BNN model, (e) prediction results after MC sampling calculated using the CNN model, (b), (d) and (f) represent the probability density of the corresponding data distribution.

Table 5.2 Comparison of the results of predicting a single numerical EoL using different models.

Index	CNN-LSTM with Dropout	BNN-MC	CNN-MC
Test accuracy (%)	89.52%	73.09%	70.40%
Train accuracy (%)	92.71%	88.70%	80.35%
Test RMSE	3.2	4.0	4.5
Train RMSE	2.8	3.6	3.9
Error uncertainty (%)	10.48%	26.91%	29.60%
Overfitting probability	Low	Medium	High
Input data size	200,000 × 100	200,000 × 100	200,000 × 100
Model complexity	Medium	High	Low

than that of the CNN-MC model alone. Furthermore, Fig. 5.22(a) indicates that the prediction results of the CNN–LSTM with dropout and MC sampling model exhibit a more uniform normal distribution, with improved stability compared to the BNN method. However, in terms of single-value prediction, the BNN performs well (3.63×10^5), attributed to its more complex network structure. Nevertheless, its probability density distribution is uneven, which may lead to polarised prediction results.

Following the results presented in Fig. 5.22, the effectiveness of the CNN–LSTM architecture with dropout for RUL prediction and uncertainty quantification is discussed. The data segmentation method illustrated in Fig. 4.1(d) is adopted. Data up to 2.5×10^5 cycles (displayed in Fig. 5.23 with a 100:1 density) are used as training dataset, while the range between 2.5×10^5 and 3×10^5 is reserved for testing. Fig. 5.23 shows the EoL prediction results obtained from two different algorithms. Based on Fig. 5.19(a), the actual service life of the SLJ structure falls within the range of approximately 3.0×10^5 to 3.6×10^5. The conventional BNN approach estimates the fatigue life around 3.3×10^5, with 73.09% of the 400 prediction runs falling within the actual service life range. However, both RUL_{min} and RUL_{mean} deviate significantly from the observed values. In contrast, the method proposed in Section 4.2 yields a more accurate distribution of RUL predictions. Among 400 calculation runs, 89.52% of the predicted RUL values fall within the actual service life range. Moreover, both the average and RUL_{min} align closely with the experimental observations.

Furthermore, the predicted whisker diagram of the full lifecycle is illustrated in Fig. 5.24. The trend observed in the whisker plot indicates that prediction error decreases as the fatigue cycle progresses. However, in the early stages, the prediction error is still relatively large due

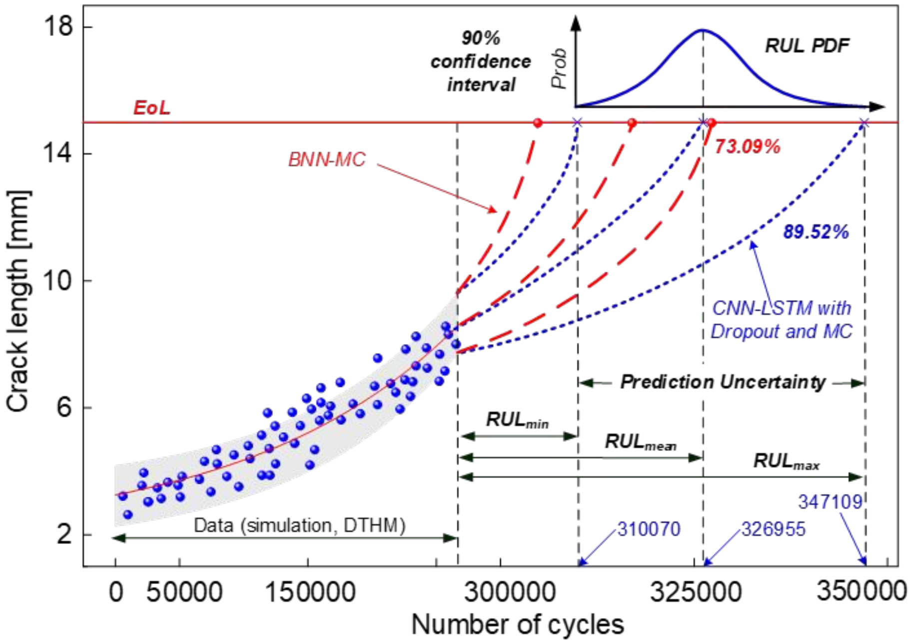

Figure 5.23 Comparative analysis of EoL and RUL prediction results using the BNN model and the CNN-LSTM with dropout and MC sampling model.

to substantial fluctuations in the input training set. Moreover, there is a significant disparity between the early and late stages of the simulation data. The damage propagation curve in the early phase depends on a large number of training data, whereas the later fatigue stages can be characterised using relatively fewer data. In addition, the lower quality of data filtering during the initial fatigue cycle also contributes to the unsatisfactory accuracy of early-stage predictions.

To improve the accuracy of the prediction results, data density is increased during the initial stage. Before 1.8×10^5 fatigue cycles, the original data density is enhanced by 30%. The additional data points are generated based on the fitted curve with Gaussian noise derived from the original simulation and experimental datasets. Furthermore, during input data preprocessing (prior to normalisation and labelling), 10% of the outliers lying outside the 95% confidence interval of the fitted curve are removed. The resulting dataset, with a simulation-to-experimental data ratio of 5:1, forms the updated training dataset. The corresponding prediction results are presented in Fig. 5.25(a).

The optimised training dataset does not lead to a significant improvement in initial prediction accuracy. Although the predicted RUL increases by approximately 23.8% at the onset of crack propagation (0.4×10^5) in the adhesion region, the RUL predictions subsequently deviate from the experimental results. This deviation is clearly visible around a fatigue life of 1.2×10^5 in Fig. 5.25(a). This phenomenon is attributed to the extensive

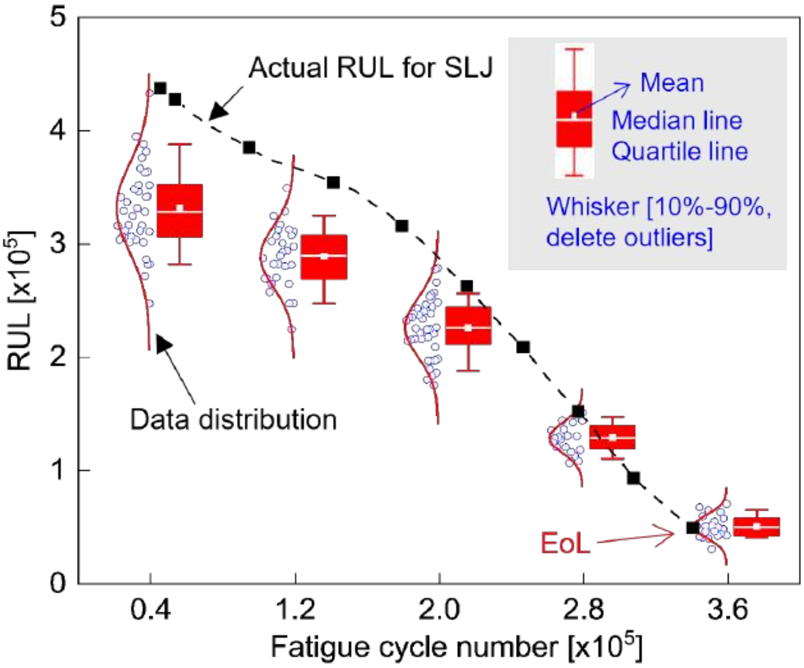

Figure 5.24 RUL degradation curve predicted using DTHM model.

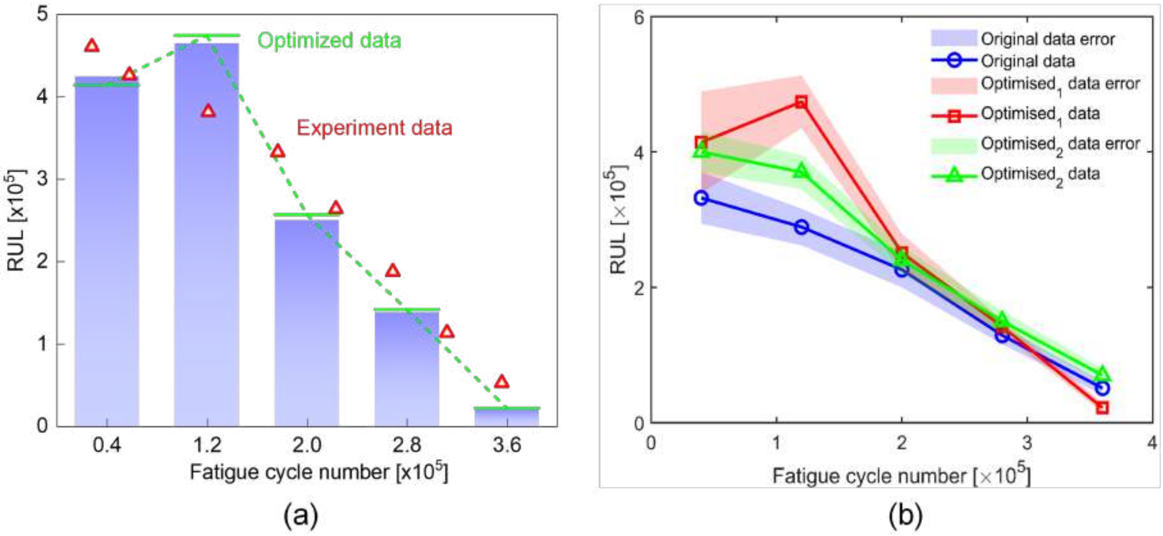

Figure 5.25 Comparison of RUL reduction curves after segmentation and augmentation of input data, (a) comparison between the prediction results and experimental data after original data enhancement and partial outliers filtering, (b) comparison of the prediction results after optimizing the data and parameters.

application of the dropout method within the model, where a low dropout probability is set for each hidden layer, resulting in alternating underfitting and overfitting. Moreover, incorporating a large amount of experimental data during the early stage contributes to overfitting, which is not unexpected. To address this issue, the input dataset is compressed by reducing 5% of the experimental data and enabling a portion of the network nodes. The resulting training outcomes demonstrate reduced overfitting, as indicated by the green curve (triangle marker with filled colour) in Fig. 5.25(b). In this figure, the original curve represents predictions without refined input processing, the first optimised dataset corresponds to Fig. 5.25(a), and the second times optimised dataset (optimised$_2$ data) illustrates the revised input strategy designed to address overfitting.

The comparative results shown in Fig. 5.25(b) demonstrate that the proposed framework effectively predicts the RUL and EoL, even in the presence of considerable noise within the training dataset. After optimisation of the training data, the framework also provides reasonably accurate RUL predictions for early-stage fatigue damage. However, the predicted values still exhibit slight deviations from the experimental data during the latter fatigue cycles (beyond 2×10^5), which can be attributed to the inherent instability of early-stage RUL predictions. From an industrial perspective, the ability to predict RUL and EoL under high-cycle fatigue conditions during early-stage damage is both more challenging and more critical for practical applications.

5.5 Summary

As the final chapter of this thesis, it presents the calculation results of the diagnosis–prognosis framework. A method for determining DI to assess damage extent is proposed based on measured GW. In addition, the dataset for the DT model is generated by integrating a user-defined fatigue subroutine into the FEA and FCP solver, representing the crack propagation process in the bonding zone of the SLJ structure under fatigue loading.

Initially, crack damage in the bonding zone is quantified using GW. Experimental results indicate that high-frequency excitation signals characterise damage more sensitively than low-frequency signals, as lower-frequency wave packets convey less amplitude within the same time window. Therefore, a five-cycle tone burst signal centred at 200 kHz is applied to assess damage extent in the bonded zone. PZTs were placed on both sides of the bonding area, with one functioning as the actuator and the other as the sensor.

Next, the same geometric model is constructed in Abaqus to calculate the S–S and α–N_f curves. A material property estimation method based on the S–S curve is adopted to eliminate the need for extensive experimental testing to determine the mechanical parameters of the bonding zone. In addition, XFEM and FM approaches are implemented within the Abaqus environment to simulate fatigue damage propagation using a user-defined high-cycle fatigue subroutine. The results demonstrate that XFEM outperforms CZM by providing a more realistic representation of damage in the bonding area, with the resulting α–N_f curve closely matching the experimental data, where the EoL is approximately 3.45×10^5. The CZM model does not account for crack deflection in the bonding layer, which is modelled with a simplified viscous constitutive relationship.

Finally, the DTHM is executed to obtain the RUL prediction results. The prognosis model is based on CNN-LSTM and incorporates the dropout method to approximately replace BNN for uncertainty quantification. The results indicate that the predicted EoL from the CNN–LSTM model with dropout and MC sampling are 16.43% higher than BNN. The resulting probability density function of RUL aligns more closely with the mean EoL within the 95% confidence interval. This suggests that a greater proportion of prediction results fall near the true EoL value. However, the use of dropout for BNN approximation still results in significant error in the early stage, which may be attributed to the size of the experimental dataset or suboptimal dropout parameter settings. After refining the input by enabling selected nodes and reducing the experimental data volume, the predicted RUL curve more closely matches the actual structural lifecycle compared to the unprocessed case.

Chapter 6

Conclusion and future work

The thesis of this dissertation is to propose a diagnostic-prognostic framework based on DT technology to detect damage and predict RUL for the adhesively bonded composite structure. To support this thesis, a DTHM is proposed, built upon established SHM techniques using GW and data-driven RUL prediction models. This framework focuses on the SLJ structure, utilising GW to quantify damage within the bonded region, and applies three types of DL-based models—CNN, BNN, and CNN–LSTM with approximate Bayesian inference, for RUL prediction. Among them, the proposed DTHM enables probabilistic RUL prediction, uncertainty quantification, and confidence interval estimation, offering a more valuable and practical reference for lifecycle assessment. The principal research of this dissertation are summarised as follows:

A method for damage quantification in bonded composite structures is developed by calculating DI based on measured GW. The approach extracts damage-related features using windowed GW, correlates them with a reference signal, and establishes a relationship between DI and crack length.

To overcome the limitations of CZM in simulating crack growth within the bonding zone, a combined XFEM and FCP solver approach is employed to model nonlinear crack propagation. It allows simulation of crack deflection in the adhesive region and continuous fatigue crack growth under high-cycle fatigue.

Given the limitations of conventional DL methods in uncertainty quantification, a BNN is developed for RUL prediction of SLJ structures. By introducing aleatory and epistemic uncertainties and applying variational inference, the model outputs a probabilistic distribution of RUL, enabling confidence interval estimation.

In response to the computational complexity and inefficiency of BNN, a dropout-based approximate Bayesian inference method is proposed. By combining CNN–LSTM architecture with MC sampling, the model achieves both high accuracy and efficient uncertainty quantification in RUL prediction.

Comparative evaluations of classical RUL models highlight the superiority of the proposed CNN–LSTM with dropout approach in uncertainty quantification, accuracy, and robustness.

The issue of poor accuracy in early-stage RUL prediction is addressed. The shortcomings of using dropout-based NN to approximately replace BNN are discussed, and prediction performance is improved through data augmentation and enabling network nodes.

The comparative analysis of numerical and experimental fatigue data validates the effectiveness of the proposed DTHM in damage diagnosis and RUL prediction, demonstrating clear advantages over conventional models.

In conclusion, the objectives presented in Chapter 1 have been fulfilled, and the thesis of this dissertation has been proven. The following sections summarise the novel contributions, key experimental findings, and the future research potential of the methods proposed herein.

6.1 Original contributions of the research

Based on the state-of-the-art review and the outcomes of both numerical and experimental investigations, several innovative contributions have been identified by the author. These are summarised as follows:

- A GW-based DI was introduced to quantify the damage extent in the bonding zone, enhancing the effectiveness of damage detection in complex composite structures.
- A combination of XFEM and FCP solver was proposed to simulate nonlinear crack propagation. Compared with the conventional CZM, this approach more accurately replicates the actual crack propagation path.
- A diagnostic–prognostic framework integrating FEA, FM, and ML was developed. Through DT technology, multi-model fusion was achieved to support comprehensive damage diagnosis and RUL prediction.
- An approximate Bayesian inference method based on dropout was employed to quantify uncertainty in RUL prediction. This approach reduces the complexity and training time associated with BNN.
- A hybrid CNN–LSTM model was implemented for time-series prediction, combined with multi-layer networks of approximate Bayesian inference to achieve accurate RUL prediction.

- A tailored data preprocessing strategy was proposed to improve prediction accuracy in the early stage. This includes the reduction of outliers in experimental data and optimisation of the dropout nodes.

6.2 Conclusion

This study employs DT technology to enable damage detection and RUL prediction for SLJ structures, demonstrating clear advantages over conventional methodologies and contributing to more efficient SHM. The principal conclusions drawn from the research are as follows:

- The application of GW for damage quantification in the bonding zone demonstrates that positioning PZT sensors on both sides of the adhesive interface is more effective in capturing damage-related information than configurations employing a single-sided or centrally located sensor.
- The lack of correlation between DI and actual damage extent can be mitigated by extracting multiple wave packets from the measured signal, thereby improving sensitivity to varying crack lengths.
- XFEM simulations of bonding damage produce different fatigue life results compared to CZM. For the same structural model and damage configuration, CZM predicts longer fatigue cycles, likely due to its viscous simplification and mesh dependency.
- The parameters required by the T–S law—namely strain and energy—can be estimated empirically via S–S curves and the J-integral, thus avoiding the need for extensive experimental testing.
- For RUL prognosis, the CNN model requires architecture modification to adequately process time-dependent sequences. Without such improvements, predictions tend to fluctuate, and uncertainty quantification becomes unreliable.
- In the SLJ damage scenario presented in this dissertation, the CNN–LSTM with Dropout MC method outperforms the BNN–MC model, yielding 16.43% higher RUL accuracy, and operates at speeds up to 130% faster, demonstrating greater efficiency and accuracy.
- Despite its complexity and computational demands, the BNN still achieves the best point-estimate accuracy among all models evaluated in this study.

- The initial accuracy of RUL prediction can be enhanced by refining the composition and quality of the experimental data in the training set and optimising the dropout probability for selected nodes.

6.3 Future work

The DTHM proposed in this dissertation offers an effective approach for assessing damage and predicting the RUL of the SLJ structure. The model specifically targets crack propagation within the bonded zone, with crack length and fatigue cycles serving as the training data and labelling parameters. The approach has the potential to be extended to other types of bonded composite materials and failure modes. It is worth mentioning that there could be hundreds of such combinations, making it impossible to list all types.

Regarding other failure types, crack-based damage detection and quantification using GWs remains an intuitive and reliable method. Nevertheless, bonded interfaces are also prone to defects such as adhesive voids and debonding. Developing suitable GW-based quantification techniques for these damage modes represents an important direction for future research.

Finally, this study adopts a CNN–LSTM architecture with dropout and compares its performance with that of single-network models to highlight improvements in prediction accuracy and uncertainty quantification. However, further comparison with other hybrid models could enhance the robustness and generalisability of the findings.

In conclusion, there are multiple potential directions for extending this research. Given the high cost of time and resources, future efforts should prioritise applications with the greatest practical value rather than attempting to cover all adhesively bonded structures. Moreover, an emerging area of interest is composite-to-metal bonding, which is increasingly common in industrial applications. Adapting this framework to such hybrid bonding structures would represent a valuable and meaningful extension of the current work.

References

[1] A. Güemes et al. “Structural Health Monitoring for Advanced Composite Structures: A Review”. *Journal of Composites Science* vol. 4.1 (Mar. 2020), p. 13.

[2] D. A. Tibaduiza Burgos et al. “Damage identification in structural health monitoring: A brief review from its implementation to the use of data-driven applications”. *Sensors* vol. 20.3 (2020), p. 733.

[3] C. Rajendran et al. “Evaluation of load-carrying capabilities of friction stir welded, TIG welded and riveted joints of AA2014-T6 aluminium alloy”. *Aircraft Engineering and Aerospace Technology* vol. 91.9 (2019), p. 1238–1244.

[4] H. Jiang et al. “Effect of locking mode on mechanical properties and failure behavior of CFRP/Al electromagnetic riveted joint”. *Composite Structures* vol. 257 (2021), p. 113162.

[5] X. Shang et al. “Review on techniques to improve the strength of adhesive joints with composite adherends”. *Composites Part B: Engineering* vol. 177 (Nov. 2019), p. 107363.

[6] Y. Zhang et al. “Damage Simulation Method for Adhesively Bonded Composite Structures Based on XFEM and Cohesive Hybrid Model”. en. In: American Society of Mechanical Engineers Digital Collection, July 2023.

[7] H. Ge et al. “Guided wave–based rail flaw detection technologies: state-of-the-art review”. *Structural Health Monitoring* vol. 21.3 (May 2022), p. 1287–1308.

[8] Z. Yang et al. “A review on guided-ultrasonic-wave-based structural health monitoring: From fundamental theory to machine learning techniques”. *Ultrasonics* vol. 133 (2023), p. 107014.

[9] M. Mitra, S. Gopalakrishnan. “Guided wave based structural health monitoring: A review”. *Smart Materials and Structures* vol. 25.5 (2016), p. 053001.

[10] W. Ostachowicz, A. Güemes. *New trends in structural health monitoring*. Vol. 542. Springer Science & Business Media, 2013.

[11] W. M. Ostachowicz. “Damage detection of structures using spectral finite element method”. *Computers & structures* vol. 86.3-5 (2008), p. 454–462.

[12] Z. Zhao, N.-Z. Chen. “Acoustic emission based damage source localization for structural digital twin of wind turbine blades”. *Ocean Engineering* vol. 265 (Dec. 2022), p. 112552.

[13] Y. Zhang, M. Radzieński, W. Ostachowicz. “Diagnostic-prognostic framework for assessing the health status of composite structures”. *International Journal of Mechanical Sciences* vol. 278 (Sept. 2024), p. 109461.

[14] B. R. Seshadri, T. Krishnamurthy. “Structural Health Management of Damaged Aircraft Structures Using Digital Twin Concept”. en. In: *25th AIAA/AHS Adaptive Structures Conference*. Grapevine, Texas: American Institute of Aeronautics and Astronautics, Jan. 2017.

[15] L. Saidi et al. “An integrated wind turbine failures prognostic approach implementing Kalman smoother with confidence bounds”. *Applied Acoustics* vol. 138 (Sept. 2018), p. 199–208.

[16] A. Bhaduri, A. Gupta, L. Graham-Brady. “Stress field prediction in fiber-reinforced composite materials using a deep learning approach”. *Composites Part B: Engineering* vol. 238 (2022), p. 109879.

[17] M. Amafabia et al. “A Review of Structural Health Monitoring Techniques as Applied to Composite Structures”. *Structural Durability & Health Monitoring* vol. 11.2 (1), p. 91–147.

[18] A. Rytter. “Vibration based inspection of civil engineering structures Ph. D”. *Aalborg University, Aalborg, Denmark* (1993),

. [19] P. Wilcox. “A rapid signal processing technique to remove the effect of dispersion from guided wave signals”. *IEEE Transactions on Ultrasonics, Ferroelectrics, and Frequency Control* vol. 50.4 (Apr. 2003), p. 419–427.

[20] J. Nienwenhui et al. “Generation and detection of guided waves using PZT wafer transducers”. *IEEE Transactions on Ultrasonics, Ferroelectrics, and Frequency Control* vol. 52.11 (Nov. 2005), p. 2103–2111.

[21] W. Ostachowicz et al. “Damage localisation in plate-like structures based on PZT sensors”. *Mechanical Systems and Signal Processing*. Special Issue: Inverse Problems vol. 23.6 (Aug. 2009), p. 1805–1829.

[22] M. Radzieński et al. “Damage Identification in Various Types of Composite Plates Using Guided Waves Excited by a Piezoelectric Transducer and Measured by a Laser Vibrometer”. *Sensors* vol. 19.9 (Jan. 2019), p. 1958.

[23] *Open Guided Waves: online platform for ultrasonic guided wave measurements - Jochen Moll, Jens Kathol, Claus-Peter Fritzen, Maria Moix-Bonet, Marcel Rennoch, Michael Koerdt, Axel S Herrmann, Markus GR Sause, Martin Bach, 2019*.

[24] Y. Zhang et al. “Spatial domain localization method for multi-damage in plate-like structure based on coefficient matrix of reflected guided waves”. *Journal of Sound and Vibration* vol. 552 (May 2023), p. 117636.

[25] K. Xu et al. “Mode separation of Lamb waves based on dispersion compensation method”. *The Journal of the Acoustical Society of America* vol. 131.4 (Apr. 2012), p. 2714–2722.

[26] C. Xu et al. “A parameter estimation based sparse representation approach for mode separation and dispersion compensation of Lamb waves in isotropic plate”. *Smart Materials and Structures* vol. 29.3 (Feb. 2020), p. 035020.

[27] S. Chen et al. “Generalized dispersive mode decomposition: Algorithm and applications”. *Journal of Sound and Vibration* vol. 492 (Feb. 2021), p. 115800.

[28] L. Zeng et al. “Waveform design for high-resolution damage detection using lamb waves [Correspondence]”. *IEEE Transactions on Ultrasonics, Ferroelectrics, and Frequency Control* vol. 60.5 (May 2013), p. 1025–1029.

[29] J. B. Harley, J. M. F. Moura. “Sparse recovery of the multimodal and dispersive characteristics of Lamb wavesa)”. *The Journal of the Acoustical Society of America* vol. 133.5 (May 2013), p. 2732–2745.

[30] W. Wang et al. “Sparse representation for Lamb-wave-based damage detection using a dictionary algorithm”. *Ultrasonics* vol. 87 (July 2018), p. 48–58.

[31] P. Kudela et al. “Structural Health Monitoring system based on a concept of Lamb wave focusing by the piezoelectric array”. *Mechanical Systems and Signal Processing* vol. 108 (Aug. 2018), p. 21–32.

[32] S. Shan, L. Cheng. “Two-dimensional scattering features of the mixed second harmonic A0 mode Lamb waves for incipient damage localization”. *Ultrasonics* vol. 119 (Feb. 2022), p. 106554.

[33] Z. Su, L. Ye, Y. Lu. “Guided Lamb waves for identification of damage in composite structures: A review”. *Journal of Sound and Vibration* vol. 295.3 (Aug. 2006), p. 753–780.

[34] B. Blachowski et al. “Structural damage detectability using modal and ultrasonic approaches”. *Measurement* vol. 85 (May 2016), p. 210–221.

[35] B. Rocha et al. “Design and development of a phased array system for damage detection in structures”. In: *Structural Health Monitoring for Advanced Composite Structures*. World Scientific Publishing Co. Pte Ltd, Dec. 2017, pp. 153–189.

[36] Z.-B. Yang et al. “FRF-based lamb wave phased array”. *Mechanical Systems and Signal Processing* vol. 166 (Mar. 2022), p. 108462.

[37] H. Xu et al. “Nonlinear Lamb wave phased array for revealing micro-damage based on the second harmonic reconstruction”. *Mechanical Systems and Signal Processing* vol. 220 (Nov. 2024), p. 111692.

[38] L. Wang, F. G. Yuan. “Damage Identification in a Composite Plate using Prestack Reverse-time Migration Technique”. *Structural Health Monitoring* vol. 4.3 (Sept. 2005), p. 195–211.

[39] W. Ostachowicz, R. Soman, P. Malinowski. “Optimization of sensor placement for structural health monitoring: a review”. *Structural Health Monitoring* vol. 18.3 (May 2019), p. 963–988.

[40] A. Tavares et al. “Machine Learning approaches to damage detection in composite structures combining experimental and simulation domains”. *Mechanical Systems and Signal Processing* vol. 215 (June 2024), p. 111412.

[41] L. Yu, V. Giurgiutiu. “In situ 2-D piezoelectric wafer active sensors arrays for guided wave damage detection”. *Ultrasonics* vol. 48.2 (Apr. 2008), p. 117–134.

[42] J. Yue, X. Hong, B. Zhang. “A damage imaging method based on particle swarm optimization for composites nondestructive testing using ultrasonic guided waves”. *Applied Acoustics* vol. 218 (Mar. 2024), p. 109878.

[43] F. K. Gruber, E. A. Marengo, A. J. Devaney. “Time-reversal imaging with multiple signal classification considering multiple scattering between the targets”. *The Journal of the Acoustical Society of America* vol. 115.6 (June 2004), p. 3042–3047.

[44] C. H. Wang, J. T. Rose, F.-K. Chang. “A synthetic time-reversal imaging method for structural health monitoring”. *Smart Materials and Structures* vol. 13.2 (Mar. 2004), p. 415.

[45] H. Sohn et al. “Damage Detection in Composite Plates by Using an Enhanced Time Reversal Method”. *Journal of Aerospace Engineering* vol. 20.3 (July 2007), p. 141–151.

[46] Y. Yu et al. “Lamb wave-based damage imaging of CFRP composite structures using autoencoder and delay-and-sum”. *Composite Structures* vol. 303 (Jan. 2023), p. 116263.

[47] K. Luo et al. “Ultrasonic Lamb Wave Damage Detection of CFRP Composites Using the Bayesian Neural Network”. *Journal of Nondestructive Evaluation* vol. 43.2 (Apr. 2024), p. 48.

[48] F. Zheng et al. “Integrated MUSIC array for high-precision damage diagnosis in complex composite structures”. *Ultrasonics* vol. 143 (Sept. 2024), p. 107425.

[49] C. Xu et al. “A focusing MUSIC algorithm for baseline-free Lamb wave damage localization”. *Mechanical Systems and Signal Processing* vol. 164 (Feb. 2022), p. 108242.

[50] C. Ferreira, G. Gonçalves. “Remaining Useful Life prediction and challenges: A literature review on the use of Machine Learning Methods”. *Journal of Manufacturing Systems* vol. 63 (Apr. 2022), p. 550–562.

[51] J. Deutsch, D. He. “Using Deep Learning-Based Approach to Predict Remaining Useful Life of Rotating Components”. *IEEE Transactions on Systems, Man, and Cybernetics: Systems* vol. 48.1 (Jan. 2018), p. 11–20.

[52] T. Loutas, N. Eleftheroglou, D. Zarouchas. “A data-driven probabilistic framework towards the in-situ prognostics of fatigue life of composites based on acoustic emission data”. *Composite Structures* vol. 161 (Feb. 2017), p. 522–529.

[53] L. Gan, H. Wu, Z. Zhong. “On the use of data-driven machine learning for remaining life estimation of metallic materials based on Ye-Wang damage theory”. *International Journal of Fatigue* vol. 156 (Mar. 2022), p. 106666.

[54] C. Peeters, P. Guillaume, J. Helsen. “A comparison of cepstral editing methods as signal pre-processing techniques for vibration-based bearing fault detection”. *Mechanical Systems and Signal Processing* vol. 91 (July 2017), p. 354–381.

[55] P. Kudela et al. “Structural Health Monitoring system based on a concept of Lamb wave focusing by the piezoelectric array”. *Mechanical Systems and Signal Processing* vol. 108 (2018), p. 21–32.

[56] T. Hayashi, C. Tamayama, M. Murase. “Wave structure analysis of guided waves in a bar with an arbitrary cross-section”. *Ultrasonics* vol. 44.1 (Jan. 2006), p. 17–24.

[57] A. Shelke et al. “Mode-selective excitation and detection of ultrasonic guided waves for delamination detection in laminated aluminum plates”. *IEEE Transactions on Ultrasonics, Ferroelectrics, and Frequency Control* vol. 58.3 (Mar. 2011), p. 567–577.

[58] M. Sayah et al. “Robustness testing framework for RUL prediction Deep LSTM networks”. *ISA Transactions* vol. 113 (July 2021), p. 28–38.

[59] T. Benkedjouh et al. “Remaining useful life estimation based on nonlinear feature reduction and support vector regression”. *Engineering Applications of Artificial Intelligence* vol. 26.7 (Aug. 2013), p. 1751–1760.

[60] Y. Zhang et al. “A LSTM-RNN method for the lithuim-ion battery remaining useful life prediction”. In: *2017 Prognostics and System Health Management Conference (PHM-Harbin)*. ISSN: 2166-5656. July 2017, pp. 1–4.

[61] L. Ren et al. “A Data-Driven Auto-CNN-LSTM Prediction Model for Lithium-Ion Battery Remaining Useful Life”. *IEEE Transactions on Industrial Informatics* vol. 17.5 (May 2021), p. 3478–3487.

[62] K. Xue et al. “An Improved Generic Hybrid Prognostic Method for RUL Prediction Based on PF-LSTM Learning”. *IEEE Transactions on Instrumentation and Measurement* vol. 72 (2023), p. 1–21.

[63] M. Ma, Z. Mao. “Deep-Convolution-Based LSTM Network for Remaining Useful Life Prediction”. *IEEE Transactions on Industrial Informatics* vol. 17.3 (Mar. 2021), p. 1658–1667.

[64] H. Miao et al. “Joint Learning of Degradation Assessment and RUL Prediction for Aeroengines via Dual-Task Deep LSTM Networks”. *IEEE Transactions on Industrial Informatics* vol. 15.9 (Sept. 2019), p. 5023–5032.

[65] M. Moradi et al. “Intelligent health indicator construction for prognostics of composite structures utilizing a semi-supervised deep neural network and SHM data”. *Engineering Applications of Artificial Intelligence* vol. 117 (2023), p. 105502.

[66] V. Ewald, R. M. Groves, R. Benedictus. “DeepSHM: A deep learning approach for structural health monitoring based on guided Lamb wave technique”. In: *Sensors and Smart Structures Technologies for Civil, Mechanical, and Aerospace Systems 2019*. Vol. 10970. SPIE, 2019, pp. 84–99.

[67] M. Azimi, A. D. Eslamlou, G. Pekcan. “Data-driven structural health monitoring and damage detection through deep learning: State-of-the-art review”. *Sensors* vol. 20.10 (2020), p. 2778.

[68] H. Zhao et al. “Feature Extraction for Data-Driven Remaining Useful Life Prediction of Rolling Bearings”. *IEEE Transactions on Instrumentation and Measurement* vol. 70 (2021), p. 1–10.

[69] G. Liu et al. “Sensor faults classification for SHM systems using deep learning-based method with Tsfresh features”. *Smart Materials and Structures* vol. 29.7 (2020), p. 075005.

[70] E. García-Macías, F. Ubertini. “Integrated SHM Systems: Damage Detection Through Unsupervised Learning and Data Fusion”. en. In: *Structural Health Monitoring Based on Data Science Techniques*. Ed. by A. Cury et al. Vol. 21. Series Title: Structural Integrity. Cham: Springer International Publishing, 2022, pp. 247–268.

[71] L. Rosafalco et al. “Online structural health monitoring by model order reduction and deep learning algorithms”. *Computers & Structures* vol. 255 (2021), p. 106604.

[72] K. R. Lyathakula, F.-G. Yuan. “Scalable and portable computational framework enabling online probabilistic remaining useful life (RUL) estimation”. *Advances in Engineering Software* vol. 181 (2023), p. 103461.

[73] K. Reddy Lyathakula, F.-G. Yuan. “Fatigue Damage Diagnostics–Prognostics Framework for Remaining Life Estimation in Adhesive Joints”. *AIAA Journal* vol. 60.8 (Aug. 2022), p. 4874–4892.

[74] K. R. Lyathakula, F.-G. Yuan. “A probabilistic fatigue life prediction for adhesively bonded joints via ANNs-based hybrid model”. *International Journal of Fatigue* vol. 151 (Oct. 2021), p. 106352.

[75] M. Słoński. “Assessment of Cracking Development in Concrete Precast Crane Beams Using Optical and Deep Learning Methods”. *Materials* vol. 18.4 (Jan. 2025), p. 731.

[76] P. Nazarko, L. Ziemianski. “Damage detection in aluminum and composite elements using neural networks for Lamb waves signal processing”. *Engineering Failure Analysis*. Special issue on the International Conference on Structural Integrity vol. 69 (Nov. 2016), p. 97–107.

[77] G. Galanopoulos et al. “Acoustic emission-based remaining useful life prognosis of aeronautical structures subjected to compressive fatigue loading”. *Engineering Structures* vol. 290 (2023), p. 116391.

[78] G. Galanopoulos et al. “A data driven methodology for upscaling remaining useful life predictions: From single- to multi-stiffened composite panels”. *Composites Part C: Open Access* vol. 11 (July 2023), p. 100366.

[79] A. Mosallam, K. Medjaher, N. Zerhouni. “Integrated bayesian framework for remaining useful life prediction”. In: *2014 International Conference on Prognostics and Health Management*. IEEE, 2014, pp. 1–6.

[80] C. Hu et al. “Ensemble of data-driven prognostic algorithms for robust prediction of remaining useful life”. *Reliability Engineering & System Safety* vol. 103 (2012), p. 120–135.

[81] T. Gao et al. “Data-driven method for predicting remaining useful life of bearing based on Bayesian theory”. *Sensors* vol. 21.1 (2020), p. 182.

[82] M. Wang et al. “Structural fatigue life prediction considering model uncertainties through a novel digital twin-driven approach”. *Computer Methods in Applied Mechanics and Engineering* vol. 391 (Mar. 2022), p. 114512.

[83] E. Giannaros et al. “Low- and high-fidelity modeling of sandwich-structured composite response to bird strike, as tools for a digital-twin-assisted damage diagnosis”. *International Journal of Impact Engineering* vol. 160 (Feb. 2022), p. 104058.

[84] M. Zhang et al. “Digital twin data: methods and key technologies”. *Digital Twin* vol. 1 (2022), p. 2.

[85] H. Jiang et al. “How to model and implement connections between physical and virtual models for digital twin application”. *Journal of Manufacturing Systems* vol. 58 (2021), p. 36–51.

[86] J. Friederich et al. “A framework for data-driven digital twins of smart manufacturing systems”. *Computers in Industry* vol. 136 (2022), p. 103586.

[87] Y. Ye et al. “A dynamic data driven reliability prognosis method for structural digital twin and experimental validation”. *Reliability Engineering & System Safety* vol. 240 (Dec. 2023), p. 109543.

[88] C. Yang et al. “Cross-validation enhanced digital twin driven fault diagnosis methodology for minor faults of subsea production control system”. *Mechanical Systems and Signal Processing* vol. 204 (Dec. 2023), p. 110813.

[89] C. Yang et al. “Digital twin-driven fault diagnosis method for composite faults by combining virtual and real data”. *Journal of Industrial Information Integration* vol. 33 (June 2023), p. 100469.

[90] W. Ostachowicz et al. *Guided waves in structures for SHM: the time-domain spectral element method*. John Wiley & Sons, 2011.

[91] E. Bechhoefer, R. Schlanbusch. “Generalized Prognostics Algorithm Using Kalman Smoother”. *IFAC-PapersOnLine*. 9th IFAC Symposium on Fault Detection, Supervision andSafety for Technical Processes SAFEPROCESS 2015 vol. 48.21 (Jan. 2015), p. 97–104.

[92] J. Chen et al. “Research on a Lamb Wave and Particle Filter-Based On-Line Crack Propagation Prognosis Method”. *Sensors* vol. 16.3 (Mar. 2016), p. 320.

[93] C. J. Keulen et al. “Prediction of fatigue response of composite structures by monitoring the strain energy release rate with embedded fiber Bragg gratings”. *Journal of Intelligent Material Systems and Structures* vol. 27.1 (Jan. 2016), p. 17–27.

[94] J. Chen, S. Yuan, X. Jin. “On-line prognosis of fatigue cracking via a regularized particle filter and guided wave monitoring”. *Mechanical Systems and Signal Processing* vol. 131 (Sept. 2019), p. 1–17.

[95] T. Li et al. “Numerical simulation-aided particle filter-based damage prognosis using Lamb waves”. *Mechanical Systems and Signal Processing* vol. 178 (2022), p. 109326.

[96] Y. Cheng et al. “Remaining useful life prognosis based on ensemble long short-term memory neural network”. *IEEE Transactions on Instrumentation and Measurement* vol. 70 (2020), p. 1–12.

[97] A. Al-Dulaimi et al. “A multimodal and hybrid deep neural network model for remaining useful life estimation”. *Computers in industry* vol. 108 (2019), p. 186–196.

[98] A. Aria et al. “Estimating damage size and remaining useful life in degraded structures using deep learning-based multi-source data fusion”. *Structural Health Monitoring* vol. 19.5 (Sept. 2020), p. 1542–1559.

[99] T. Hielscher et al. “A neural network based digital twin model for the structural health monitoring of reinforced concrete bridges”. In: *Structures*. Vol. 57. Elsevier, 2023, p. 105248.

[100] S. H. Khajavi et al. “Digital twin: vision, benefits, boundaries, and creation for buildings”. *IEEE access* vol. 7 (2019), p. 147406–147419.

[101] D.-G. J. Opoku et al. “Digital twin application in the construction industry: A literature review”. *Journal of Building Engineering* vol. 40 (2021), p. 102726.

[102] Q. Lu et al. “Developing a Digital Twin at Building and City Levels: Case Study of West Cambridge Campus”. *Journal of Management in Engineering* vol. 36.3 (May 2020), p. 05020004.

[103] V. Qiuchen Lu et al. “Developing a Dynamic Digital Twin at a Building Level: using Cambridge Campus as Case Study”. en. In: *International Conference on Smart Infrastructure and Construction 2019 (ICSIC)*. Cambridge, UK: ICE Publishing, Jan. 2019, pp. 67–75.

[104] V. Nerlikar et al. “Machine learning-based digital twin framework for realistic guided wave signal generation, applied to reliability assessment and global sensitivity analysis in shm”. In: *50th annual review of progress in quantitative nondestructive evaluation*. Vol. 87202. American Society of Mechanical Engineers, 2023, V001T05A003.

[105] D. Milanoski et al. “Multi-level damage diagnosis on stiffened composite panels based on a damage-uninformative digital twin”. *Structural Health Monitoring* vol. 22.2 (Mar. 2023), p. 1437–1459.

[106] K. Kim et al. “Adhesion enhancement and damage protection for carbon fiber-reinforced polymer (CFRP) composites via silica particle coating”. *Composites Part A: Applied Science and Manufacturing* vol. 109 (June 2018), p. 105–114.

[107] G. R. Edwards. “Qualification of digital twins for predicting failure in welded structures”. In: *Proceedings of the Annual British Conference on Non-Destructive Testing*. Vol. 2023. Issue: 1. The British Institute of Non-Destructive Testing, 2023, pp. 1–11.

[108] C. Ye et al. “A digital twin of bridges for structural health monitoring”. In: *12th International Workshop on Structural Health Monitoring 2019*. Stanford University, 2019.

[109] Y.-C. Zhu et al. “Real-Time Digital Twin Updating Strategy Based on Structural Health Monitoring Systems”. en. In: *Model Validation and Uncertainty Quantification, Volume 3*. Ed. by Z. Mao. Series Title: Conference Proceedings of the Society for Experimental Mechanics Series. Cham: Springer International Publishing, 2020, pp. 55–64.

[110] A. Z. O. Al-Hijazeen et al. “Implementation of digital twin and support vector machine in structural health monitoring of bridges”. *Archives of Civil Engineering* (2023), p. 31–47.

[111] H. V. Dang, M. Tatipamula, H. X. Nguyen. “Cloud-based digital twinning for structural health monitoring using deep learning”. *IEEE transactions on industrial informatics* vol. 18.6 (2021), p. 3820–3830.

[112] X. Lai et al. “Digital twin-based structural health monitoring by combining measurement and computational data: An aircraft wing example”. *Journal of Manufacturing Systems* vol. 69 (2023), p. 76–90.

[113] X. Hu, G. Olgun, R. H. Assaad. “An intelligent BIM-enabled digital twin framework for real-time structural health monitoring using wireless IoT sensing, digital signal processing, and structural analysis”. *Expert Systems with Applications* vol. 252 (2024), p. 124204.

[114] S. Hochreiter, J. Schmidhuber. “Long Short-Term Memory”. *Neural Computation* vol. 9.8 (Nov. 1997), p. 1735–1780.

[115] Y. Gal, Z. Ghahramani. “Dropout as a Bayesian Approximation: Representing Model Uncertainty in Deep Learning”. en. In: *Proceedings of The 33rd International Conference on Machine Learning*. ISSN: 1938-7228. PMLR, June 2016, pp. 1050–1059.

[116] M. L. Benzeggagh, M. Kenane. “Measurement of mixed-mode delamination fracture toughness of unidirectional glass/epoxy composites with mixed-mode bending apparatus”. *Composites Science and Technology* vol. 56.4 (Jan. 1996), p. 439–449.

[117] A. Turon et al. “An engineering solution for mesh size effects in the simulation of delamination using cohesive zone models”. *Engineering Fracture Mechanics* vol. 74.10 (July 2007), p. 1665–1682.

[118] Y. J. Wang, C. Q. Ru. “Determination of two key parameters of a cohesive zone model for pipeline steels based on uniaxial stress-strain curve”. *Engineering Fracture Mechanics* vol. 163 (Sept. 2016), p. 55–65.

[119] Y. Ling, A. Incorporated. “Uniaxial True Stress-Strain after Necking”. In: 2004.

[120] T. E. A. Ribeiro et al. “Damage analysis of composite–aluminium adhesively-bonded single-lap joints”. *Composite Structures* vol. 136 (Feb. 2016), p. 25–33.

[121] H. Khoramishad et al. “Predicting fatigue damage in adhesively bonded joints using a cohesive zone model”. *International Journal of Fatigue* vol. 32.7 (July 2010), p. 1146–1158.

[122] D. M. Blei, A. Kucukelbir, J. D. M. and. “Variational Inference: A Review for Statisticians”. *Journal of the American Statistical Association* vol. 112.518 (2017), p. 859–877.

[123] N. Razavi et al. “Single lap joints bonded with structural adhesives reinforced with a mixture of silica nanoparticles and multi walled carbon nanotubes”. *International Journal of Adhesion and Adhesives* vol. 80 (2018), p. 76–86.